ANL-24/51

Design Methods, Tools, and Data for Ceramic Solar Receivers

Applied Materials Division

ANL-24/51

Design Methods, Tools, and Data for Ceramic Solar Receivers

---

prepared by
Pawan Chaugule, Argonne National Laboratory
Bipul Barua, Argonne National Laboratory
Dileep Singh, Argonne National Laboratory
Mark C. Messner, Argonne National Laboratory

Applied Materials Division

September 2024

Abstract

This report presents the development of tools and methods for evaluating the reliability and performance of ceramic materials in high temperature solar receivers. As Concentrating Solar Power (CSP) technologies aim for higher operating temperatures to enhance efficiency and meet industrial process heat requirements, current high temperature metallic materials face challenges in maintaining structural integrity. This report explores advanced ceramics as a promising alternative, given their superior high temperature strength and lower thermal expansion, compared to metals. To address the need for effective ceramic receiver design tools, this report integrates statistical failure models of ceramics into the existing *srlife* tool: an open-source software package designed to estimate the life of high temperature CSP components. These failure models account for the inherent variability and flaw distribution in ceramics, as well as the impact of subcritical crack growth under high temperature cyclic loads. The report also presents experimental data collected for a commercially available ceramic material, SiC, and details the process of estimating reliability model parameters from these data. A comparative design analysis is then performed between ceramic (SiC) and metallic (current nickel-based superalloys A740H and A282) receiver. This comparison demonstrates that SiC receivers can achieve service life exceeding 30 years under high incident heat flux conditions, compared to just a few years for metallic receivers.

Table of Contents

List of Figures

List of Tables

Part I

Introduction

1 Introduction

As Concentrating Solar Power (CSP) system progresses towards Generation 3 designs, achieving higher outlet temperatures poses significant challenges to the structural integrity of high temperature metallic materials [1] [2]. These increasing temperature demands are driven not only by efficiency goals for CSP systems but also by the need to meet process heat requirements for decarbonizing industrial operations, such as steel [3] and ammonia production [4]. This creates a pressing need to explore alternative materials capable of withstanding such extreme conditions.

Advanced ceramics emerge as a promising alternative due to their superior high temperature strength and relatively low thermal expansion [5]. Despite their potential advantages, ceramics face challenges such as limited ductility and complexities in fabrication and joining with other plant components. Therefore, before tackling these manufacturing challenges, it is crucial for CSP developers to assess whether high temperature ceramic components are viable within the context of a complete system design.

A key factor in evaluating the feasibility of ceramic components is their expected operational life under the challenging conditions of next-generation CSP systems. Currently, there is a gap in suitable methods and software tools for designing high temperature ceramic receivers, which prevents detailed comparisons between ceramic and metallic receiver designs. Ceramic materials exhibit distinct failure mechanisms compared to metals, including subscale flaws from the manufacturing process that can grow under thermal and mechanical loads, leading to brittle fracture [6]. Unlike metals, whose failure mechanisms are often well-characterized, ceramic failure is inherently statistical, linked to the distribution and evolution of flaws within the material [7].

Rather than using conventional design methods based on bounding analysis, as is common for metallic structures, ceramic design must account for the statistical nature of material strength. high temperature ceramic design must include both the initial flaw population and how these flaws evolve over time, particularly under thermal cycling and environmental exposure [8]. The evolving flaw population leads to changes in the material's strength distribution as service continues (see Fig. 1.1). Thus, an adequate design approach for high temperature ceramic CSP systems must account for both the variability in initial strength and the ongoing changes in material properties over time.

To address these challenges, statistical failure theories, such as the Weibull distribution, are employed to model the reliability of ceramics. NASA's CARES program [9] [10] offers a robust framework for failure analysis of ceramics, including the effects of subcritical crack growth (SCG), a phenomenon that impacts ceramics under high temperature cyclic loading. This work incorporates NASA's methodology into the *srlife* tool [11], which was originally developed for evaluating the life of metallic receivers, and extends it for evaluating ceramic receivers.

The primary goal of this project is to provide CSP developers with the necessary tools and insights to evaluate the viability of ceramic components, enabling them to make informed decisions for future system designs. The objectives of this report include:

1. Providing users an automated tool for the statistical life assessment of high temperature ceramic CSP components.

2. Demonstrating how to parameterize reliability models for an industrially relevant high

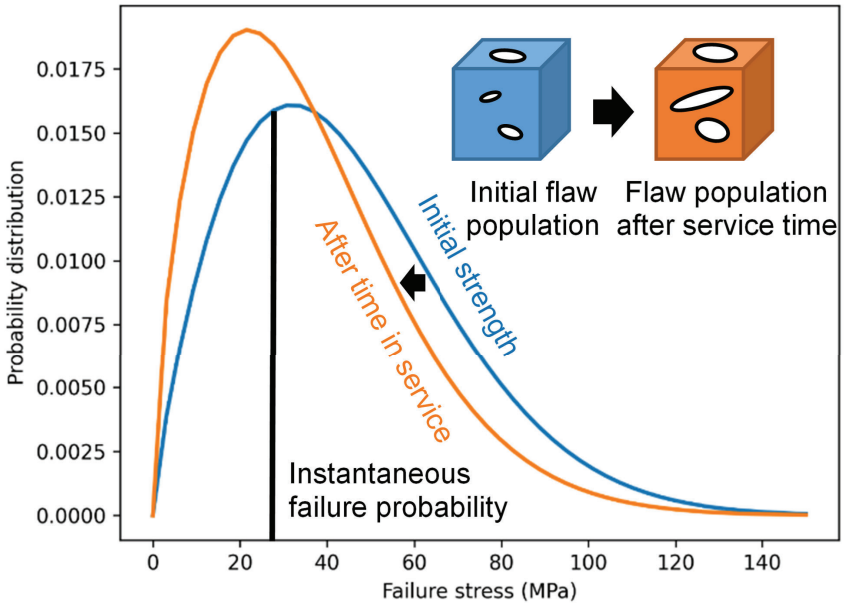

Figure 1.1: Illustration of how time-dependent flaw growth affects the strength of ceramic materials.

temperature ceramic material.

3. Comparing the long-term reliability of ceramic and metallic salt receiver designs.

Chapters 2 and 3 detail the time-independent and time-dependent failure models for ceramics, respectively. Chapter 4 covers the implementation of these models in *srlife* and their validation. Chapter 5 discusses the experimental methods used to estimate model parameters, focusing on high temperature testing of a commercial engineering ceramic material, SiC. Chapter 6 outlines the reliability analysis process within *srlife*, including options for different failure models and criteria. In Chapter 7, the performance of SiC ceramics is compared with nickel-based superalloys, such as A740H and A282, in high temperature CSP applications. The report concludes with a summary in Chapter 8.

Part II

Ceramic Failure Models

2 Time-independent Failure

This chapter describes several models that can predict time-independent failure of advanced ceramic materials. These models all start from the uniaxial failure statistics for a heat of ceramic material, for example as quantified by a series of four-point bend tests (see Part III). The goal of these models is to extend the uniaxial failure model to arbitrary states of stress and account for the size effect. The size effect here is the fact that the larger the sample volume the more likely it will be to find a critical flaw in that volume. That is, for ceramics, larger equals weaker.

The models are based on failure theories from the literature and have been converted to a suite of failure models similar to the approach taken in the CARES manual [10] by NASA. The failure models are (i) Principle of Independent Action (PIA) [12, 13], (ii) Weibull Normal Tensile Stress Averaging (WNTSA) [14, 15], (iii) Maximum Tensile Stress (MTS) Criterion [10], (iv) Total Co-planar Strain Energy (CSE) release rate criterion [10], and (v) Shetty's Mixed-Mode (SMM) criterion [16, 17] or Non-Coplanar Strain Energy (NCSE) release rate criterion.

Since ceramics can fail majorly from volume-based flaws (distributed throughout the volume) and surface-based flaws (present on the surface), the failure models are categorized for both flaw types as shown by the flow chart in Fig. 2.1(a) and 2.2(a), respectively. The models are also categorized based on their dependency on the crack (or flaw) shape (or geometry) and fracture criteria. A schematic of each flaw shape considered is shown for volume flaws in Fig. 2.1(b) and for surface flaws in Fig. 2.2(b). The PIA and WNTSA models are crack shape independent and shear insensitive. While the other models are crack shape dependent and for them, the following crack shapes are considered: Griffith Flaw (GF), Penny Shaped Flaw (PSF), Griffith Notch (GN), and Semi-Circular Crack (SCC). The arrows shown below each flow chart represent the direction of increase in complexity across the models.

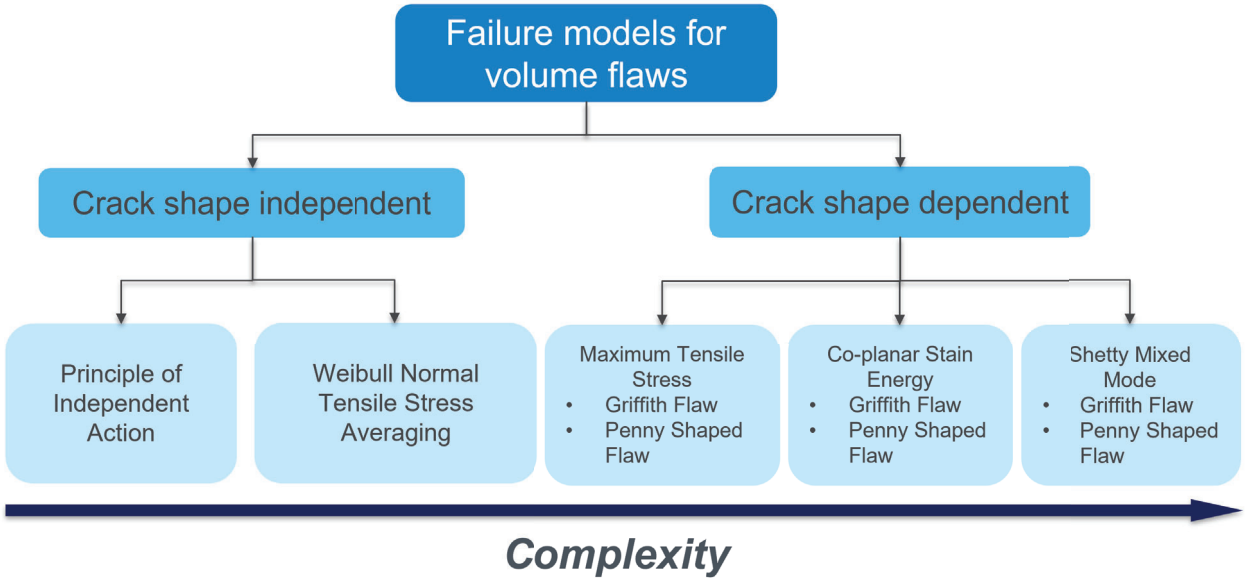

(a)

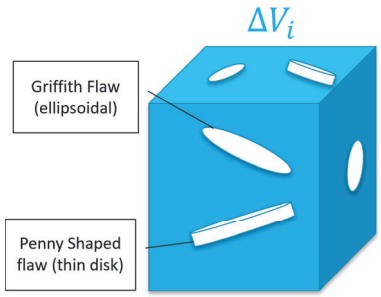

(b)

Figure 2.1: (a) Flow chart of failure models implemented in *srlife* for volume flaws, (b) Schematic of volume flaws considered on a volume element ΔV.

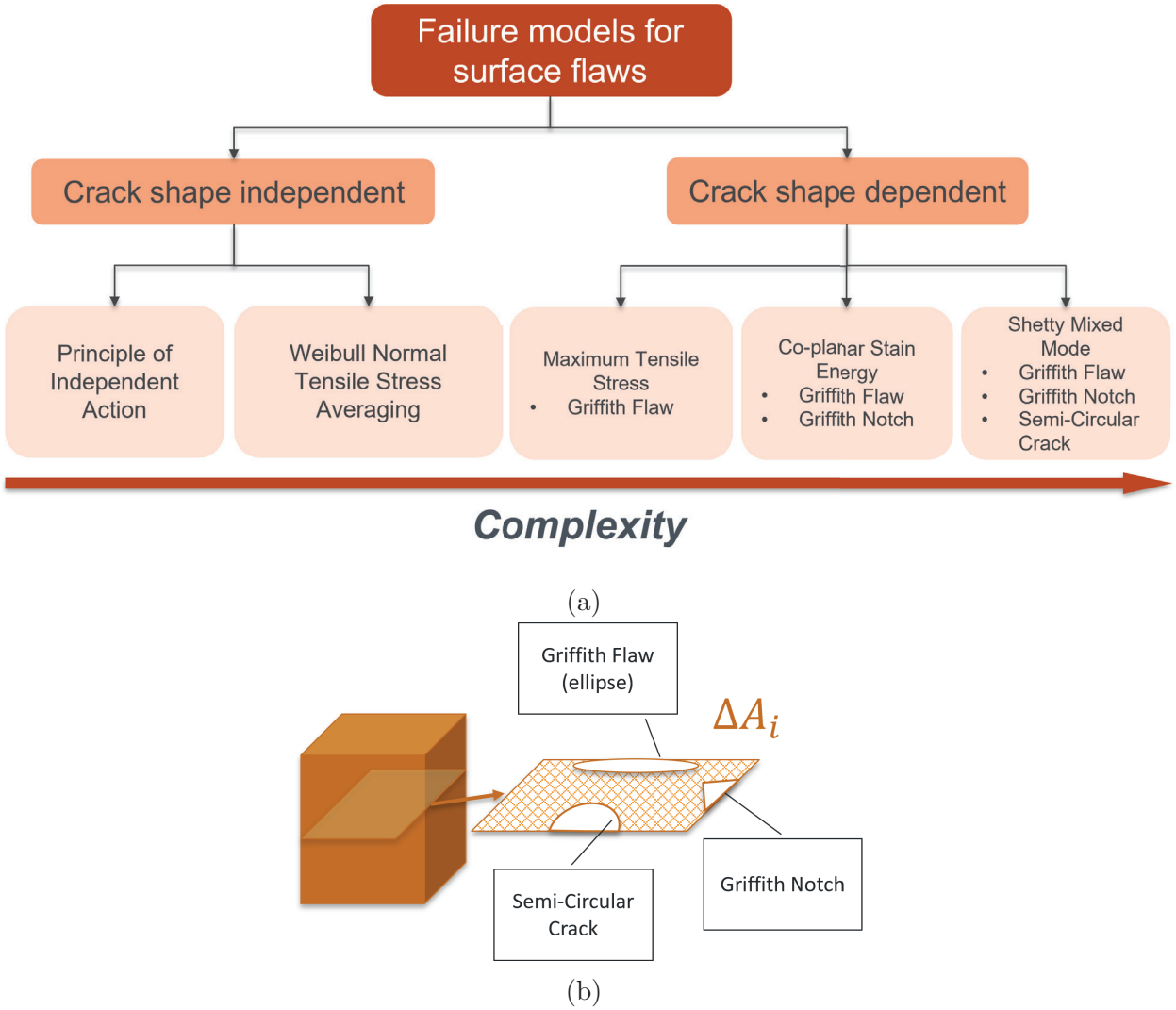

Figure 2.2: (a) Flow chart of failure models implemented in *srlife* for surface flaws, (b) Schematic of surface flaws considered on an area element ΔA.

The models have been developed to account for multiaxial stresses provided by the structural analyses in *srlife*. These multiaxial stresses are converted to their principal components and relevant equivalent stresses using the constitutive equations for each failure model. These stresses and the relevant material parameters are then used to analytically calculate the probability of failure using Eq. 2.1. The equation involves relevant material properties (or characteristics) which include the: Weibull modulus (m), characteristic strength (σ_θ), and scale parameter (σ_0). These properties are estimated from experimental test data demonstrated later in Part III. Additionally, the parameters uniaxial Weibull crack density coefficient (k_w) and polyaxial Weibull crack density coefficient (k_{wp}) are estimated from σ_0 and m. Lastly, the parameter k_B is the Batdorf crack density coefficient that is estimated analytically as shown in Section 2.3. Each of the above properties is classified for the type of flaw i.e. surface or volume. Using the properties and by considering the flaw types, a failure probability is evaluated by integrating a crack density function $N(\sigma)$ in the following equation:

$$P_f = \begin{cases} 1 - exp\left[-\int_V N(\sigma) dV\right] & ...volume\ flaws \\ 1 - exp\left[-\int_A N(\sigma') dA\right] & ...surface\ flaws \\ 1 - exp\left[-(\int_V N(\sigma) dV + \int_A N(\sigma') dA)\right] & ...combined\ flaws \end{cases} \tag{2.1}$$

where $N(\sigma)$ is defined in literature [18, 19, 20, 21, 16] using the following representations:

$$N(\sigma) = \begin{cases} \left(\frac{\sigma}{\sigma_0}\right)^m \equiv k_w \sigma^m & Weibull\ 2\ parameter\ uniaxial\ model \\ \left(\frac{\sigma - \sigma_u}{\sigma_0}\right)^m \equiv k_w (\sigma - \sigma_u)^m & Weibull\ 3\ parameter\ uniaxial\ model \\ \left(\frac{f(\sigma_1, \sigma_2, \sigma_3)}{\sigma_0}\right)^m \equiv k_w f(\sigma_1, \sigma_2, \sigma_3)^m & PIA\ model \\ \left(\frac{f(\sigma_n)}{\sigma_0}\right)^m \equiv k_{wp} f(\sigma_n)^m & WNTSA\ model \\ \left(\frac{f(\sigma_e)}{\sigma_0}\right)^m \equiv k_B f(\sigma_e)^m & Batdorf\ polyaxial\ models \end{cases} \tag{2.2}$$

In the first two representations i.e. in the Weibull 2 parameter and 3 parameter uniaxial models, $N(\sigma)$ is determined using the uniaxial applied stress from experiments. These representations will be revisited in Part III. In the remaining three representations, $N(\sigma)$ is determined using the PIA, WNTSA, and Batdorf models. These representations involve a power law model, wherein a ratio is taken between a function and the Weibull scale parameter. The function is applied on a 3D stress tensor (σ). Based on the model, the tensor is converted to its principal components and further quantities (σ_n, σ_e) by applying various analytical functions. This approach is followed primarily for volume flaws. In case of surface flaws in-plane 2D stresses (σ') are first evaluated from the projection of the 3D stress tensor (σ) onto the surface elements, and then implemented into the models. The projection involves using a projection tensor P formulated using the surface normals (n_x, n_y, n_z) as described using Eq. 2.3 which was originally derived by Hotz. et. al. [22].

$$\sigma' = P \cdot \sigma \cdot P^T \tag{2.3}$$

$$N = \begin{pmatrix} n_x \\ n_y \\ n_z \end{pmatrix} \tag{2.4}$$

$$\begin{aligned} P &= \begin{pmatrix} (1 - n_x^2) & -n_x n_y & -n_x n_z \\ -n_x n_y & (1 - n_y^2) & -n_y n_z \\ -n_x n_z & -n_y n_z & (1 - n_z^2) \end{pmatrix} \\ &= I - n \otimes n \end{aligned} \tag{2.5}$$

The following subsections describe each of the models in detail with equations formulated separately for volume flaws (subscripted as V) and surface flaws (subscripted as S).

2.1 Crack Shape Independent Models

As shown in the flow chart, the models that are independent of the crack shape are formulated using the following criteria:

2.1.1 Principle of Independent Action (PIA)

This method predicts the probability of failure (P_f) directly by considering only the tensile principal stresses ($\sigma_1, \sigma_2, \sigma_3 \geq 0$) assuming they act independently on the flaws [12, 13]. In case of volume flaws for a small uniformly stressed volume element (dV or ΔV_i), P_f is defined by summing up the contributions from the stresses in the volume elements as shown in Eq. 2.7.

$$P_f = 1 - exp\left[k_{wV} \int_v (\sigma_1^{m_v} + \sigma_2^{m_v} + \sigma_3^{m_v}) dV\right] \tag{2.6}$$

or

$$P_f = 1 - exp\left[k_{wV} \sum_i^n (\sigma_1^{m_v} + \sigma_2^{m_v} + \sigma_3^{m_v})_i \Delta V_i\right] \tag{2.7}$$

and in case of surface flaws, a similar summation is applied over the small uniformly stressed area elements (dA or ΔA_i) to calculate the P_f in Eq. 2.9.

$$P_f = 1 - exp\left[k_{wS} \int_v (\sigma_1^{'m_S} + \sigma_2^{'m_S}) dA\right] \tag{2.8}$$

or

$$P_f = 1 - exp\left[k_{wS} \sum_i^n (\sigma_1^{'m_S} + \sigma_2^{'m_S})_i \Delta A_i\right] \tag{2.9}$$

where; $k_w = \sigma_0^{-m}$ and $\sigma_i = 0$ if $\sigma < 0$, because ceramics show significantly higher compressive strengths compared to their tensile strengths, and thus, it is assumed that compressive stresses do not contribute majorly to their failure [10]. Hence, as a heuristic in the PIA model, only tensile principal stresses (σ_i and σ_i' >0) are considered. If compressive principal stresses appear in the structure, their contribution to the failure probability is taken to be zero. Additionally, the contribution from shear stresses, different crack orientations, and modes of crack extensions are also ignored.

2.1.2 Weibull Normal Tensile Stress Averaging (WNTSA)

This method predicts the failure probability directly by considering only the average normal tensile stresses ($\overline{\sigma_n}$) [14, 15]. First, the normal stresses are evaluated from the principal stresses for i.e. σ_n for volume flaws using Eq. 2.27 and σ_n' for surface flaws using Eq. 2.29. The calculation considers the different crack orientations using the direction cosines (l, m, n) for volume flaws and (p, o) for surface flaws. Next, only the tensile normal stresses are taken and averaged by integrating over (i) the surface of a sphere of unit radius defined in 3D

principal stress space, for volume flaws (Eq. 2.10) and (ii) over the boundary of a circle of unit radius defined in principal stress space for surface flaws (Eq. 2.13). As observed shear stresses and different modes of crack extensions are ignored by the WNTSA model. The failure probability is calculated using the averaged normal tensile stress in Eq. 2.11 and 2.14. The equation considers a polyaxial Weibull crack density coefficient (k_{wp}), which is derived by equating the failure probability for uniaxial loading, to the failure probability for polyaxial loading when the latter is reduced to a uniaxial condition.

For volume flaws:

$$\overline{\sigma_n}^{m_V} = \begin{cases} \dfrac{\int_A \sigma_n^{m_V} dA}{\int_A dA} & \sigma_n \geq 0 \\ 0 & \sigma_n < 0 \end{cases} \tag{2.10}$$

$$P_{fV} = 1 - exp\left[-k_{wpV} \sum_i^n (\overline{\sigma_n}^{m_V})_i \Delta V_i\right] \tag{2.11}$$

where

$$k_{wpV} = (2m_V + 1)k_{wV} = (2m_V + 1)\sigma_{0V}^{-m_V} \tag{2.12}$$

For surface flaws:

$$\overline{\sigma_n}'^{m_S} = \begin{cases} \dfrac{\int_c \sigma_n'^{m_S} dc}{\int_c dc} & \sigma_n' \geq 0 \\ 0 & \sigma_n' < 0 \end{cases} \tag{2.13}$$

$$P_{fS} = 1 - exp\left[-k_{wpS} \sum_i^n (\overline{\sigma_n}'^{m_S})_i \Delta A_i\right] \tag{2.14}$$

where

$$k_{wpS} = \frac{m_S \Gamma(m_S)\sqrt{\pi}}{\Gamma(m_S + 0.5)} k_{ws} = \frac{m_S \Gamma(m_S)\sqrt{\pi}}{\Gamma(m_S + 0.5)} \sigma_{0S}^{-m_S} \tag{2.15}$$

and Γ is the gamma function.

2.2 Crack Shape Dependent Models

The next category of models are crack shape dependent models. These were originally developed by Batdorf and Heinisch [18] and are based on mixed-mode fracture mechanics. These models combine (1) an assumed crack geometry with (2) a mixed-mode fracture criteria to completely describe the model. The Griffith Flaw crack can be combined with any mixed-mode failure criteria for both volume and surface flaws. The Penny Shaped Flaw is specific to criteria defined for volume flaws only, and the Griffith Notch, Semi-Circular Crack is specific to criteria defined for surface flaws only.

2.2.1 Failure Probability

The incremental probability of failure under an applied stress Σ in a small, uniformly stressed volume element (ΔV) can be written as the following product:

$$\Delta P_{fV}(\Sigma, \sigma_{cr}, \Delta V) = \Delta P_{1V} P_{2V} \tag{2.16}$$

where the product terms described by Batdorf and Crose [19] are:

$$\Delta P_{1V} = \Delta V \frac{dN_V(\sigma_{cr})}{d\sigma_{cr}} d\sigma_{cr} \tag{2.17}$$

ΔP_{1V} is the probability of the existence of a crack having a critical stress between σ_{cr} and $\sigma_{cr} + \Delta\sigma_{cr}$ in the volume ΔV, and

$$P_{2V} = \frac{\Omega(\Sigma, \sigma_{cr})}{4\pi} \tag{2.18}$$

is the probability of a crack of critical stress σ_{cr} oriented in a direction, such that the effective stress on it is greater than the critical stress i.e. $\sigma_e \geq \sigma_{cr}$. The critical stress σ_{cr} is the remote uniaxial strength of a given crack in Mode I loading, and the effective stress σ_e on the crack is based on the normal σ_n and shear τ components of the total traction vector σ acting on the crack plane. Lastly, $N_V(\sigma_{cr})$ is the Batdorf crack density function, and $\Omega(\Sigma, \sigma_{cr})$ is the area of a solid angle projected onto a unit radius sphere in principal stress space containing all crack orientations for which $\sigma_e \geq \sigma_{cr}$. The solid angle area depends on the (i) fracture criterion (ii) crack configuration, and (iii) applied stress. The angle is determined numerically in most cases using the following equation:

$$\Omega(\Sigma, \sigma_{cr}) = \int_0^{\pi/2} \left(\int_0^{\pi/2} sin\alpha d\alpha \right) d\beta \; H(\sigma_e, \sigma_{cr}) \tag{2.19}$$

where $H(\sigma_e, \sigma_{cr}) = \begin{cases} 1; & \sigma_e \geq \sigma_{cr} \\ 0; & \sigma_e < \sigma_{cr} \end{cases}$ The integration limits are based on the symmetry of σ_e in the principal stress space, and hence, are defined for only the first octant of a unit sphere.

Using all the above terms, the component failure probability is calculated for applied stresses varying from 0 to σ_{emax} which is the maximum effective stress a randomly oriented flaw could experience. Mathematically, the failure probability is obtained by substituting Eq. 2.17 and Eq. 2.18 in Eq. 2.16 to get the following expression:

$$P_{fV} = 1 - exp\left[- \int_V \left[\int_0^{\sigma_{emax}} \frac{\Omega(\Sigma, \sigma_{cr})}{4\pi} \frac{dN_V(\sigma_{cr})}{d\sigma_{cr}} d\sigma_{cr} \right] dV \right] \tag{2.20}$$

The integration limits signify that for any given crack, the σ_{cr} can vary from 0 to σ_{emax}. On substituting Eq. 2.19 into Eq. 2.20, the σ_{cr} is replaced by σ_e as implied by the case for $H(\sigma_e, \sigma_{cr})$ where $\sigma_e \geq \sigma_{cr}$. This is done to cover the flaws on which the effective stress exceeds their critical stress. Therefore, their crack density functions is written as:

$$N_V(\sigma_e) = k_{BV} \sigma_e^{m_V}(x, y, z, \alpha, \beta) \tag{2.21}$$

Substituting the $N_V(\sigma_e)$ and $\Omega(\Sigma, \sigma_{cr})$, in Eq. 2.20, and integrating with respect to σ_{cr} we get the following form:

$$P_{fV} = 1 - exp\left[-\frac{2}{\pi}\int_V \left[\int_0^{\pi/2}\int_0^{\pi/2} N_V(\sigma_e) sin\alpha \; d\alpha \; d\beta\right] dV\right] \tag{2.22}$$

To implement Eq. 2.22 into a finite element method which involves discrete volume elements V_i, with Gaussian integration points at which the failure probability is evaluated, the equation can be used in the following numerical form:

$$P_{fV} = 1 - exp\left[-\frac{2k_{BV}}{\pi}\sum_i^n \left[\int_A \sigma_e^{m_V}(\alpha, \beta) \; dA\right]_i \Delta V_i\right] \tag{2.23}$$

The numerical formulation for the failure probability arising from surface flaws can be derived in a similar manner (following Eq. 2.16 to 2.23) and for the sake of brevity, the final equation involving discrete area elements ΔA_i is presented directly as:

$$P_{fS} = 1 - exp\left[-\frac{2k_{BS}}{\pi}\sum_i^n \left[\int_0^{\pi/2} \sigma_e^{'m_S}(\alpha) \; d\alpha\right]_i \Delta A_i\right] \tag{2.24}$$

2.2.2 Stresses on a Crack

As observed earlier, the crack shape independent models, employ the normal stress σ_n, and the crack shape dependent similarly employ σ_n and additionally the shear stress τ in the calculation for the effective stress σ_e, whose expression depends on the crack orientation in the principal stress space. Hence, to define $sigma_n$ and τ we start by first defining the total stress using the principal stresses and direction cosines for a volume flaws as:

$$\sigma^2 = (\sigma_1 l)^2 + (\sigma_2 m)^2 + (\sigma_3 n)^2 \tag{2.25}$$

and for surface flaws as:

$$\sigma^2 = (\sigma_1 p)^2 + (\sigma_2 o)^2 \tag{2.26}$$

where $l = cos\alpha$, $m = sin\alpha \; cos\beta$, and $n = sin\alpha \; sin\beta$; are the direction cosines for the traction vector σ as shown in Figure 2.3.

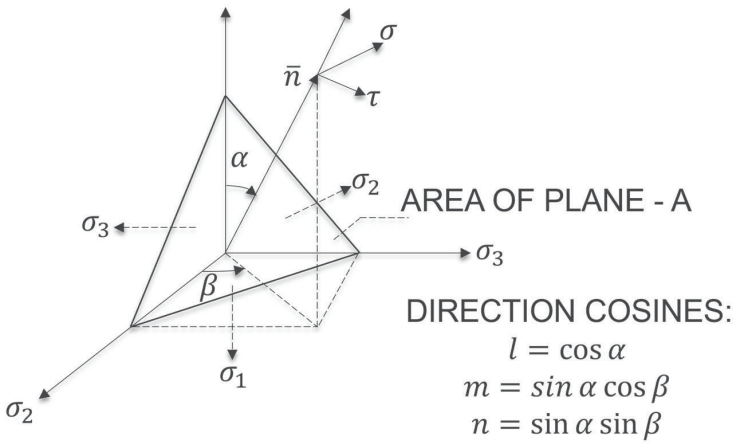

Figure 2.3: Direction cosines l, m, n of the stress tensor σ in principal stress space.

Based on the above figure, the normal stress on the crack plane is defined for volume flaws as:

$$\sigma_n = \sigma_1 l^2 + \sigma_2 m^2 + \sigma_3 n^2 \tag{2.27}$$

and the shear stress component as:

$$\tau^2 = \sigma^2 - \sigma_n^2 \tag{2.28}$$

Similarly, for surface flaws, the direction cosines in a projected frame of reference of σ_1' and σ_2' are $o = sin\gamma$, $p = cos\gamma$ where $\gamma \equiv \alpha$ and:

$$\sigma_n' = \sigma_1' p^2 + \sigma_2' o^2 \tag{2.29}$$

and the shear stress component as:

$$\tau'^2 = \sigma'^2 - \sigma_n'^2 \tag{2.30}$$

2.2.3 Mixed-Mode Failure Criterion

To evaluate the effective stress σ_e, the crack shape and fracture criteria must be specified. The criteria shown in the flow-chart (Fig. 2.1 and 2.2) are adopted from the literature and implemented here.

2.2.4 Maximum Tensile (MTS) Criterion

According to Batdorf and Heinisch [18] the assumption that fracture occurs when the maximum stress on the surface of the crack cavity reaches the ultimate strength of the material, leads to the MTS criterion that depends on the crack shape.

2.2.4.1 Volume flaws

For volume flaws, the effective stress solution under this criterion in the case of a Griffith flaw is:

$$\sigma_e = \frac{1}{2}\left(\sigma_n + \sqrt{\sigma_n^2 + \tau^2}\right) \tag{2.31}$$

whereas the solution for a Penny shaped flaw (which has greater shear sensitivity) is:

$$\sigma_e = \frac{1}{2}\left(\sigma_n + \sqrt{\sigma_n^2 + \left(\frac{\tau}{1 - 0.5\nu}\right)^2}\right) \tag{2.32}$$

where ν is the Poisson ratio.

2.2.4.2 Surface flaws

For surface flaws, the effective stress solution under this criterion in the case of a Griffith flaw is the same as the one for volume flaws:

$$\sigma_e' = \frac{1}{2}\left(\sigma_n' + \sqrt{\sigma_n'^2 + \tau'^2}\right) \tag{2.33}$$

The MTS criterion ignores the different modes of crack extension.

2.2.5 Total Co-planar Strain Energy (CSE) Release Rate Criterion

The CSE criterion is calculated from the total strain energy release rate is expressed in terms of the different modes of loading as:

$$G_T = G_I + G_{II} + G_{III} \tag{2.34}$$

The above equation can be re-written in terms of the stress intensity factor (K_{Ic}) as:

$$K_{Ic}^2 = K_I^2 + K_{II}^2 + \frac{K_{III}^2}{1-\nu} \tag{2.35}$$

which becomes a criterion to help derive the solution for the effective stress. Here $K_I = \sigma_n\sqrt{\pi a}$ and $K_{II} = \tau\sqrt{\pi a}$ where $2a$ is the crack length, and K_{III} is not defined as mode-I and mode-II are considered to be dominant.

2.2.5.1 Volume Flaws

For volume flaws, in case of a Griffith flaw the solution for effective stress is:

$$\sigma_e = \sqrt{\sigma_n^2 + \tau^2} \tag{2.36}$$

whereas the solution for a Penny shaped flaw (which has greater shear sensitivity) is:

$$\sigma_e = \sqrt{\sigma_n^2 + \left(\frac{\tau}{1-0.5\nu}\right)^2} \tag{2.37}$$

The above two criteria are formulated assuming plane strain condition, and that the cracks grow/extend in their own plane, an assumption that can lead to too high fracture stress [18].

2.2.5.2 Surface flaws

In case of surface flaws, the CSE model is formulated using the stress intensity factors, similar to the method used for volume-based flaws. For a Griffith flaw, Modes I and II are assumed to be dominant, and hence, the factors $K_I = \sigma_n\sqrt{\pi a}$ and $K_{II} = \tau\sqrt{\pi a}$ are used to derive the equivalent stress as:

$$\sigma_e' = \sqrt{\sigma_n'^2 + \tau'^2} \tag{2.38}$$

For a Griffith notch flaw shape the factors $K_I = 1.1215\ \sigma_n\sqrt{\pi a}$ and $K_{III} = \tau\sqrt{\pi a}$ [23, 21] are used to derive the equivalent stress as:

$$\sigma_e' = \sqrt{\sigma_n'^2 + \frac{0.7951}{1-\nu}\tau'^2} \tag{2.39}$$

Note: The CSE criterion is agnostic to the sign of σ_n and τ used in the above equations, as the terms are squared.

2.2.6 Shetty's Mixed-Mode (SMM) Criterion

Shetty in his work [16] implemented a modified equation proposed by Palaniswamy and Knauss [24], on the mixed-mode fracture of structural ceramics, based on the stress intensity factors. The equation's final form is:

$$\frac{K_I}{K_{IC}} + \left(\frac{K_\delta}{\overline{C} K_{IC}}\right)^2 = 1 \tag{2.40}$$

where K_δ can be either K_{II} or K_{III}, whichever is dominant and $\overline{C}$ is an empirical constant adjusted to best fit the data. Shetty found a range values of $0.8 \leq \overline{C} \leq 2$ for materials such as soda-lime glass and various ceramics with large cracks. The value of $\overline{C}$ is proportional to shear insensitivity in the above equation.

2.2.6.1 Volume flaws

Substituting the normal and shear stresses in Eq. 2.40, the equivalent stress solution in case of volume flaws for a Griffith flaw is:

$$\sigma_e = \frac{1}{2}\left[\sigma_n + \sqrt{\sigma_n^2 + \left(\frac{2\tau}{\overline{C}}\right)^2}\right] \tag{2.41}$$

and for a Penny-shaped flaw the solution is:

$$\sigma_e = \frac{1}{2}\left[\sigma_n + \sqrt{\sigma_n^2 + \left(\frac{2\tau}{\overline{C}(2-\nu)}\right)^2}\right] \tag{2.42}$$

2.2.6.2 Surface flaws

In case of surface flaws, the noncoplanar strain energy release rate model (similar to the Shetty mixed-mode model) provides a solution for the effective stress

2.2.7 Noncoplanar Strain Energy (NCSE) Release Rate Criterion

2.2.7.1 Surface flaws

The NCSE Criterion, like SMM is also based on the stress intensity factors and similar to the approach for volume-based flaws, it is formulated using the equation:

$$\frac{K_I}{K_{IC}} + \left(\frac{K_\delta}{\overline{C} K_{IC}}\right)^2 = 1 \tag{2.43}$$

where K_δ is either K_{II} or K_{III}, based on which is dominant and $\overline{C}$ is an empirical constant adjusted to fit the data. Using the above relation and assuming mode I and II dominate for a Griffith flaw the equivalent stress is derived as follows:

$$\sigma_e' = \frac{1}{2}\left[\sigma_n' + \sqrt{\sigma_n'^2 + \left(\frac{2\tau'}{\overline{C}}\right)^2}\right] \tag{2.44}$$

and for a Griffith notch the equivalent stress is:

$$\sigma'_e = \frac{1}{2}\left[\sigma'_n + \sqrt{\sigma'^2_n + 3.1803\left(\frac{\tau'}{\overline{C}}\right)^2}\right] \tag{2.45}$$

Lastly, for a semi-circular crack the equivalent stress is derived by taking $K_I = 1.366\sigma_n\sqrt{a}$, $K_{II} = 1.241\tau\sqrt{a}$, and $K_{III} = 0.133\sqrt{a}$ [25, 26]. On neglecting the effect of K_{III} the expression derived is:

$$\sigma'_e = \frac{1}{2}\left[\sigma'_n + \sqrt{\sigma'^2_n + 3.301\left(\frac{\tau'}{\overline{C}}\right)^2}\right] \tag{2.46}$$

The NCSE criterion does not have an effective stress solution for volume flaws.

Note: In the models that consider compressive stresses, an additional heuristic is made. When the principal compressive stresses exceed the maximum principal tensile stress by a factor of three (for the same element), the corresponding failure probability is set to zero, following the CARES manual specification [10].

2.3 Shear-Sensitivity Analysis

The PIA and WNTSA failure models mentioned earlier are inherently shear-insensitive because they assume only Mode I fracture to occur and ignore the shear-stresses. The Batdorf models on the other hand are shear-sensitive as they consider the shear-stress term in their analytical equations and assume multi-modal fracture to occur. In addition, the shear-sensitivity amongst the Batdorf models is affected by the choice of normalized Batdorf crack density coefficient ($\overline{k}_B$) introduced in Eq. 2.23, 2.24, and the Shetty mixed mode empirical constant $\overline{C}$ introduced in Eq. 2.40. We illustrate this in the following section.

2.3.1 Normalized Batdorf crack density coefficient ($\overline{k}_B$)

The parameter k_B is estimated from the normalized Batdorf crack density coefficient ($\overline{k}_B$) as mentioned in the CARES manual [10]:

$$k_B = \overline{k}_B.k_w \tag{2.47}$$

where, $\overline{k}_B$ can either be evaluated by (i) a fixed expression: $\overline{k}_B = 2m + 1$ for each Batdorf model or, (ii) it can be evaluated numerically based on the mixed-mode fracture criteria. The former evaluation is designated as a "shear-insensitive" case while the latter evaluation is designated as a "shear-sensitive" case by the CARES manual. In the (ii) method, the risk of rupture in a polyaxial Batdorf theory is equated to that of a uniaxial Weibull model, for an imposed uniaxial stress state. The risk of rupture is the integral of the crack density function ($N(\sigma)$) as shown in Eq. 2.1.

2.3.1.1 Volume flaws

For an imposed uniaxial stress state of magnitude σ_1, and assuming volume-based flaws, the expression of $\overline{k}_B$ is as follows:

$$\overline{k}_{BV} = \frac{\pi}{2\int_0^{\pi/2}\left(\int_0^{\pi/2}\left(\frac{\sigma_e(\sigma_1,\alpha,\beta)}{\sigma_1}\right)^{m_v} sin\alpha\ d\alpha\right)d\beta} \tag{2.48}$$

The expression for $\overline{k}_{BV}$ depends on the equivalent stress σ_e which is based on the fracture criteria mentioned in Section 2.2. For each fracture criterion, the $\overline{k}_{BV}$ is analytically derived considering volume flaws and presented as follows:

1. *MTS: GF*

$$\overline{k}_{BV} = \frac{\pi}{2\int_0^{\pi/2}\left(\int_0^{\pi/2}\left(\frac{1}{2}\left(cos\alpha^2+\sqrt{cos\alpha^4+cos\alpha^2 sin\alpha^2}\right)\right)^{m_v} sin\alpha\ d\alpha\right)d\beta} \tag{2.49}$$

2. *MTS: PSF*

$$\overline{k}_{BV} = \frac{\pi}{2\int_0^{\pi/2}\left(\int_0^{\pi/2}\left(\frac{1}{2}\left(cos\alpha^2+\sqrt{cos\alpha^4+\frac{sin2\alpha^2}{(2-\nu)^2}}\right)\right)^{m_v} sin\alpha\ d\alpha\right)d\beta} \tag{2.50}$$

3. *CSE: GF*

$$\overline{k}_{BV} = \frac{\pi}{2\int_0^{\pi/2}\left(\int_0^{\pi/2}(cos\alpha)^{m_v} sin\alpha\ d\alpha\right)d\beta} \tag{2.51}$$

4. *CSE: PSF*

$$\overline{k}_{BV} = \frac{\pi}{2\int_0^{\pi/2}\left(\int_0^{\pi/2}\left(\sqrt{cos\alpha^4+\left(\frac{sin2\alpha}{2-\nu}\right)^2}\right)^{m_v} sin\alpha\ d\alpha\right)d\beta} \tag{2.52}$$

5. *SMM: GF*

$$\overline{k}_{BV} = \frac{\pi}{2\int_0^{\pi/2}\left(\int_0^{\pi/2}\left(\frac{1}{2}\left(cos\alpha^2+\sqrt{cos\alpha^4+\left(\frac{sin2\alpha}{\overline{C}}\right)}\right)\right)^{m_v} sin\alpha\ d\alpha\right)d\beta} \tag{2.53}$$

6. *SMM: PSF*

$$\overline{k}_{BV} = \frac{\pi}{2\int_0^{\pi/2}\left(\int_0^{\pi/2}\left(\frac{1}{2}\left(cos\alpha^2+\sqrt{cos\alpha^4+4\left(\frac{sin2\alpha}{\overline{C}(\nu-2)}\right)^2}\right)\right)^{m_v} sin\alpha\ d\alpha\right)d\beta} \tag{2.54}$$

2.3.1.2 Surface flaws

In case of surface flaws, too the PIA and WNTSA models are inherently shear-insensitive, and the Batdorf models are shear-sensitive. The shear-sensitivity amongst the Batdorf models is affected by the choice of $\overline{k}_B$ and $\overline{C}$. As done for volume flaws, $\overline{k}_B$ can be defined for each Batdorf model using (i) a closed-form solution from Eq. 2.55

$$\overline{k}_{BS} = \frac{k_{BS}}{k_{wS}} = \frac{m_S\sqrt{\pi}\Gamma(m_S)}{\Gamma\left(m_S + \frac{1}{2}\right)} \tag{2.55}$$

or, (ii) it can be evaluated numerically based on the fracture criteria. The former method is designated as a "shear-insensitive" case while the latter method is designated as a "shear-sensitive" case by the CARES manual. In the latter method, we equate the risk of rupture in a polyaxial Batdorf theory to that of a uniaxial Weibull model, for an imposed uniaxial stress state. For the imposed uniaxial stress state of magnitude σ_1, and assuming surface-based flaws, the expression for $\overline{k}_B$ is as follows:

$$\overline{k}_{BS} = \frac{\pi}{2\displaystyle\int_0^{\pi/2}\left(\frac{\sigma_e(\sigma_1,\alpha)}{\sigma_1}\right)^{m_S} d\alpha} \tag{2.56}$$

The expression for $\overline{k}_{BS}$ is based on the equivalent stress σ_e which is based on the fracture criteria. For each fracture criterion, the $\overline{k}_{BS}$ is analytically derived considering surface flaws and presented as follows::

1. *MTS: GF*

$$\overline{k}_{BS} = \frac{\pi}{2\displaystyle\int_0^{\pi/2}\left(\frac{1}{2}\left(cos\alpha^2 + cos\alpha\right)\right)^{m_S} d\alpha} \tag{2.57}$$

2. *CSE: GF*

$$\overline{k}_{BS} = \frac{\pi}{2\displaystyle\int_0^{\pi/2}(cos\alpha)^{m_S}\ d\alpha} \equiv \frac{m_S\sqrt{\pi}\Gamma(m_S/2)}{2\Gamma\left(\frac{m_S+1}{2}\right)} \tag{2.58}$$

3. *CSE: GN*

$$\overline{k}_{BS} = \frac{\pi}{2\displaystyle\int_0^{\pi/2}\left(\sqrt{cos\alpha^4 - \frac{0.198775(sin2\alpha)^2}{\nu-1}}\right)^{m_S} d\alpha} \tag{2.59}$$

4. *NCSE: GF*

$$\overline{k}_{BS} = \frac{\pi}{2\displaystyle\int_0^{\pi/2}\frac{1}{2}\left(cos\alpha^2 + \sqrt{cos\alpha^4 + \left(\frac{sin2\alpha}{\overline{C}}\right)^2}\right)^{m_S} d\alpha} \tag{2.60}$$

5. *NCSE: GN*

$$\overline{k}_{BS} = \frac{\pi}{2\int_0^{\pi/2} \frac{1}{2}\left(cos\alpha^2 + \sqrt{cos\alpha^4 + 0.795075\left(\frac{sin2\alpha}{\overline{C}}\right)^2}\right)^{m_S} d\alpha} \tag{2.61}$$

6. *NCSE: SCC*

$$\overline{k}_{BS} = \frac{\pi}{2\int_0^{\pi/2} \frac{1}{2}\left(cos\alpha^2 + \sqrt{cos\alpha^4 + 0.82525\left(\frac{sin2\alpha}{\overline{C}}\right)^2}\right)^{m_S} d\alpha} \tag{2.62}$$

2.3.2 Shetty's empirical constant ($\overline{C}$)

As demonstrated by Shetty [16] the shear-sensitivity within the Batdorf models can also change with different $\overline{C}$ parameter values. When the value of $\overline{C}$ is increased from 0.82 to ∞ the shear-sensitivity goes from being maximum to zero. The change in shear-sensitivity matters when it comes to predicting the failure probability. A demonstration of the effect of shear-sensitivity on the failure probability is shown later in Section 4.3.2.

2.4 Summary

The present chapter presented a suite of failure models built using fracture mechanics theories adopted from the literature. These models are able to predict a time-independent probability of failure for monolithic ceramics. Estimating the probability involves integrating a crack density function that operates on stress tensors and employs material failure properties that are obtained from experiments. The integration is also performed over volume elements for volume flaws and surface elements for surface flaws. The failure models are also categorized differently for the two flaw types and are further sub-categorized based on their dependency on crack shapes. Lastly, the assumption made in this chapter is that the state of stress is constant with time. In the next chapter a time-dependent stat of stress is considered.

3 Time-dependent Failure

In the previous chapter, the stress state was assumed to be constant with time and hence, the resulting failure probability was time-independent and history-independent, where history is with respect to any prior thermomechanical loading. In the present chapter, the effect of time-dependent stresses is considered. Monolithic ceramics when subjected to either stress corrosion, cyclic or dynamic fatigue loads, and even surface phenomena such as oxidation, result in degrading the ceramics' ability to sustain a load over time. This happens due to the growth of the existing non-critical defects (in a stable manner) to a size that makes them critical and results in catastrophic failure. In other words, the cracks that are below the critical size grow to a critical size, when the ceramic is subjected to time-dependent loads ($\sigma(t)$) that are smaller than the inert strength (σ_f). This phenomenon is known as subcritical crack growth [27, 28, 29] as is schematically shown in Figure 3.1.

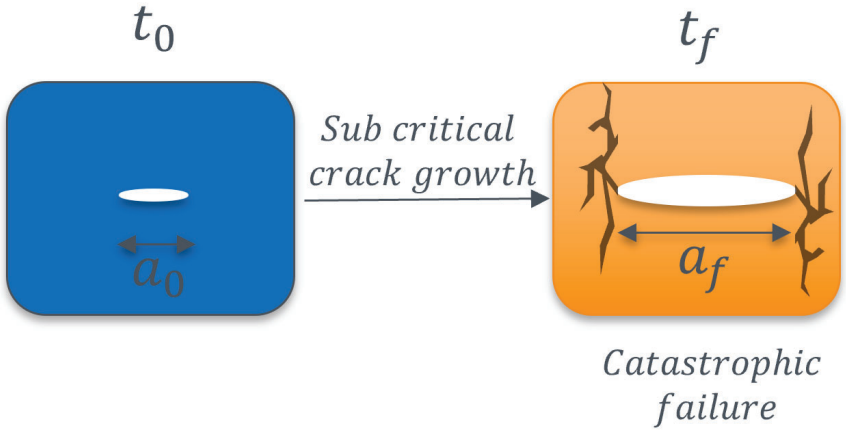

Figure 3.1: Schematic showing occurrence of sub-critical crack growth in a monolithic ceramic. Non-critical flaw of size a_0 at time t_0 grows to critical size a_f and results in catastrophic failure at time t_f.

3.1 Subcritical Crack Growth (SCG)

The work by Wiederhorn [27] presents techniques for characterizing SCG and predicting useful component lifetime (from crack growth) after proof testing, by using crack growth data from different glasses, porcelains, and ceramics such as Aluminum Oxide and Silicon Nitride. Additional works on SCG relevant to the present study include studies by (i) Quinn and Katz [30] on sintered α-SiC which shows the occurrence of SCG only at temperatures beyond 1400 ^{0}C, while (ii) Choi et. al. [31, 29, 32] and Lube et. al. [33] demonstrate an SCG analysis in SiC, Si_3N_4, and Alumina, (iii) Gilbert et. al. [34] demonstrates fatigue crack growth in MAX Phase (Ti_3SiC_2), and finally (iv) the CARES [10] manual by NASA that presents examples of crack growth due to various types of fatigue loading and presents methods for estimating a time-dependent failure probability. The present study adopts the method from CARES and presents it here in a concise manner.

As shown in Figure 3.1, SCG of pre-existing flaws can result in driving them to a critical

length and catastrophic failure, i.e. when the equivalent stress intensity factor is $K_{Ieq} = K_{IC}$. The models developed so far are semi-empirical and can only approximate the phenomenological behavior of SCG because of the complex mechanisms involved. For instance, the recent work by Wang et. al. [5] presents an analytical model for SCG that claims crack growth occurs in a stable manner when K_{Ieq} is equal to a threshold stress intensity factor K_0, where K_0 is approximately 0.3 - 0.8K_{IC}. Similarly in the present study, to account for the effect of SCG, the state of stress in the ceramic is approximated using a transformed equivalent mode I far-field stress σ_{Ieq} normal to the crack. The parameters describing the state of stress during SCG are fatigue parameters denoted by N and B and like the Weibull parameters, they too are classified separately for volume and surface flaws.

3.1.1 Constitutive Equations

The σ_{Ieq} can be derived starting with a relation [10, 35] between crack velocity and stress intensity factor defined as:

$$\frac{da(\psi,t)}{dt} = AK_{Ieq}^{N}(\psi,t) \tag{3.1}$$

where K_{Ieq} is the equivalent mode - I stress intensity factor of polyaxial stress states and it is further defined as:

$$K_{Ieq} = \sigma_{Ieq}(\psi,t)Y\sqrt{a(\psi,t)} \tag{3.2}$$

where $a(t)$ is the crack length, $\psi(x,y,z,\alpha,\beta)$ is the function defining the crack location (x,y,z) within the body, and the crack orientation is defined by (α,β). The term Y is a function of the crack geometry, and, hence, can vary with SCG. The CARES manual [10] assumes it to be a fixed geometric constant based on the crack shape (i.e. $\sqrt{\pi}$ for a Griffith crack or $\dfrac{2}{\sqrt{\pi}}$ for a penny-shaped crack). Lastly, A and N are material/environmental constants. Substituting Eq. (3.2) into (3.1) we get:

$$\frac{da(\psi,t)}{dt} = A\sigma_{Ieq}^{N}(\psi,t)Y^{N}a(\psi,t)^{N/2} \tag{3.3}$$

separating the variables we get:

$$\sigma_{Ieq}^{N}(\psi,t)dt = \frac{1}{AY^{N}}\left(\frac{1}{\sqrt{a(\psi,t)}}\right)^{N} da(\psi,t) \tag{3.4}$$

Integrating Eq. 3.4 using the integration limits (a_0,a_f) representing the critical crack lengths at the start of the loading ($t = 0$) and at failure ($t = t_f$), respectively as shown schematically in Figure 3.2.

$$\int_{t=0}^{t_f} \sigma_{Ieq}^{N}(\psi,t)dt = \frac{1}{AY^{N}}\int_{a=a_0}^{a_f}\left(\frac{1}{\sqrt{a(\psi,t)}}\right)^{N} da(\psi,t) \tag{3.5}$$

The expressions for the critical crack lengths can be derived using the fracture toughness (K_{IC}) i.e. the critical stress intensity factor of the ceramic, under mode-I loading [35], in Eq. (3.2) as:

$$a_0 = \left(\frac{K_{Ic}}{Y\sigma_{Ieq}(\psi, t_0)}\right)^2 \quad \text{and} \quad a_f = \left(\frac{K_{Ic}}{Y\sigma_{Ieq}(\psi, t_f)}\right)^2 \tag{3.6}$$

where $\sigma_{Ieq}(\psi, t_0)$ is the critical effective stress [10] distribution in the ceramic when SCG begins, and will be denoted by $\sigma_{Ieq,0}(\psi)$, hereafter. The term $\sigma_{Ieq}(\psi, t_f)$ addresses the final distribution of flaws, which occur at the point at which the equivalent stress equals the instantaneous failure strength (or inert strength [36]) at t_f. On integrating Eq. 3.5:

$$\int_0^{t_f} \sigma_{Ieq}^N(\psi, t)dt = \left(\frac{2}{AY^2(N-2)K_{Ic}^{N-2}}\right)\sigma_{Ieq,0}^{N-2}(\psi)\left[1 - \left(\frac{\sigma_{Ieq}(\psi, t_f)}{\sigma_{Ieq,0}(\psi)}\right)^{N-2}\right] \tag{3.7}$$

The bracketed term can be compacted as the coefficient:

$$B = \left(\frac{2}{AY^2(N-2)K_{Ic}^{N-2}}\right) \tag{3.8}$$

From Eq. 3.7 the (reduced) equivalent stress after SCG can be expressed as:

$$\sigma_{Ieq}^{N-2}(\psi, t_f) = \sigma_{Ieq,0}^{N-2}(\psi) - \frac{\int_0^{t_f} \sigma_{Ieq}^N(\psi, t)dt}{B} \tag{3.9}$$

The above equation can be rearranged to express $\sigma_{Ieq,0}(\psi)$ as a transformed equivalent mode-I stress (Eq. 3.10) that evolves with time (t) to account for the effects of SCG up till failure (t_f) as shown schematically in Figure 3.2. If $t_f = 0$ i.e. in the absence of SCG, the first term vanishes and the expression corresponds to the fast-fracture stress. The model parameters N and B describe the state of stress during SCG and are known as the fatigue parameters, determined from experiments.

$$\boxed{\sigma_{Ieq,0}(\psi) = \left[\frac{\int_0^{t_f} \sigma_{Ieq}^N(\psi, t)dt}{B} + \sigma_{Ieq}^{N-2}(\psi, t_f)\right]^{1/(N-2)}} \tag{3.10}$$

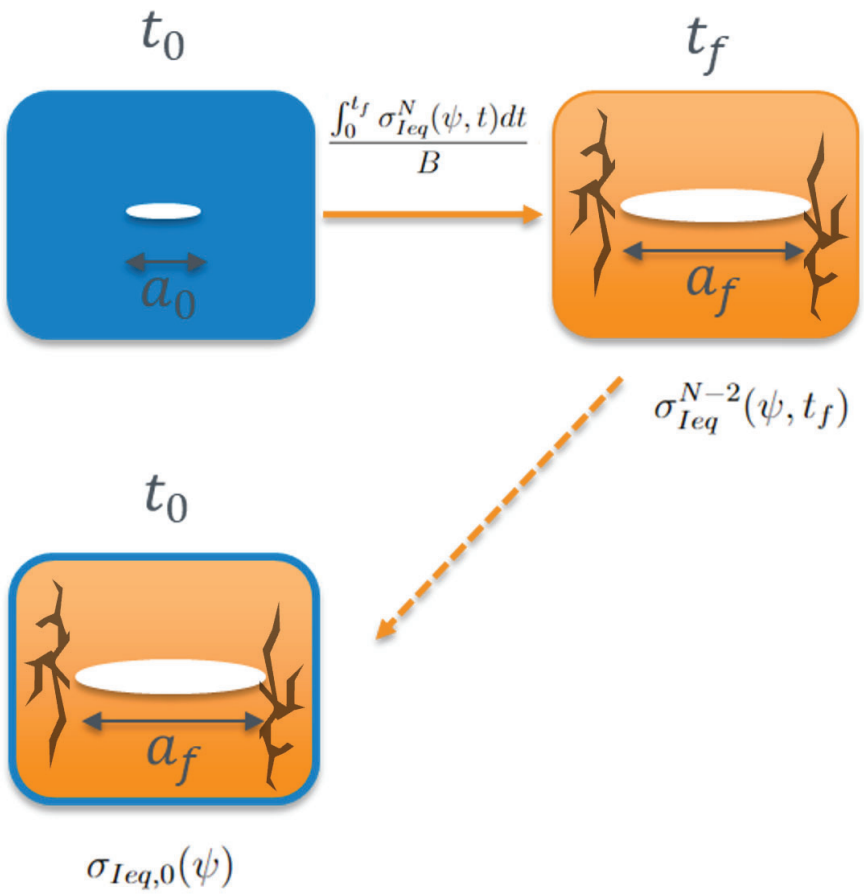

Figure 3.2: Schematic showing occurrence of sub-critical crack growth in a monolithic ceramic and approximating the phenomenon using the transformed equivalent mode-I stress.

3.1.2 Failure Probability

The time-dependent stress $\sigma_{Ieq,0}(\psi)$ is used to estimate a time-dependent failure probability $P_f(t_f)$ when the ceramic undergoes SCG. The estimation is dependent on the chosen fracture criterion, flaw type, crack shape, and given time to failure t_f or service life. Hence, it is determined from the known: (i) principal stresses (for the PIA model), (ii) normal tensile stress (for the WNTSA model), and (iii) equivalent stress (for the Batdorf models). In case of volume flaws the 3D stresses are used, while in case of surface flaws, the 2D in-plane stresses are used.

3.1.2.1 Volume Flaws

The numerical solutions for the time-dependent failure probability from each model while considering volume flaws are as follows:

- PIA

$$P_{fV}(t_f) = 1 - exp\left[-k_{wV}\sum_{i}^{n}(\sigma_{I1,0}^{m_v} + \sigma_{I2,0}^{m_v} + \sigma_{I3,0}^{m_v})_i \Delta V_i\right] \tag{3.11}$$

- WNTSA

$$P_{fV}(t_f) = 1 - exp\left[-k_{wpV}\sum_{i}^{n}(\overline{\sigma_{In,0}}^{m_V})_i \Delta V_i\right] \tag{3.12}$$

- Batdorf models

$$P_{fV}(t_f) = 1 - exp\left[-\frac{k_{BV}}{2\pi}\sum_{i=1}^{n}\left(\int_0^{2\pi}\int_0^{\pi/2}[\sigma_{Ieq,0}(\psi)]^{m_V} sin\alpha \; d\alpha \; d\beta\right)_i \Delta V_i\right] \tag{3.13}$$

3.1.2.2 Surface Flaws

The time-dependent failure probability from each model while considering surface based flaws are as follows:

- PIA

$$P_{fS}(t_f) = 1 - exp\left[-k_{wS}\sum_{i}^{n}(\sigma_{I1,0}^{'m_S} + \sigma_{I2,0}^{'m_S})_i \Delta A_i\right] \tag{3.14}$$

- WNTSA

$$P_{fS}(t_f) = 1 - exp\left[-k_{wpS}\sum_{i}^{n}(\overline{\sigma'_{In,0}}^{m_S})_i \Delta A_i\right] \tag{3.15}$$

- Batdorf models

$$P_{fS}(t_f) = 1 - exp\left[-\frac{2k_{BS}}{\pi}\sum_{i=1}^{n}\left(\int_0^{\pi/2}[\sigma'_{Ieq,0}(\psi)]^{m_S} \; d\alpha\right)_i \Delta A_i\right] \tag{3.16}$$

3.1.2.3 Combined Failure Probability

A combined failure probability for each the models is evaluated by considering both volume and surface flaws and summing up their *log reliabilities* i.e. the terms within the integrals of Eq. 2.1 as follows:

$$P_f(t_f) = 1 - exp\left[-\left(\int_V N(\sigma)dV + \int_A N(\sigma')dA\right)\right] \tag{3.17}$$

The result for each model is equivalent to adding the terms within the [ ] of the $exp[\,]$ term for volume and surface flaws.

3.2 Types of Loading

As mentioned earlier SCG can occur due to different types of time-dependent loading conditions which essentially cause fatigue in the ceramic. The transformed equivalent mode-I stress in Eq. 3.10 is dependent on the type of fatigue load applied to the ceramic as its equation is formulated accordingly. The flowchart shown in Fig. 3.3 presents the typical fatigue loading conditions, and the following sections present the equations for the $\sigma_{Ieq,0}(\psi)$ corresponding to them.

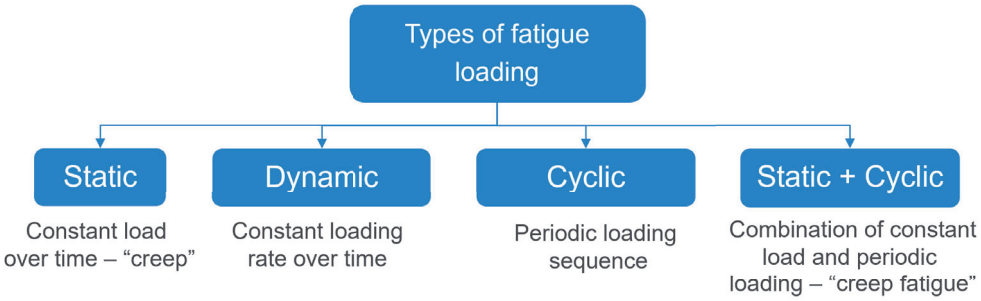

Figure 3.3: Flowchart showing the typical types of fatigue loading that can result in subcritical crack growth.

3.2.1 Static Fatigue (Creep)

This type of fatigue involves a constant load (or stress) applied over a time t. The transformed equivalent mode-I stress is defined as:

$$\begin{aligned} \sigma_{Ieq}(\psi, t) &= \sigma_{Ieq}(\psi) \\ \sigma_{Ieq,0}(\psi) &= \left[\frac{\sigma_{Ieq}^{N}(\psi)\ t_f}{B} + \sigma_{Ieq}^{N-2}(\psi) \right]^{1/N-2} \end{aligned} \tag{3.18}$$

3.2.2 Dynamic Fatigue

This type of fatigue involves a constant loading rate (or stress rate) applied over a time t. The transformed equivalent mode-I stress is defined as:

$$\begin{aligned}\sigma_{Ieq}(\psi,t) &= \dot{\sigma}_{Ieq}(\psi)t \\ \sigma_{Ieq,0}(\psi) &= \left[\frac{(\dot{\sigma}_{Ieq}(\psi))^N\ t_f^{N+1}}{B\ (N+1)} + (\dot{\sigma}_{Ieq}(\psi)\ t_f)^{N-2}\right]^{1/N-2} \\ &= \left[\frac{(\sigma_{Ieq}(\psi,t_f))^N\ t_f}{B\ (N+1)} + (\sigma_{Ieq}(\psi,t_f))^{N-2}\right]^{1/N-2}\end{aligned} \tag{3.19}$$

3.2.3 Cylic Fatigue

This type of fatigue involves applying a periodic loading sequence (with a period T for one cycle), and the applied cyclic load (σ_{Ieqc}) is converted to an equivalent static load (σ_{Ieq}, equivalent in the sense of crack growth) over the same time interval as follows:

$$\int_0^T \sigma_{Ieqc}^N(\psi,t)dt = \sigma_{Ieq}^N(\psi)T \tag{3.20}$$

rearranging the equation we get:

$$\sigma_{Ieq}^N(\psi) = \left[\frac{\int_0^T \sigma_{Ieqc}^N(\psi,t)dt}{T}\right] = \sigma_{Ieqc_{max}}^N(\psi)\underbrace{\left[\frac{\int_0^T \frac{\sigma_{Ieqc}^N(\psi,t)}{\sigma_{Ieqc_{max}}^N(\psi)}dt}{T}\right]}_{g(\psi)} = \sigma_{Ieqc_{max}}^N(\psi)g(\psi) \tag{3.21}$$

where $\sigma_{Ieqc_{max}}(\psi)$ is the maximum stress of the periodic loading over a time T, and $g(\psi)$ is known as a g-factor which describes the stress gradient across the specimen and is evaluated numerically. Eq. 3.21 can be used to describe static (creep) fatigue as well when $g(\psi) = 1$, as the numerator becomes independent of time. For n multiple, but different, cyclic loads over a time interval of $t_n = t_f$, the equivalent static stress is defined as:

$$\begin{aligned}\sigma_{Ieq}(\psi)t_f &= \int_0^{t_1} \sigma_1^N(\psi,t)dt + \int_{t_1}^{t_2} \sigma_2^N(\psi,t)dt + ... + \int_{t_{n-1}}^{t_n} \sigma_n^N(\psi,t)dt \\ &= \sigma_{Ieqc_{max}}^N(\psi)g(\psi)t_f\end{aligned} \tag{3.22}$$

Finally,

$$\sigma_{Ieq,0}(\psi) = \left[\frac{\sigma_{Ieqc_{max}}^N(\psi)\ t_f\ g(\psi)}{B} + \sigma_{Ieqc_{max}}(\psi)^{N-2}\right]^{1/N-2} \tag{3.23}$$

3.2.4 Static + Cyclic Fatigue

This type of fatigue involves applying a combination of constant and cyclic load that varies as a function of time and generates static and cyclic fatigue, that results in enhancing the crack growth. An empirical method was developed by Dauskardt et. al. [37] using a Walker modification [38] of the Paris law to express the crack growth increment over each cycle, and model cyclic effects. It involved using the applied min and max values of the cyclic stresses, as follows:

$$\sigma_{Ieq,0}(\psi) = \left[\frac{\int_{n=0}^{n_f} \left(1 - \frac{\sigma_{Ieqc_{min}}(\psi,n)}{\sigma_{Ieqc_{max}}(\psi,n)}\right)^{Q} \sigma^{N}_{Ieqc_{max}}(\psi,n)dn}{B} + \sigma^{N-2}_{Ieqc_{max}}(\psi,n_f) \right] \tag{3.24}$$

where N, Q, and B are the cyclic fatigue parameters determined from experiments. For a periodic cyclic stress, the terms inside the integral become independent of number of cycles (n):

$$\sigma_{Ieq,0}(\psi) = \left[\frac{\left(1 - \frac{\sigma_{Ieqc_{min}}(\psi)}{\sigma_{Ieqc_{max}}(\psi)}\right)^{Q} \sigma^{N-2}_{Ieqc_{max}}(\psi).n_f}{B} + \sigma^{N-2}_{Ieqc_{max}}(\psi) \right] \tag{3.25}$$

The above equation can be reduced for a static fatigue case by equating $\sigma_{Ieqc_{max}} = \sigma_{Ieqc_{min}}$. The equation can also be expressed with respect to time as follows:

$$\sigma_{Ieq,0}(\psi) = \left[\frac{\frac{t_i}{t_{cycle}} \int_{0}^{t_{cycle}} \sigma^{N}_{Ieqc}(\psi,t')dt'}{B} + \sigma^{N-2}_{Ieqc}(\psi,t_f) \right]^{1/N-2} \tag{3.26}$$

where t_i is the duration of interest up till which static + cyclic fatigue occurs and t_{cycle} is the the duration of one cycle. In case failure, $t_i = t_f$.

3.3 Summary

The present chapter introduced the concept of subcritical crack growth in monolithic ceramics wherein on applying a time-dependent stress state, the ceramic's ability to sustain load over time degrades. A phenomenological approach to modeling the stress state is introduced and applied to the models discussed in the previous chapter, to predict a time-dependent failure probability. The working of the models is demonstrated in the next chapter.

4 Implementation of Models in srlife

The models presented in the previous two chapters were incorporated into *srlife* to extend its capabilities in predicting the failure of ceramic structures. Since *srlife* is built for concentrated solar power (CSP) receivers, it accounts for the thermal and structural loading experienced by the receiver. These loads are frequent and transient, caused by the day-night cycles, and the resulting stresses generated in the material of the receiver tubes are time-dependent. Therefore, the models predicting the material behavior of the receiver tubes must be time-dependent to account for the effects of such stresses. The models presented in Chapter 3 account for such time-dependent stresses in ceramic structures and hence, were incorporated in *srlife* to predict a time-dependent failure probability (or reliability) of ceramic receivers. The models were specifically incorporated into the reliability module of *srlife* that gives the reliability of each tube, panel, and the overall receiver, for volume-based and surface-based flaws. A combined reliability from both the flaws is also calculated. The present chapter presents a validation of the above.

4.1 Verification

To validate the models incorporated an example problem from the CARES manual [10] was used as it provided the results to compare. The example problem statement is as follows.

4.1.1 Example Problem

An annular disk made of Silicon Nitride (shown in Fig. 4.2) is subjected to an isothermal condition and rotated at various constant and cyclic angular speeds. Based on the resulting stresses, a time-dependent probability of failure for the disk is calculated for a given service life (t_f). The constant angular speed results in constant stresses which generate static (creep) fatigue in the disk. The cyclic angular speeds result in stresses varying with time and generate cyclic fatigue. The probability of failure from volume flaws is evaluated using the PIA, CSE, and SMM models for the GF and PSF crack geometries. Similarly, the probability of failure from surface flaws is evaluated using the PIA, CSE, and NCSE (or SMM) models for the GC and SCC crack geometries. The problem statement is as follows:

1. Dimensions of the annular disk:
   (a) Inner radius: $r_i = 6.35$ mm
   (b) Outer diameter: $r_o = 41.28$ mm
   (c) Thickness: 3.8 mm
2. Isothermal temperature: 1000 ^{o}C
3. Material parameters for Silicon Nitride obtained from literature [39, 28]:
   (a) Weibull modulus (for both volume and surface flaws): $m_V = m_S = 7.65$
   (b) Characteristic strength: $\sigma_\theta = 808$ MPa
   (c) Weibull scale parameter (for volume flaws): $\sigma_{0V} = 74.79$ MPa $(\text{m})^{3/7.65} = 1122.83$ MPa $(\text{mm})^{3/7.65}$

(d) Weibull scale parameter (for surface flaws): σ_{0S} = 232.0 MPa $(\text{m})^{2/7.65}$ = 1411.89 $(\text{mm})^{2/7.65}$

(e) Young's modulus: 289 GPa

(f) Poisson's ratio: 0.219

(g) Density: 3.25*10^3 kg/m^3

(h) Fatigue parameters: $N = 30$, $B = 320$ MPa^2 hr

4. Angular speeds considered: ω = 60,000 rpm to 120,000 rpm

(a) For static fatigue cases: The angular speeds are kept constant

(b) For cyclic fatigue cases: The angular speeds are varied between two fixed speeds, in a sinusoidal manner with a period of 36 sec or 0.01 h as shown in Fig. 4.1

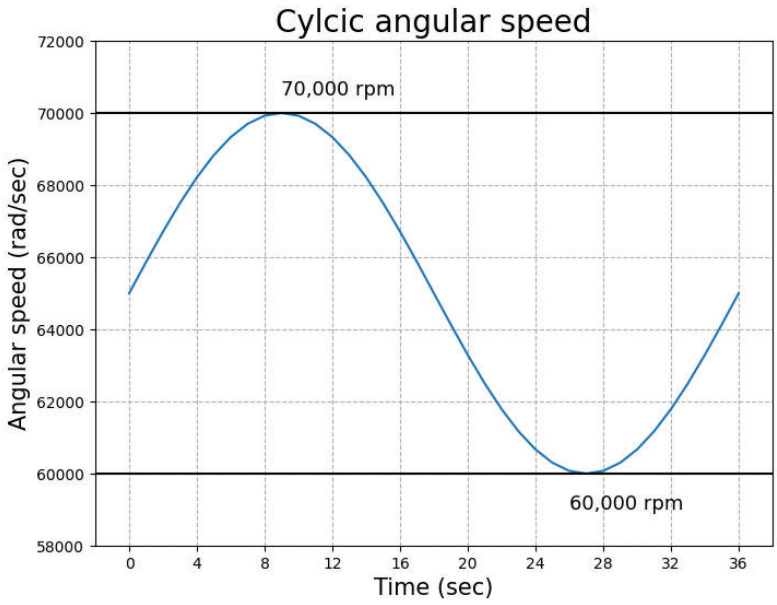

Figure 4.1: Angular speed varying in a sinusoidal manner between 60,000 rpm to 70,000 rpm

To simulate the forces inside the disk during rotation the following body force (Eq. 4.1) was applied with units: r in mm, ω in rad/sec, ρ in mg/mm^3. In Eq. 4.2, T = time, $\omega_{max} = 70,000$ rpm, $\omega_{min} = 60,000$ rpm, and the period is P = 0.01 h.

$$\begin{aligned} \vec{b} &= \rho\omega^2 r \\ b_x &= \rho\omega^2 r Cos(\theta) = \rho\omega^2 x \\ b_y &= \rho\omega^2 r Sin(\theta) = \rho\omega^2 y \end{aligned} \tag{4.1}$$

$$\omega = \left(\frac{\omega_{max} + \omega_{min}}{2}\right) + \left(\frac{\omega_{max} - \omega_{min}}{2}\right) Sin\left[\frac{2\pi}{P} * T\right] \tag{4.2}$$

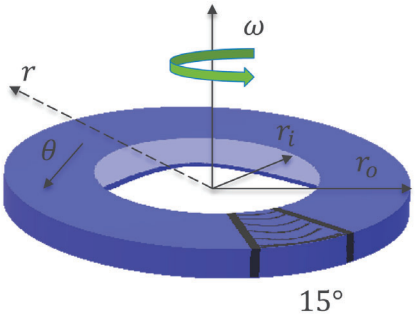

Figure 4.2: Rotating annular disk with a 15^o segment used in CARES

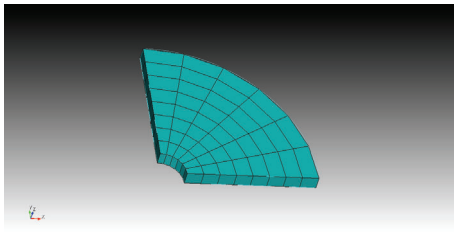

Figure 4.3: Mesh of annular disk for a 90^o segment used for *srlife*

To evaluate the stresses generated in the disk from the rotation, in the CARES manual, the stresses were determined by conducting a finite element analysis (FEA) on a 15^o segment of the disk as shown in Fig. 4.2. For the *srlife* model verification, a similar FEA analysis was conducted in the present study by using MOOSE and CUBIT to prepare a quarter symmetric model (90° segment) of the disk as shown in Fig. 4.3. Post FEA, the stresses were extracted from a 15° sector (for volume flaws) as done in the CARES manual, and a 75° sector (for surface flaws). For volume-flaws the 3D stress tensor (σ) was used, while for surface-flaws, the 3D stresses were projected onto the surface elements to evaluate the in-plane stresses (σ') on the surface. This approach is different from the one followed in the CARES manual, in two ways. Firstly, in *srlife* brick elements were used for evaluating the 3D stresses and projecting them on the surface, while in CARES QUAD8 shell elements were used to identify external surfaces and evaluate surface stresses. Secondly, in CARES the shell elements were assigned membrane properties and negligible thickness, and hence, negligible bending stiffness. Therefore, the stresses evaluated on the surface elements from both approaches differ and this difference can be reflected in the reliability analysis.

4.2 Results

Based on the stresses in the finite element segments, the failure probabilities were evaluated with respect to increasing t_f, for (i) each constant angular velocity in the case of static fatigue, and (ii) a varying angular velocity in the case of cyclic fatigue, as done in the CARES manual. The results presented are firstly segregated based on the flaw type and then the loading type. Lastly, the results from *srlife* are compared with the values in the CARES manual to check for accuracy.

4.2.1 Volume-flaws

The results for volume flaws for the following fatigue loading types are:

4.2.1.1 Static (creep) fatigue

The results for the static fatigue loading case are presented in Figure 4.4 (a) - (f) for the different angular velocities. From the comparison plots, it is observed that the failure proba-

bility increases with angular velocity and service life. The failure probability becomes equal to one close to 110k rpm and is one at 120,000 rpm, for all values of service life. This observation is also clear in the plot generated by using only one model i.e. SMM (PSF) in Fig. 4.5. Lastly, it is also observed that the values from the two sources fall close to each other.

4.2.1.2 Cyclic fatigue

The results for the cyclic fatigue loading case are presented in Figures 4.6, 4.7, and 4.8 for the varying angular velocity. From the comparison plots, as expected, the values of the 60k-80k rpm are higher than the values for 60k-70k, and the values increase with service life. It is also observed that the values from the two sources fall close to each other, and the cyclic fatigue results fall in between the static fatigue results.

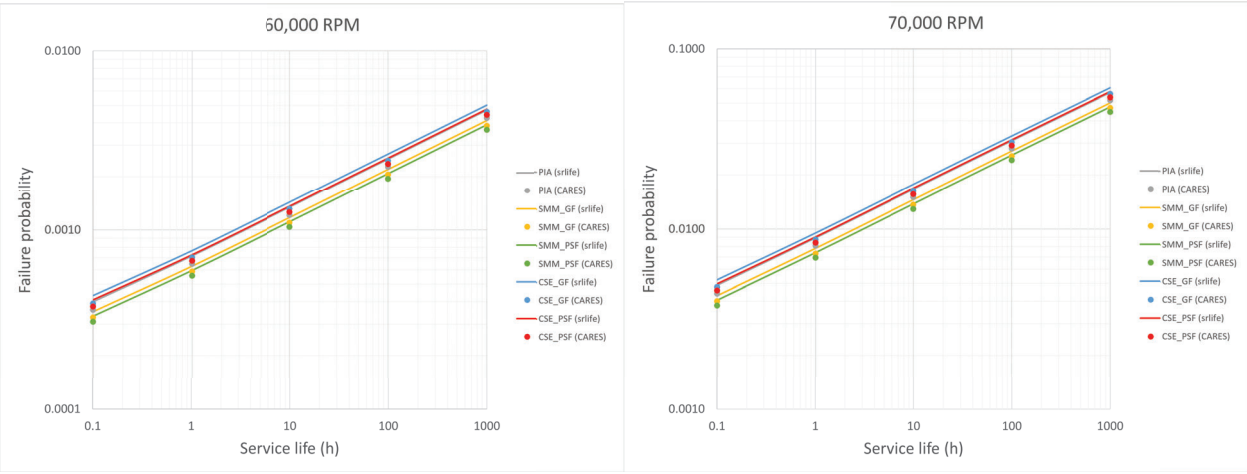

(a) (b)

Figure 4.4: Comparison of failure probabilities at (a) 60,000 rpm (b) 70,000 rpm from CARES manual (symbols) and *srlife* (lines), generated using the models: PIA, CSE, and SMM for GF and PSF flaws

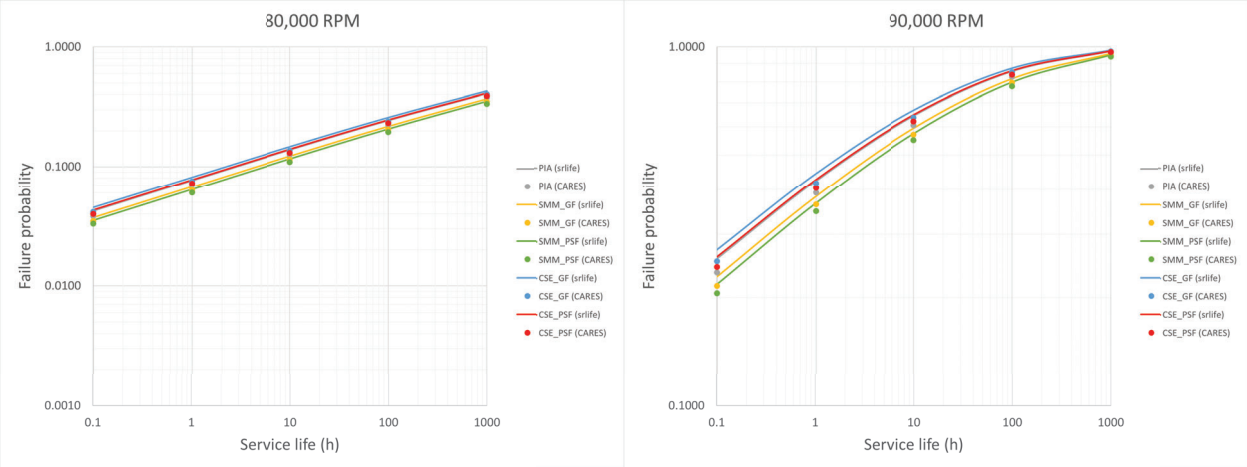

(c) (d)

Figure 4.4: Comparison of failure probabilities at (c) 80,000 rpm (d) 90,000 rpm from CARES manual (symbols) and *srlife* (lines), generated using the models: PIA, CSE, and SMM for GF and PSF flaws

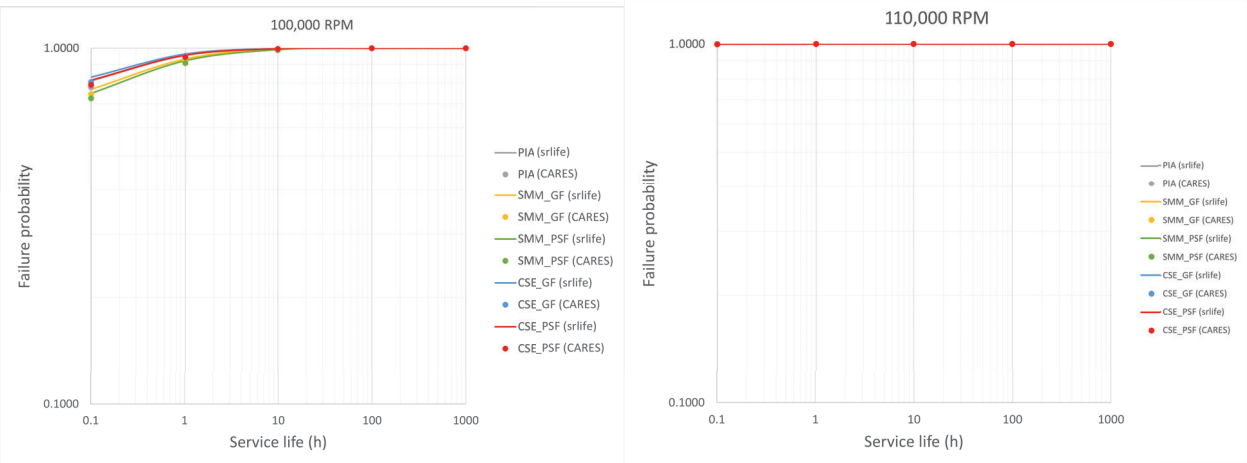

(e) (f)

Figure 4.4: Comparison of failure probabilities at (e) 100,000 rpm (f) 110,000 rpm from CARES manual (symbols) and *srlife* (lines), generated using the models: PIA, CSE, and SMM for GF and PSF flaws

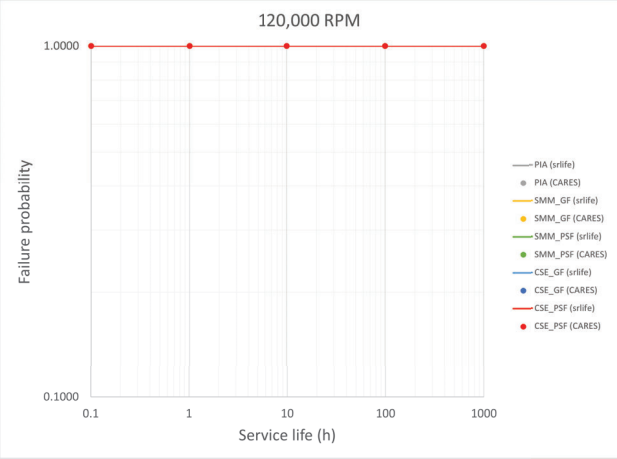

(g)

Figure 4.4: Comparison of failure probabilities at (g) 120,000 rpm from CARES manual (symbols) and *srlife* (lines), generated using the models: PIA, CSE, and SMM for GF and PSF flaws

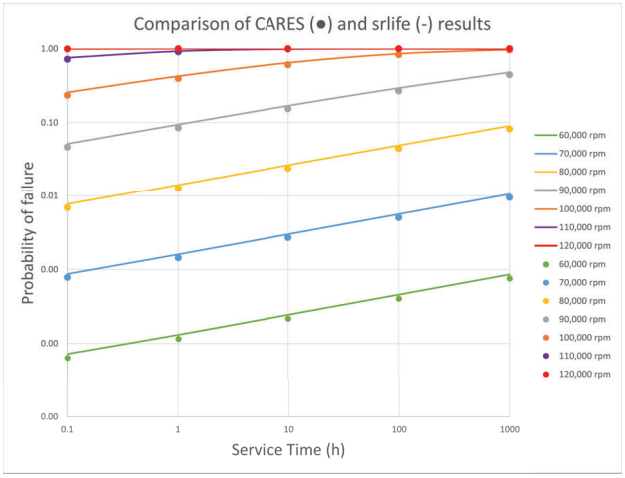

Figure 4.5: Comparison of failure probabilities for all angular velocities from CARES manual (symbols) and *srlife* (lines), generated using the model SMM for penny-shaped flaw (PSF)

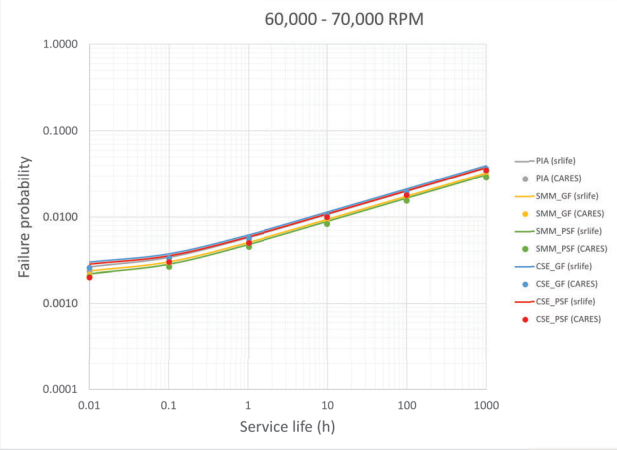

Figure 4.6: Comparison of failure probabilities for angular speeds varying from 60,000 rpm to 70,000 rpm, from CARES manual (symbols) and *srlife* (lines), generated using the models: PIA, CSE, and SMM for GF and PSF flaws

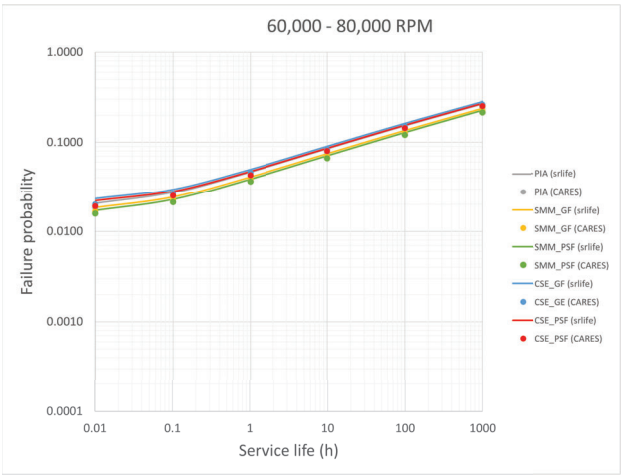

Figure 4.7: Comparison of failure probabilities for angular speeds varying from 60,000 rpm to 80,000 rpm, from CARES manual (symbols) and *srlife* (lines), generated using the models: PIA, CSE, and SMM for GF and PSF flaws

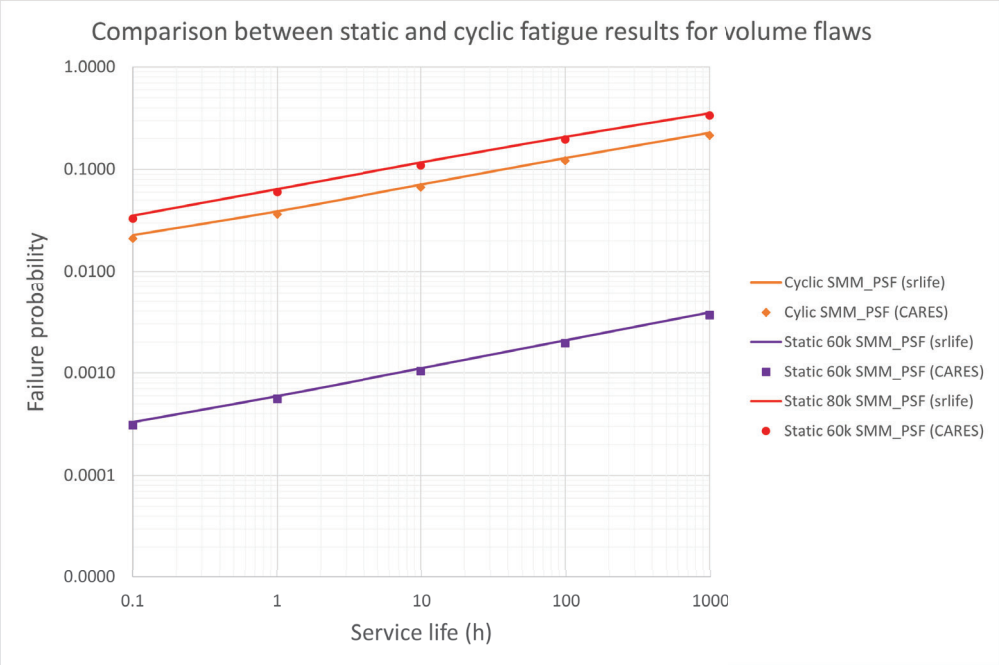

Figure 4.8: Comparison of failure probabilities generated from constant angular velocities (60,000 and 80,000 rpm) and cyclic angular velocity (60,000 - 80,000 rpm) using the model SMM for penny-shaped flaw (PSF).

4.2.2 Surface-flaws

The results for surface flaws for the following fatigue loading types are:

4.2.2.1 Static (creep) fatigue

The results for the static fatigue loading case are presented in Figure 4.9 (a) - (f) for the different angular velocities. From the comparison plots, it is observed that the failure probability increases with angular velocity and service life. The failure probability becomes equal to one close to 110k rpm and is one at 120,000 rpm, for all values of service life. This observation is also clear in the plot generated by using only one model i.e. SMM (SCC) in Fig. 4.10. Lastly, it is also observed that the values from the two sources fall close to each other. Overall the failure estimates from *srlife* are slightly more conservative than those presented in the CARES manual, as they show a higher magnitude.

4.2.2.2 Cyclic fatigue

The results for the cyclic fatigue loading case are presented in Figures 4.11, 4.12, and 4.13 for the varying angular velocity. From the comparison plots, as expected, the values of the 60k-80k rpm are higher than the values for 60k-70k, and the values increase with service life. It is also observed that the values from the two sources fall close to each other, and the cyclic fatigue results fall in between the static fatigue results.

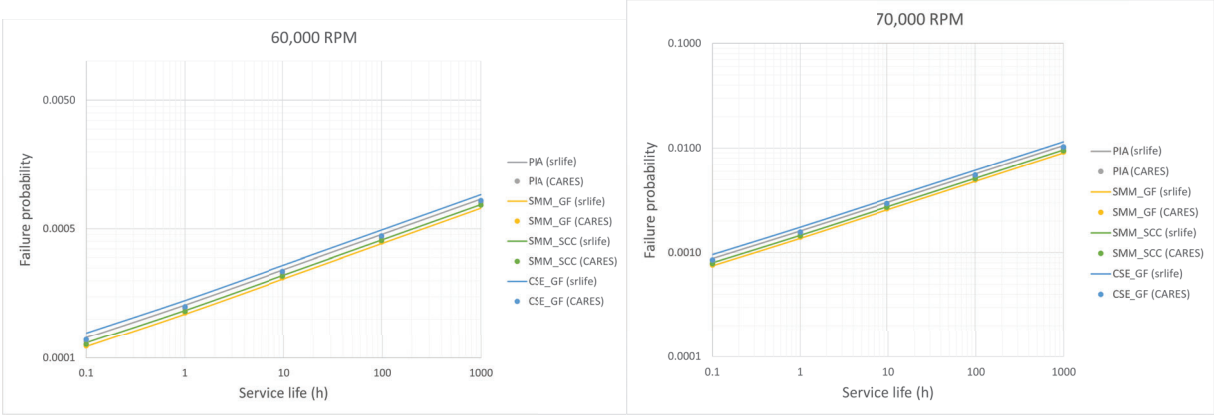

(a) (b)

Figure 4.9: Comparison of failure probabilities at (a) 60,000 rpm (b) 70,000 rpm from CARES manual (symbols) and *srlife* (lines), generated using the models: PIA, CSE, and NCSE (or SMM) for GF and SCC flaws

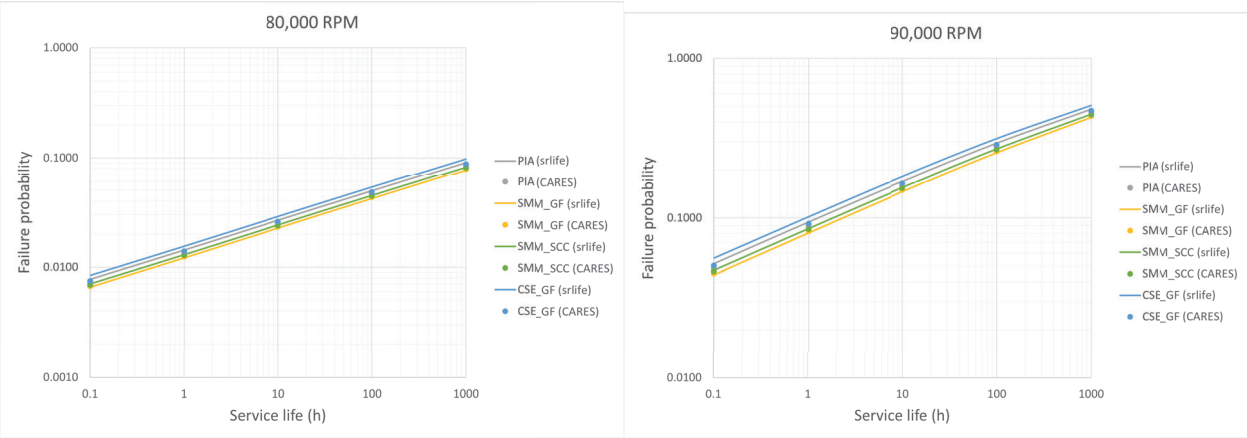

(c) (d)

Figure 4.9: Comparison of failure probabilities at (c) 80,000 rpm (d) 90,000 rpm from CARES manual (symbols) and *srlife* (lines), generated using the models: PIA, CSE, and NCSE (or SMM) for GF and SCC flaws

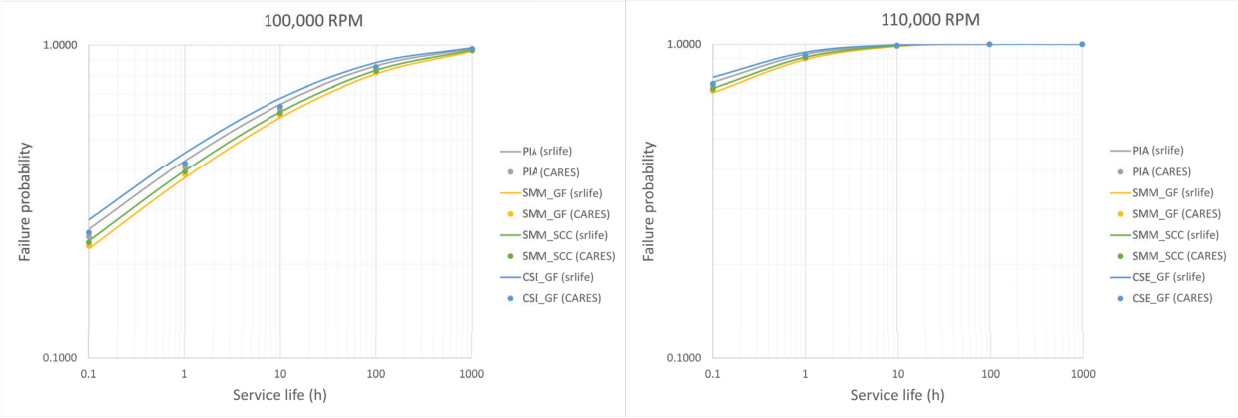

(e) (f)

Figure 4.9: Comparison of failure probabilities at (e) 100,000 rpm (f) 110,000 rpm from CARES manual (symbols) and *srlife* (lines), generated using the models: PIA, CSE, and NCSE (or SMM) for GF and SCC flaws

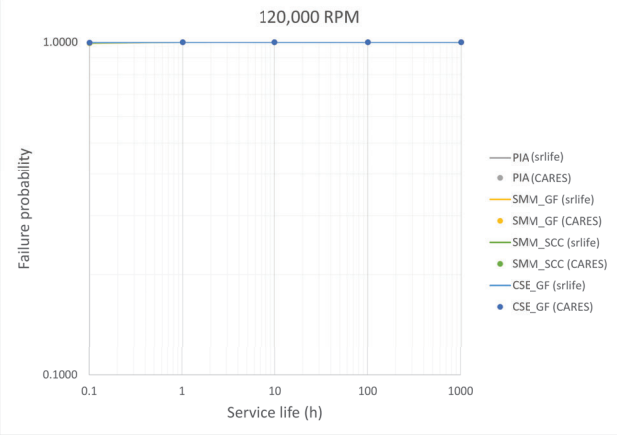

(g)

Figure 4.9: Comparison of failure probabilities at (g) 120,000 rpm from CARES manual (symbols) and *srlife* (lines), generated using the models: PIA, CSE, and NCSE (or SMM) for GF and SCC flaws

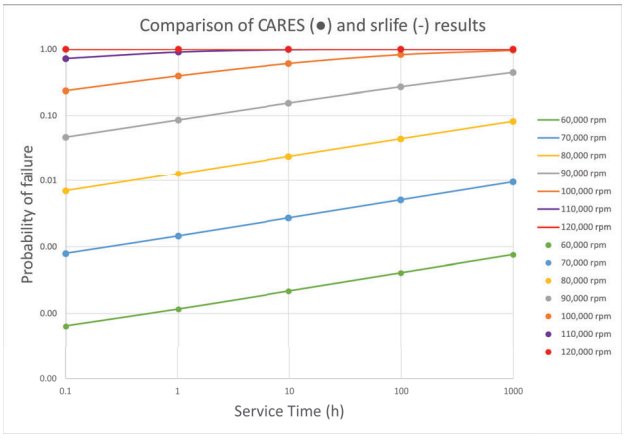

Figure 4.10: Comparison of failure probabilities for all angular velocities from CARES manual (symbols) and *srlife* (lines), generated using the model NCSE (or SMM) for semi-circular crack (SCC)

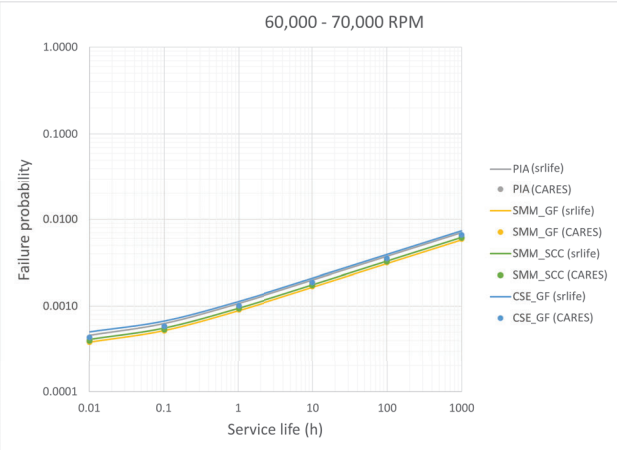

Figure 4.11: Comparison of failure probabilities for angular speeds varying from 60,000 rpm to 70,000 rpm, from CARES manual (symbols) and *srlife* (lines), generated using the models: PIA, CSE, and NCSE (or SMM) for GF and SCC flaws

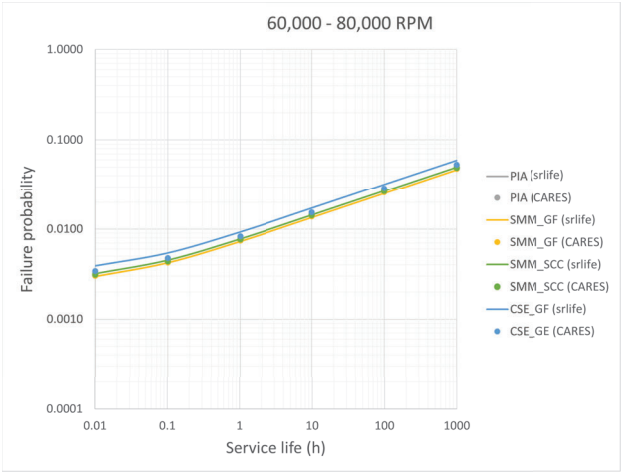

Figure 4.12: Comparison of failure probabilities for angular speeds varying from 60,000 rpm to 80,000 rpm, from CARES manual (symbols) and *srlife* (lines), generated using the models: PIA, CSE, and NCSE (or SMM) for GF and SCC flaws

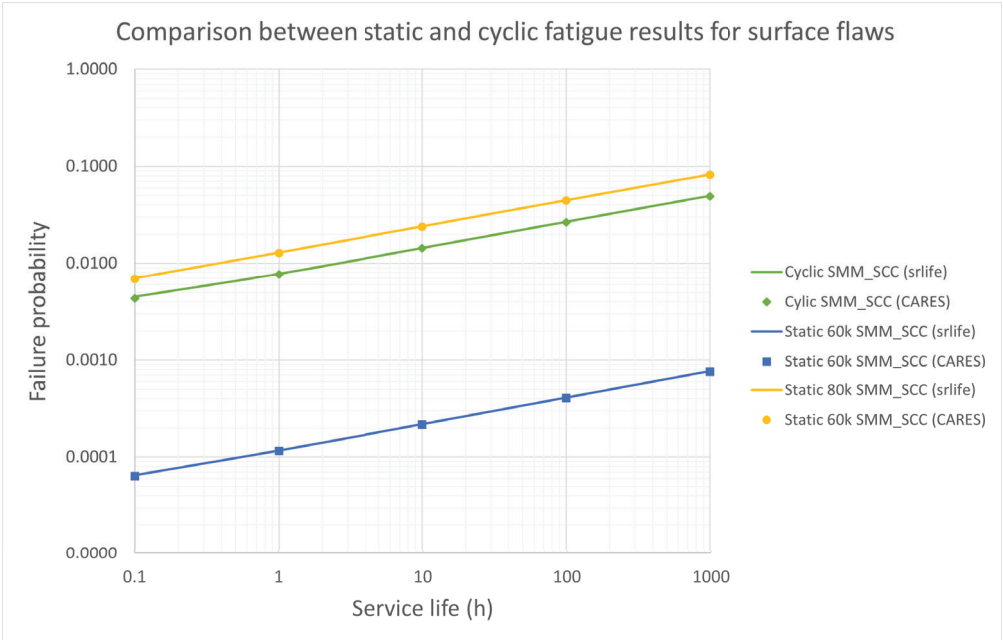

Figure 4.13: Comparison of failure probabilities generated from constant angular velocities (60,000 and 80,000 rpm) and cyclic angular velocity (60,000 - 80,000 rpm) using the model NCSE (or SMM) for semi-circular crack (SCC).

4.3 Discussion and Summary

The models presented in Chapters 2, 3 were incorporated into *srlife* to predict the time-dependent reliability of ceramic-based CSP receivers. The present chapter demonstrates the use of an example problem involving both static (creep) and cyclic fatigue in a ceramic, to validate the incorporation of the models in *srlife*. The static and cyclic fatigue results from *srlife* fall close to those presented in the CARES manual for all the models, and hence, verify the correct implementation of the models in *srlife*. On comparing the volume flaw results with the surface flaw ones, it is observed that the $P_{fV} > P_{fS}$ overall, and $P_{fV} = P_{fS}$ at 120k rpm. On comparing the failure probability values between the different models the following observations are made.

4.3.1 Volume flaws

In the case of volume flaws, the order of conservativeness from the model results is the same for *srlife* and CARES. The most conservative model is highlighted in red i.e. the CSE (GF) model.

srlife: SMM (PSF) < SMM (GF) < PIA < CSE (PSF) < CSE (GF)
CARES: SMM (PSF) < SMM (GF) < PIA < CSE (PSF) < CSE (GF)

The above order is obtained from the Batdorf models for a shear-sensitive case. An interesting observation is that the order changes when the Batdorf models are implemented as shear-insensitive and it is as shown below.

PIA < CSE (GF) < CSE (PSF) < SMM (GF) < SMM (PSF)

The difference is the Shetty mixed-mode model for penny-shaped flaw is the least conservative for the shear-sensitive case, and most conservative for the shear-insensitive case. The difference arises because of a change in the $\overline{k}_{BV}$ parameter as mentioned in Section 2.3.

4.3.2 Shear-Sensitvity Analysis (Cont.)

To comprehensively analyze the effects of shear sensitivity on the failure probability and, hence, the order of conservativeness, the failure probability was re-evaluated for the cyclic disk problem (60,000 - 80,000 rpm and 1000 h) but for a random stress tensor. During the evaluation, both shear-insensitive (SIS) and shear-insensitive (SS) cases for all the failure models (mentioned in Chapter 2) were considered. In actuality, only the MTS and SMM model results were switched from being shear-insensitive to shear-sensitive, on evaluating their $\overline{k}_B$ parameter numerically as mentioned in Section 2.3. Additionally, an effect of the $\overline{C}$ parameter on the failure probability from all the models was also investigated. The results from these analyses are shown in Fig. 4.14.

The plot shows an arrow signifying the order of conservativeness which is as follows:

SMM (PSF) SS < SMM (GF) SS < MTS (PSF) SS < PIA < MTS (GF) SS < WNTSA < MTS (GF) SIS < MTS (PSF) SIS < SMM (GF) SIS < SMM (PSF) SIS

This order holds true for the smallest value of $\overline{C} = 0.8$ as shown in Fig. 4.15 (a). On increasing the value the order changes and it is shown graphically in Fig. 4.15 (b) and (c). Additionally, the results from the SMM models change their position in the plot and the order of conservativeness as the $\overline{C}$ value is increased from 0.8 to 2 to 100. Essentially the SMM models show that for an SIS case, their failure probability decreases and for an SS the failure probability increases, as the $\overline{C}$ parameter is increased. Eventually, both cases converge to a single value. This observation is consistent with what Shetty [16] observed (Section 2.3). On the other hand, the PIA, WNTSA, and MTS models are not affected by a change in $\overline{C}$ values because their expressions do not contain the parameter. However, their order of conservativeness is decided by the $\overline{k}_B$ values.

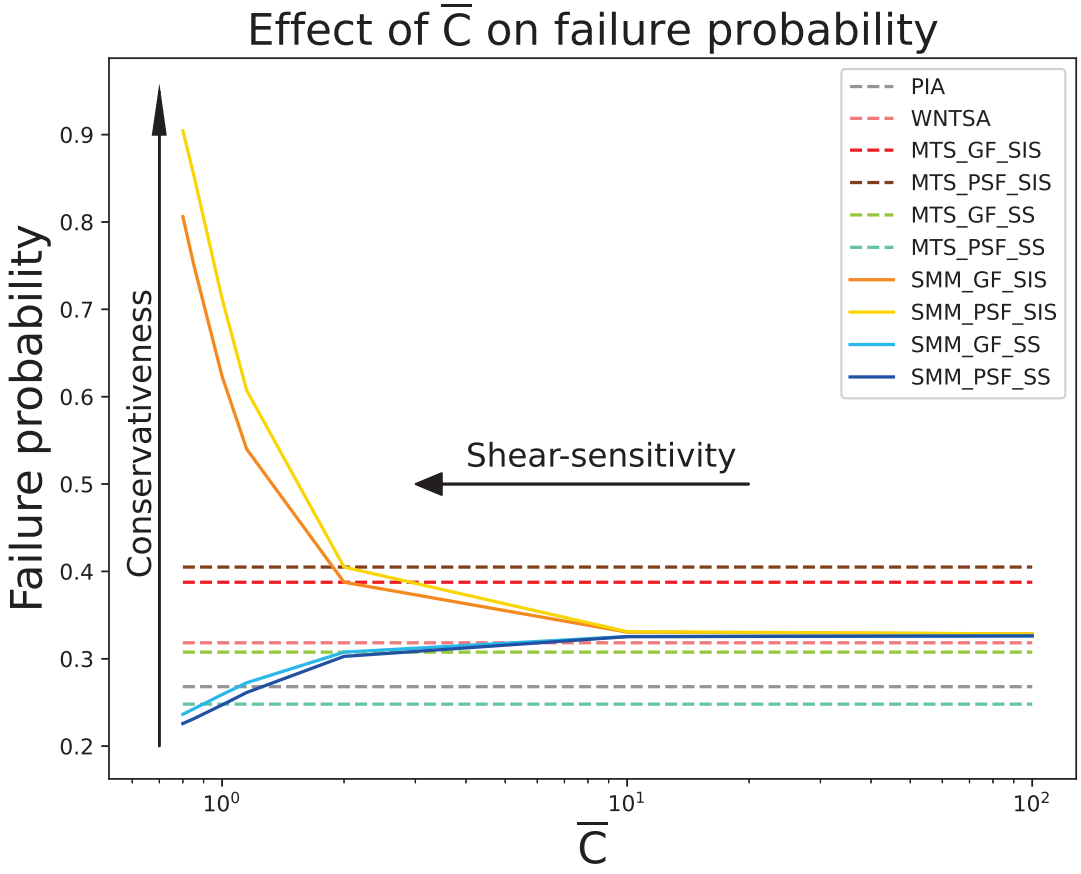

Figure 4.14: Failure probability evaluated using PIA, WNTSA, MTS, SMM models for GF and PSF and for both shear-insensitive and shear-sensitive cases, and their variation with the $\overline{C}$ parameter.

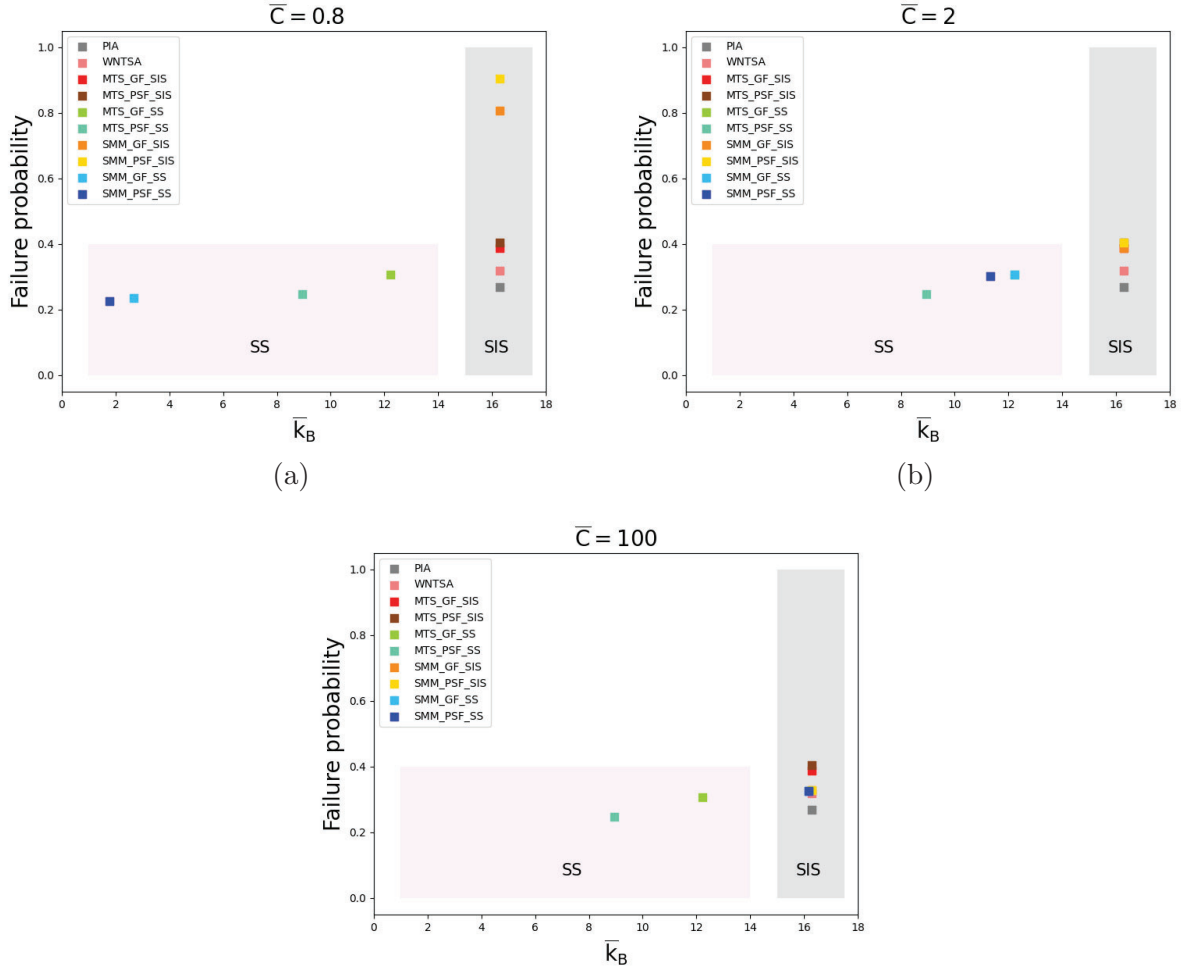

Figure 4.15: Plot of failure probability for various $\overline{k}_B$ values defining SS and SIS regions. Failure probability is evaluated with increasing $\overline{C}$ value from (a) 0.8 to (b) 2 to (c) 100.

The above analysis was also conducted by varying the (i) values of Weibull modulus (m_v) and Weibull scale (σ_{0V}) parameters, and it was observed that the order of conservativeness is not affected by a change in their values. However, on changing the stress state the order changes. On using a random stress tensor that includes compressive principal stresses, the order is as shown Fig. 4.16. It is observed that the SMM models for the SS case flip the trend they showed earlier in Fig. 4.14. Additionally, the WNTSA model is observed to be the least conservative one.

Hence, to apply and interpret the above information a user must know the Weibull parameters and $\overline{C}$ parameter for the material chosen, and the stress state. Based on the parameters and stresses, *srlife* can evaluate the failure probability (or reliability) as shown in Fig. 4.14 and 4.16, and the user gets to decide which model to choose for reliability analysis. The user is recommended to choose the most conservative model i.e. the one that predicts the highest probability of failure, but be careful of the results from the CSE model as it is agnostic to the sign of the stresses.

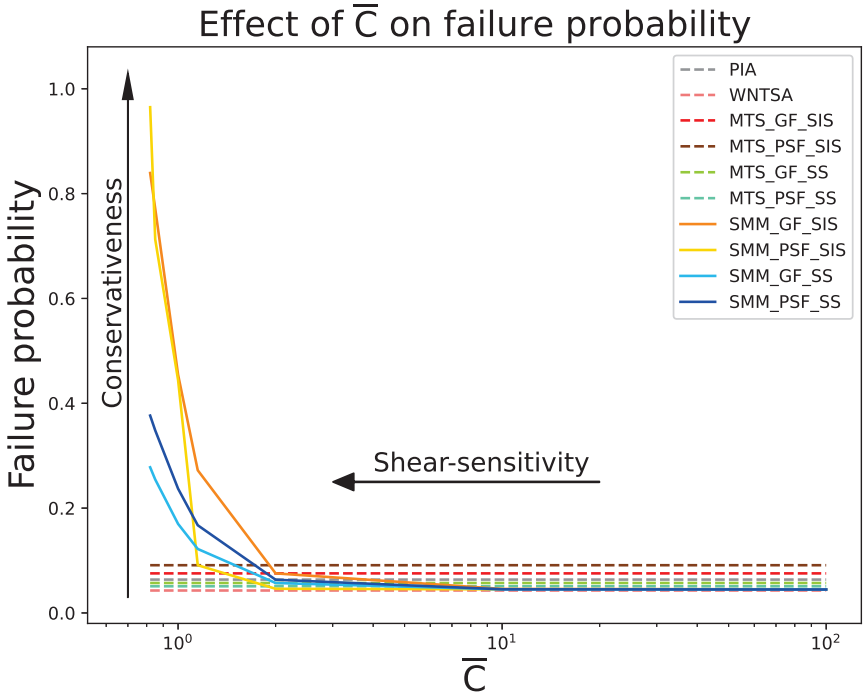

(a)

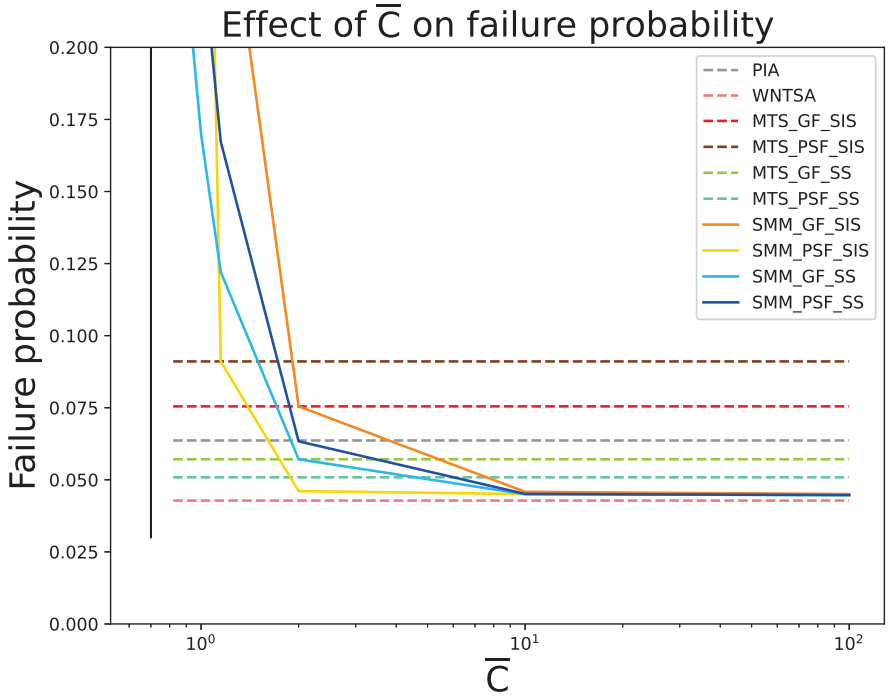

(b)

Figure 4.16: (a) Failure probability evaluated for a random stress tensor using PIA, WNTSA, MTS, SMM models for GF and PSF flaws, and for both shear-insensitive and shear-sensitive cases, and their variation with the $\overline{C}$ parameter, (b) zoomed in plot showing the order of conservativeness for all the models.

4.3.3 Surface flaws

In case of surface flaws, the order of conservativeness observed in the results from *srlife* is consistent with the one in CARES [9] for the time-dependent and shear-sensitive case. The most conservative model is highlighted in red i.e. the CSE (GF) model and it is the same as observed from volume flaw results. Due to this reason, it is expected that a shear-sensitivity analysis on the surface flaw models will provide similar results as those provided by volume flaws.

srlife: SMM (GF) < SMM (SCC) < PIA < CSE (GF)
CARES: SMM (GF) < SMM (SCC) < PIA < CSE (GF)

Part III

Experimental Investigations

5 Time-Independent and Time-Dependent Testing

As seen in Chapter 2 and 3, the models require an array of material parameters (m, σ_θ, σ_0, N, B) to evaluate the probability of failure. These parameters can be estimated by fitting the experimental data obtained from a series of time-independent and time-dependent tests conducted as per ASTM Standards [40, 41, 36, 42, 43]. In the present chapter, a description of each type of test conducted on a ceramic material is provided and the experimental data is presented. Uniaxial experimental data involving the strengths of ceramics is fitted using either a Weibull 2-parameter and 3-parameter uniaxial model as shown earlier in the equation for the crack density function i.e. Eq. 2.2. The methods for parameter estimation are also described and the final values are provided, which were implemented in srlife.

5.1 Experimental Details

5.1.1 Material Selection and Properties

The ceramic material used for testing was commercial monolithic silicon carbide (SiC) and it was purchased in plate form, from the vendor Stanford Advanced Materials [44]. SiC is commonly available and produced by various methods such as sintering and reaction-bonding. The present ceramic was produced by sintering and it contained majorly the alpha-SiC phase. Its material properties provided by the vendor are presented in Table 5.1.

	Sintered SiC
Purity of SiC	98%
Maximum working temperature	$1550°C$
Bulk Density	3.1 g/cc
Appearance porosity	2.5 %
Flexural Strength (at RT)	380 MPa
Compressive Strength	2200 MPa
Thermal Expansion	$4.0*10^{-6}$ ($<500°C$)
Thermal Conductivity	110 W/mK

Table 5.1: Material properties of commercial sintered silicon carbide from Stanford Advanced Materials.

5.1.2 Experimental Setup and Samples

To conduct the experiments, a universal testing frame and a set of SiC based fixtures as shown in Figure 5.1, were purchased from the vendor Test Resources [45], and Applied Test Systems [46], respectively. The test frame is capable of conducting tensile, flexure, and compression tests up to loads of 50kN. The test frame is equipped with a furnace that allows testing to be conducted at temperatures as high as 1200 $°C$. The test fixtures are made from Hexoloy SA (grade of SiC) that can operate up to 1900 $°C$. The test frame was set up and calibrated at ANL in November 2023. Preliminary tests were conducted and the data obtained was verified for correctness.

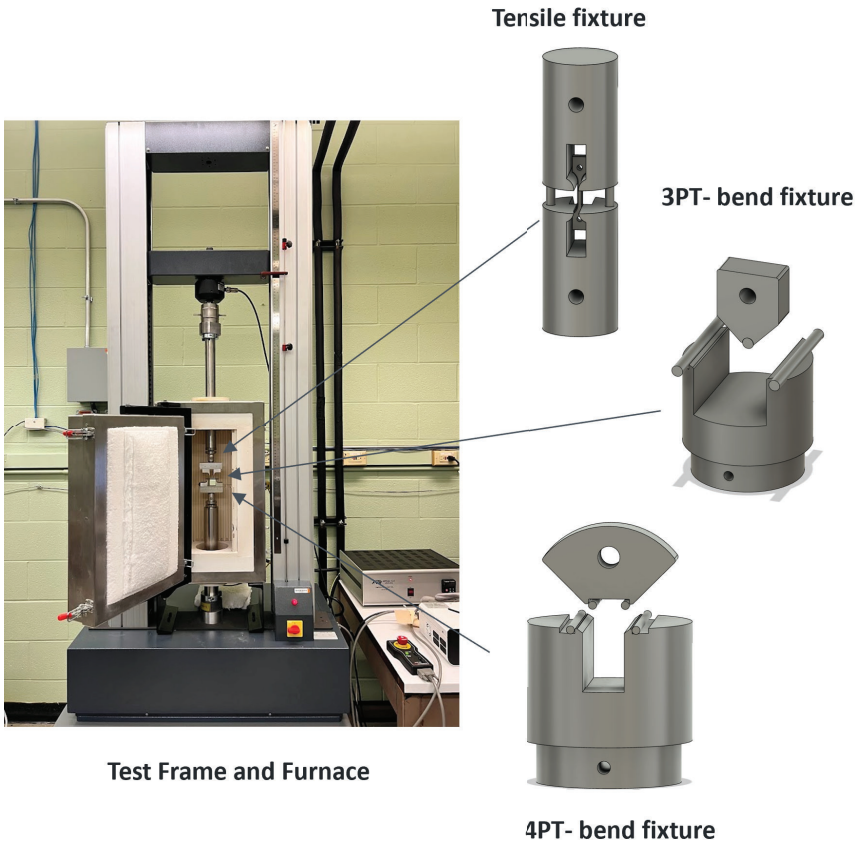

(a)

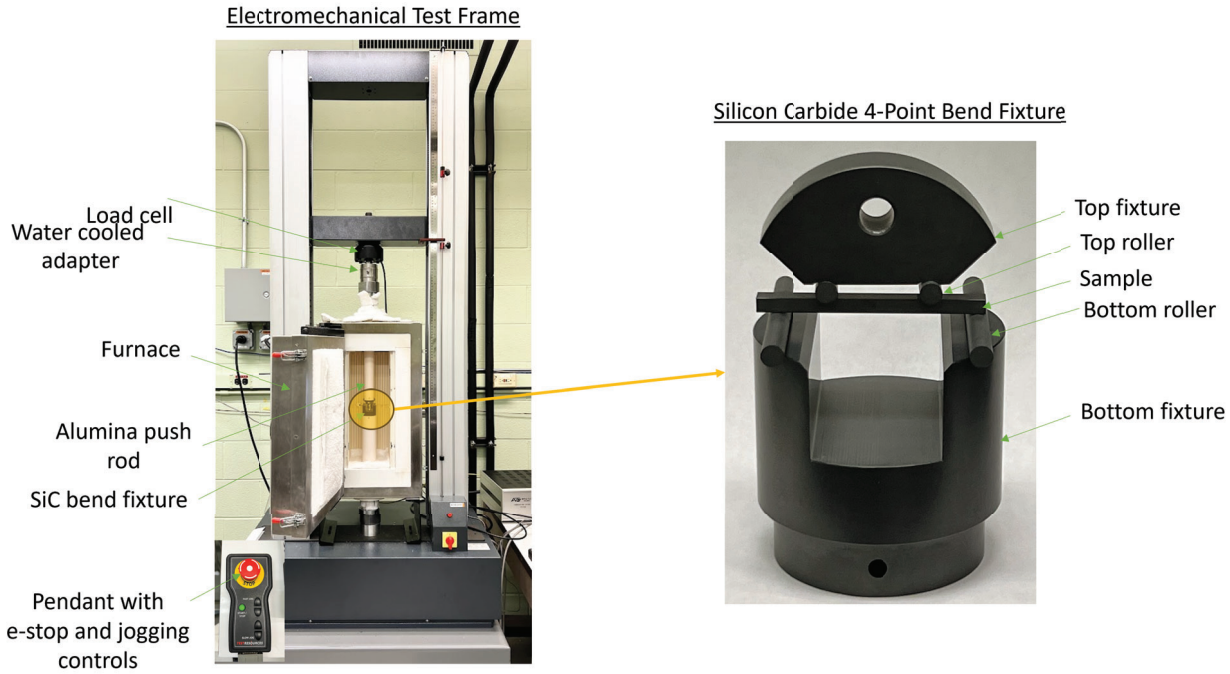

(b)

Figure 5.1: (a) Universal testing frame and silicon carbide based fixtures, (b) Test frame parts with a four-point bend fixtures at Argonne National Lab.

To conduct testing on the commercial SiC ceramic, the plates were cut into several rectangular bar-shaped samples as shown in Figure 5.2. The sample machining was done as per ASTM C1161 [40] by the machining vendor Bomas Ceramic machining specialists [47]. The sample average dimensions were 46 mm x 4 mm x 3 mm and along with the fixtures (Fig. 5.1 (b)), they met the requirement of loading Configuration B (20/40 mm) in ASTM C1161 and C1211 standard. During testing the samples were supported between the fixtures using rollers (also made of SiC) which were at a distance L_i on the top and L_o on the bottom as shown in Figure 5.3.

Figure 5.2: Commercial monolithic SiC samples bar samples.

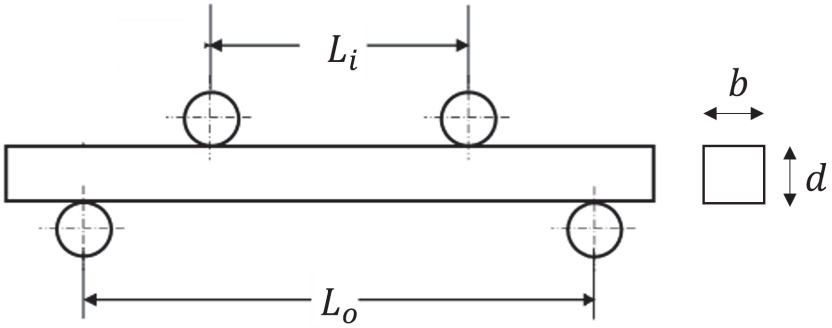

Figure 5.3: Four-point bend configuration as per ASTM Standards.

5.1.3 Experimental Tests

As mentioned earlier, the samples were used to conduct a series of time-independent and time-dependent tests. The time-independent tests included "Inert Strength or Fast-Fracture" and "Fracture Toughness" tests and it was assumed the test conditions generated no SCG. Whereas, the time-dependent tests included "Constant Stress Rate" and "Constant Stress" tests, and the loading conditions were chosen to induce SCG. The test conditions are elaborated further.

5.1.3.1 Inert Strength Tests

The inert strength or fast-fracture strength tests were conducted at room temperature and at high temperatures of 600^oC and 800^oC to determine the (flexure) strength of the material as a function of temperature. The high temperatures were chosen as they cover the operating temperatures of the CSP receiver as mentioned in the next Chapter. The tests were conducted following ASTM C1161 (for room temperature) and C1211 (for high temperature) standards [40, 41]. These tests were conducted on the bar samples using a displacement control method, by loading the sample at a rate of 0.5 mm/min (i.e. cross-head speed) up to failure (Fig. 5.4 (a)). Post failure the maximum load was recorded (Fig. 5.4(b)) and using Eq. 5.1 the flexure strength was determined:

$$\sigma_f = \frac{3}{2}\frac{F * (L_o - L_i)}{bh^2} \tag{5.1}$$

where F: maximum load, L_o: outer (support) span, L_i: inner (loading) span, b: sample width, h: sample height. The results were presented as a plot of flexure strength vs temperature.

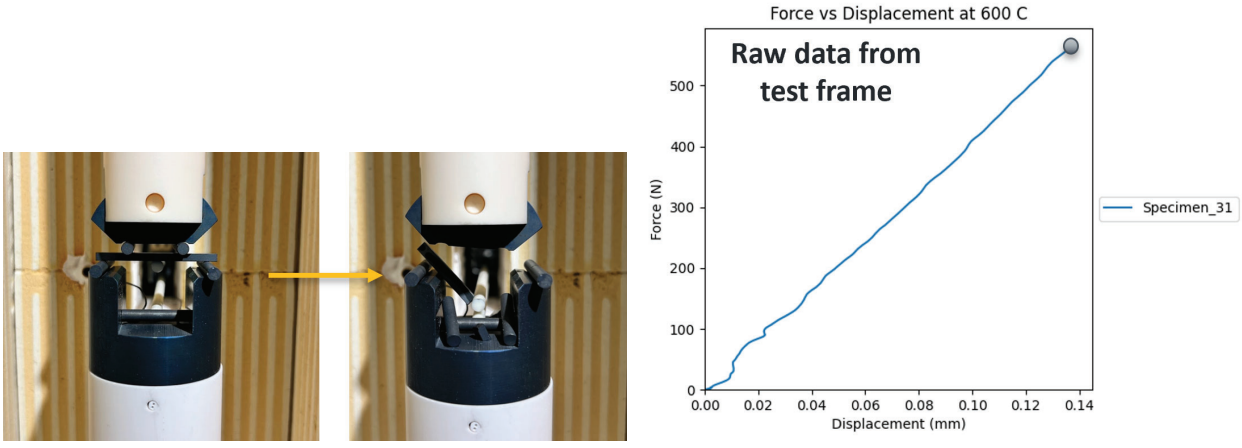

(a) (b)

Figure 5.4: (a) Picture showing sample during the test and after failure, (b) Raw data plot of force applied on sample vs. displacement shown at the midpoint.

5.1.3.2 Fracture Toughness Tests

The fracture toughness tests were also conducted at room temperature and high temperatures by following ASTM C1421 [48] and using the *pb* method mentioned in the standard. These tests were conducted on the same bar samples with straight notches cut into them at their mid-location as shown in Figure 5.5(a). The samples were loaded up to failure using the same displacement-controlled method and loading configuration as the fast-fracture tests. At failure, the maximum load was recorded (Fig. 5.5(b)) and used in Eq. 5.2 to estimate the fracture toughness.

$$K_{Ipb} = f * \left(\frac{P_{max} * (L_o - L_i) * 10^{-6}}{BW^{3/2}} \right) \left(\frac{3(a/W)^{1/2}}{2(1 - a/W)^{3/2}} \right) \tag{5.2}$$

where P_{max}: maximum load, L_o: outer (loading) span, L_i: inner (support) span, W: top-to-bottom dimension of the test specimen parallel to the crack length (depth), B: side-to-side dimension of the test specimen perpendicular to the crack length (depth), a: notch/crack length, and f is defined as:

$$f = f(a/W) = 1.9887 - 1.326(a/W) - \frac{(3.49 - 0.68(a/W) + 1.35(a/W)^2)(a/W)(1 - (a/W))}{(1 + (a/W))^2} \tag{5.3}$$

The results were presented as a plot of fracture toughness vs temperature.

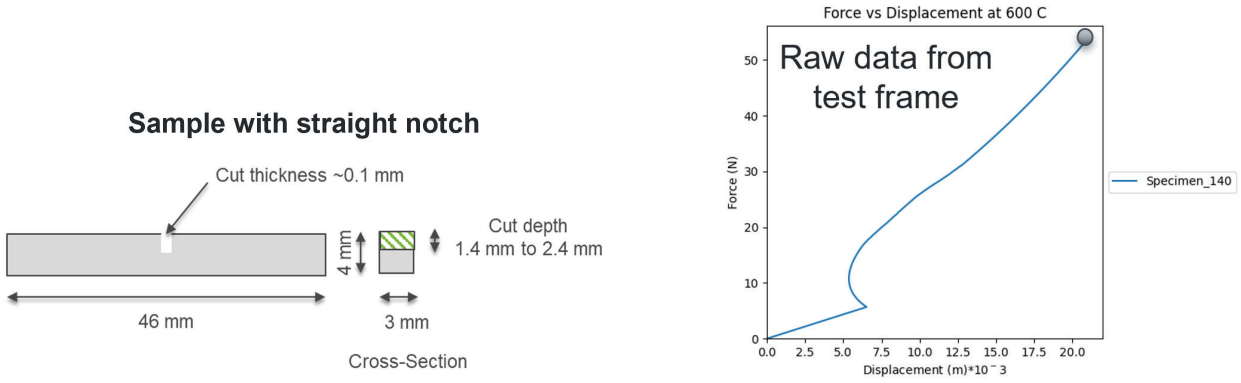

(a) (b)

Figure 5.5: (a) Raw data plot of force applied on sample vs. displacement shown at the midpoint, (b) Straight notched bar sample used for fracture toughness test.

5.1.3.3 Constant Stress Rate Tests: Dynamic Fatigue

The constant stress rate tests were a part of the time-dependent testing series wherein the test conditions were applied to induce slow crack growth before failure. The tests were conducted as per ASTM C1368 [36] at room temperature and C1456 [42] at high temperatures, using a force-control method. Different force rates (or stress rates) were used to test several samples up to failure. The applied force rates used were 0.1 N/s, 1 N/s, and 100 N/s. For each test, the corresponding maximum load before failure was recorded (Fig. 5.6), and the flexure

strength was evaluated using Eq. 5.1. The results were presented as a plot of flexure strength vs applied stress-rate, for each temperature. The relation between the flexure strength and stress rate can be defined using the following equations.

$$\sigma_f = D\dot{\sigma}^{\frac{1}{N+1}} \tag{5.4}$$

$$B = \frac{D^{N+1}}{(N+1)\sigma_i^{N-2}} \tag{5.5}$$

where N, D, B are the SCG parameters estimated from a linear regression of the experimental data, and σ_i is the inert strength, as explained in later sections.

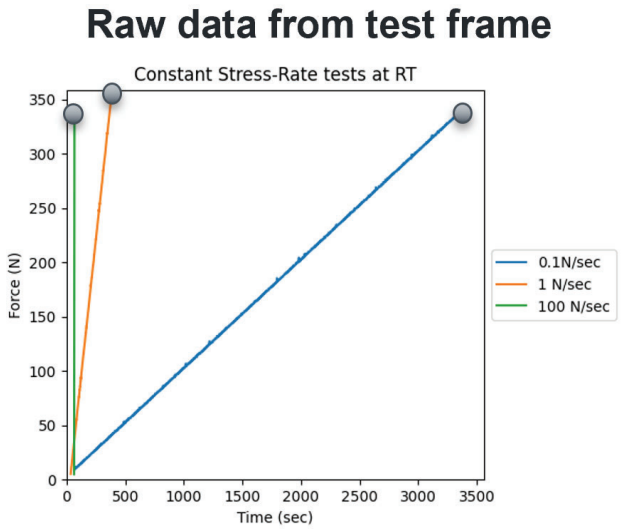

Figure 5.6: Raw data plot of force applied on sample vs. displacement shown at the midpoint for the force rates of 1, 10, and 100 N/s applied during the constant stress rate tests.

5.1.3.4 Constant Stress Tests: Static (creep) Fatigue

The constant stress tests were also a part of the time-dependent testing series wherein the test conditions were applied to induce slow crack growth before failure. The tests were conducted as per ASTM C1834 [43] at high temperatures, using a force-control method. The samples were loaded up to a fixed force value (at a fixed temperature) and the force was kept constant up till the sample failed. The force values were chosen to be close to the inert strength of the material i.e. σ_i: obtained from fast-fracture tests at the high temperatures. For each test, the displacement and time to failure were recorded (Fig. 5.7). The results were presented as a plot of applied stress (σ or σ_f) vs time to failure (t_f), for each temperature. Note: Here σ and σ_f are used interchangeably as the sample fails at the applied stress at t_f. The relation between the flexure stress and time to failure can be defined using the following equations.

$$t_f = D\sigma^{-N} \tag{5.6}$$

$$B = \frac{D}{\sigma^{N-2}} \tag{5.7}$$

where N, D, B are the SCG parameters estimated from a linear regression of the experimental data, as explained in later sections.

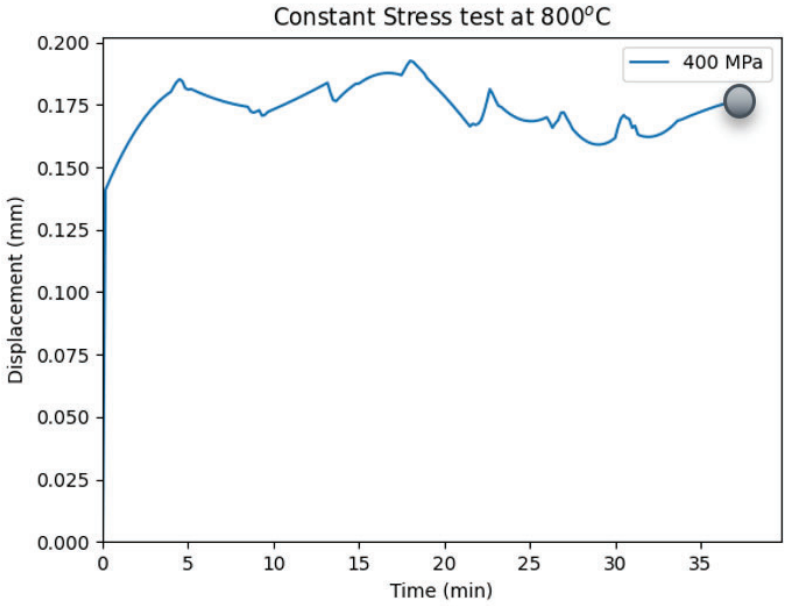

Figure 5.7: Raw data plot of midpoint displacement vs. time during the constant stress test.

The flow chart in Figure 5.8 summarizes all the tests conducted. It shows the type of test, corresponding ASTM standards followed, number of tests conducted at each condition (temperature, force rate, stress level etc.), the plot of experimental data, constitutive equations used to fit the experimental data, and finally the parameters estimated by fitting the data with the equations. The estimated parameters were then incorporated into *srlife*.

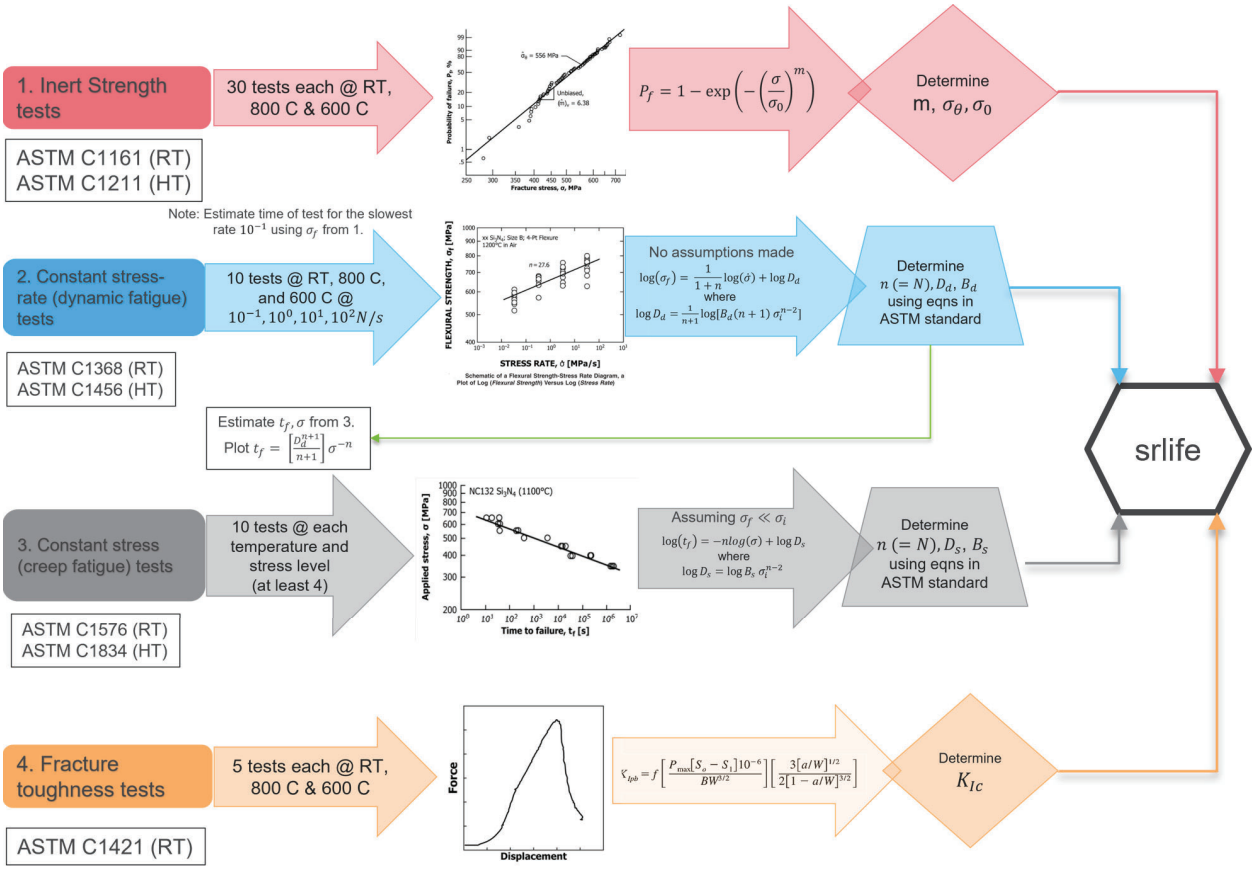

Figure 5.8: Experimental flowchart of tests to be completed and parameters to be estimated before the project ends.

5.2 Results: Experimental Data and Estimating Parameters

5.2.1 Fast-fracture Tests

A total of 30 bar samples were tested up to failure to determine their inert strengths. The strengths obtained at each temperature are shown in Fig. 5.9, through bar plots and tabulated in Table 5.2. The data is obtained from 30 tests at room-temperature, 20 tests at $600°C$, and 20 tests at $800°C$. The average flexure strength at room-temperature is 331 MPa, at 600 C is 350 MPa, and at 800 C is 329 MPa. The theoretical value of flexural strength provided by the vendor Stanford Advanced Materials [44] for this batch of SiC is 380 MPa, which falls within the bounds of data recorded in the present study. It can be observed in the bar plots in Figure 5.9 that the average strengths at the three temperatures fall within one standard deviation. A Kolmogorov-Smirnov test was implemented on the data and the statistics are tabulated in Table 5.3. The KS test reveals that the strength data belong to the same distribution.

Temperature	Number of tests ($^{\circ}C$)	Flexural strength (MPa)
RT	30	331.25 ± 58.29
$600^{o}C$	20	350.75 ± 47.48
$800^{o}C$	20	329.72 ± 62.46

Table 5.2: Flexure strength data from commercial SiC tested at room-temperature, $600^{\circ}C$, and $800^{\circ}C$.

Strengths at	statistic	p-value	p-value > 0.05	Decision
RT & $600^{o}C$	0.333	0.134	Yes	Same distribution
RT & $800^{o}C$	0.244	0.451	Yes	Same distribution
$600^{o}C$ & $800^{o}C$	0.444	0.056	Yes	Same distribution

Table 5.3: Comparison of Kolmogorov-Smirnov test statistics between data from different temperatures

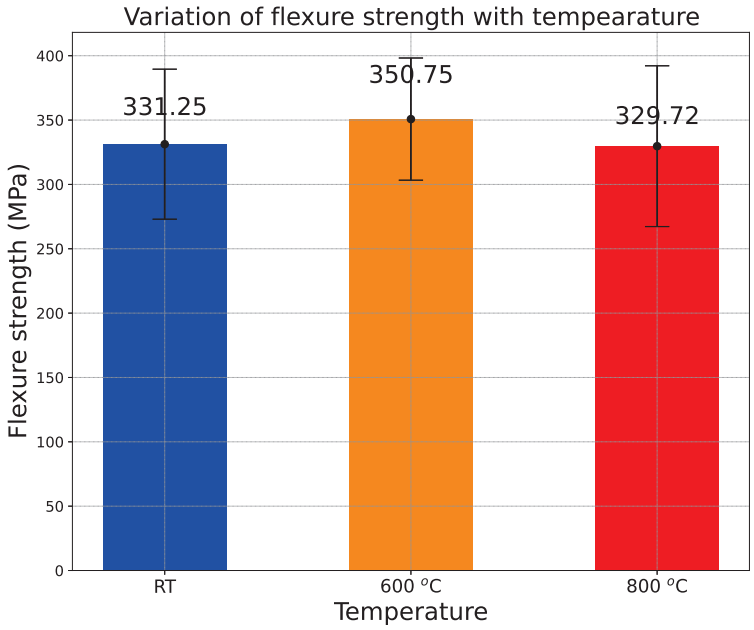

Figure 5.9: Flexure strength results from commercial SiC tested at room-temperature, $600^{\circ}C$, and $800^{\circ}C$.

5.2.2 Fractography

Post-experiments the fractured samples were collected and their fracture surfaces were viewed under a scanning electron microscope to identify the most likely initiation of fracture or fracture origin, its location i.e. volume-based or surface-based, and type. As per ASTM C1239 [49] the flaw can be located in the volume, at the surface, or at an edge. There are

several flaw types documented in the ASTM C1322 [50] that can be found at the above three locations. In the present study, the flaws observed were of the following types: A: Agglomerate, CI: Compositional Inhomogeneity, P: Pit, and M: Machining. As seen in Table 5.4, 5.5, 5.6 majority of the flaws were agglomerates (incompletely sintered particles) and compositional inhomogeneities. Also, majority of the flaws were found at the surface or very close to the surface. The rest were found inside the bulk material i.e. volume. There were three flaws that could not be categorized as a type and hence were designated as "uncertain" as per ASTM C1322. Examples of each flaw type are shown in Fig. 5.10 and 5.10.

Sample Number	Strength (MPa)	Flaw location	Flaw type
1	354.38	Surface	M
2	406.06	Volume	A
3	341.89	Surface	CI
4	277.73	Surface	A
5	386.45	Volume	A
6	332.58	Volume	A
7	225.68	Uncertain	U
8	285.06	Surface	CI
9	346.69	Surface	CI
10	307.09	Surface	CI
11	314.12	Surface	CI
12	351.73	Uncertain	U
13	380.76	Volume	A
14	288.25	Volume	A
15	349.65	Surface	M

Sample Number	Strength (MPa)	Flaw location	Flaw type
16	282.10	Volume	A
17	324.61	Volume	CI
18	320.46	Volume	A
19	265.88	Surface	A
20	236.20	Surface	CI
21	319.94	Surface	P
22	377.82	Uncertain	U
23	336.20	Surface	M
24	268.00	Surface	CI
25	273.53	Surface	A
26	407.83	Volume	A
27	484.50	Surface	CI
28	435.14	Surface	M
29	376.63	Volume	A
30	280.46	Surface	A

Table 5.4: Failure strength data from room-temperature tests and classification of flaw location and type using the following key: A: Agglomerate, CI: Compositional Inhomogeneity, M: Machining defect, P: Pit, U: Uncertain (absence of visible fracture origin).

Sample Number	Strength (MPa)	Flaw location	Flaw type
1	461.16	Surface	CI
2	339.19	Volume	A
3	359.65	Volume	A
4	364.04	Volume	A
5	320.67	Volume	CI
6	280.87	Surface	P
7	346.10	Surface	A
8	376.74	Surface	A
9	305.79	Surface	A
10	335.88	Surface	U
11	369.34	Volume	A
12	330.12	Volume	CI
13	331.38	Volume	P
14	332.45	Surface	P or CI
15	476.21	Volume	CI
16	292.50	Volume	A
17	343.74	Surface	A
18	376.00	Surface	CI
19	336.91	Surface	A
20	336.33	Surface	P & CI

Table 5.5: Failure strength data from $\underline{600\ ^{\circ}C}$ temperature tests and classification of flaw location and type using the following key: A: Agglomerate, CI: Compositional Inhomogeneity, M: Machining defect, P: Pit, U: Uncertain (absence of visible fracture origin).

Sample Number	Strength (MPa)	Flaw location	Flaw type
1	400.62	Volume	A
2	336.31	Surface	A
3	199.72	Edge	M
4	289.93	Volume	A
5	285.75	Surface	M
6	309.92	Surface	A
7	285.87	Surface	P & A
8	280.94	Surface	A
9	307.66	Volume	A
10	448.20	Surface	P
11	310.72	Volume	CI
12	359.18	Surface	CI & A
13	286.98	Surface	A
14	361.93	Surface	P
15	423.41	Surface	CI
16	382.89	Volume	CI
17	270.93	Volume	CI
18	276.80	Surface	CI
19	405.46	Volume	P
20	371.28	Volume	A

Table 5.6: Failure strength data from $\underline{800\ ^{\circ}C}$ temperature tests and classification of flaw location and type using the following key: A: Agglomerate, CI: Compositional Inhomogeneity, M: Machining defect, P: Pit, U: Uncertain (absence of visible fracture origin).

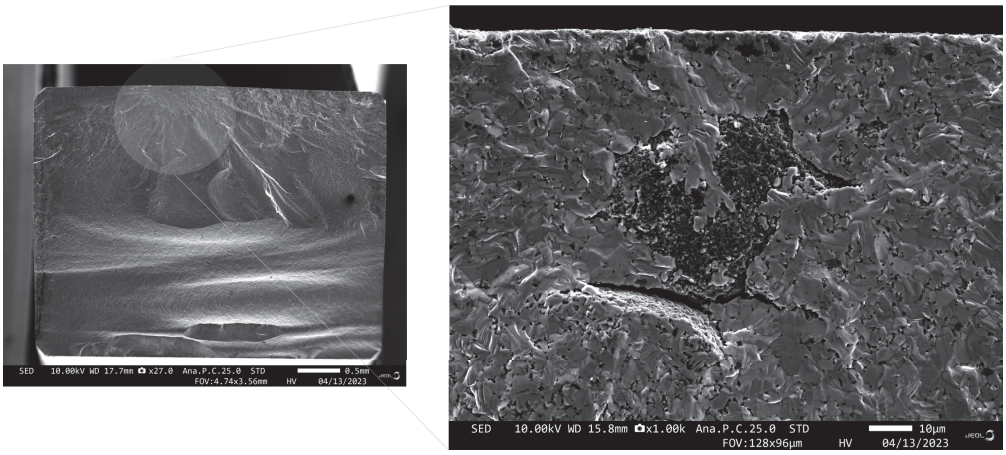

(a) Sample 1: Agglomerate within the volume

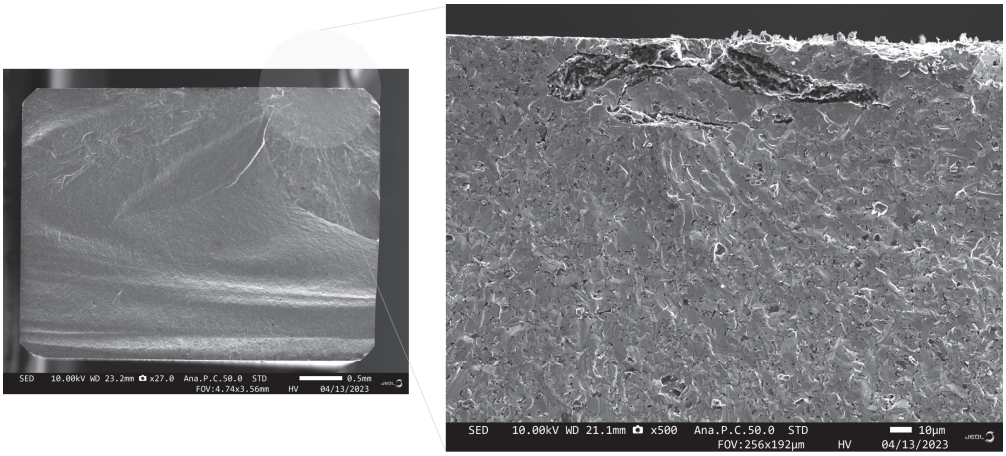

(b) Sample 3: Compositional inhomogeneity attached to the surface

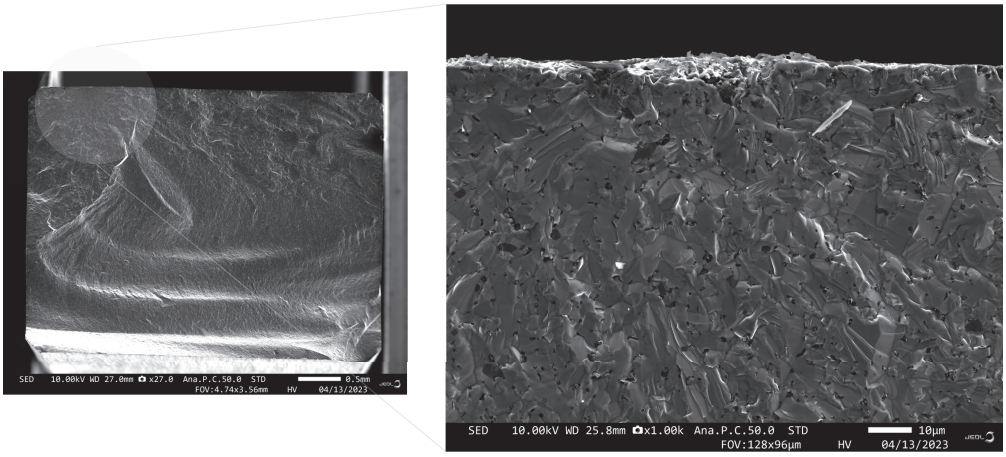

(c) Sample 15: Machining defect on surface

Figure 5.10: Fracture surfaces of samples 1, 3, and 15 investigated under SEM to identify flaw type and location.

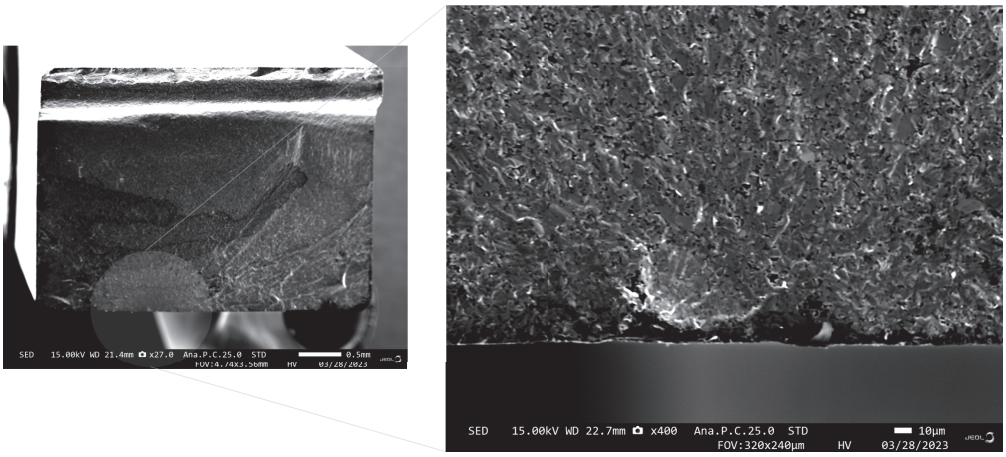

(d) Sample 21: Pore close to surface

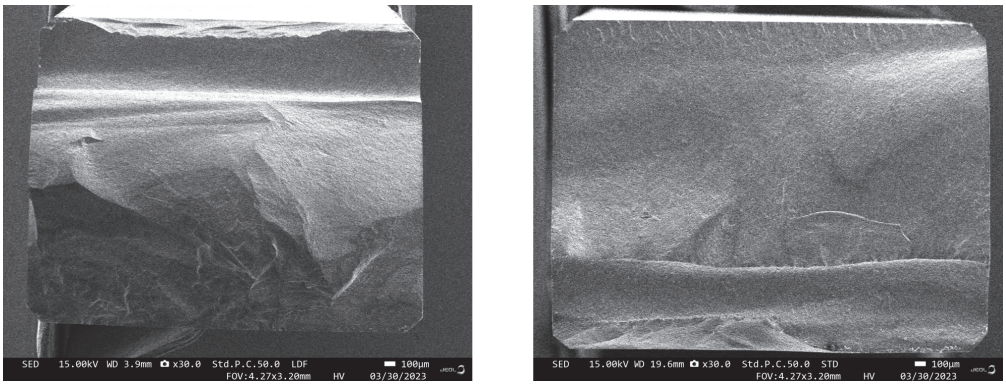

(e) Sample 7: Uncertain fracture origin

Figure 5.10: Fracture surfaces of samples 21 and 7 investigated under SEM to identify flaw type and location.

5.2.3 Weibull Parameters

The failure strengths of monolithic ceramics are stochastic in nature i.e. they exhibit a scatter in strengths due to their inherent flaw distribution. To plot the failure strengths, the rank statistics method has been conventionally used [51, 52, 53, 54]. This involves sorting the strengths in ascending order and using the expression for rank statistics [49, 55] to calculate a probability of failure (Eq. 5.8) corresponding to each strength. In Section 5.2.1 it was observed that the average failure strength does not change with temperature and the KS test revealed the strengths at different temperatures fall within the same distribution. Therefore, the strengths for all temperatures were pooled together, for the volume and surface flaws and plotted as shown in Figure 5.8.

$$P_f = \frac{i - 0.5}{N} \; or \; \frac{i - 0.3}{N + 0.4} \tag{5.8}$$

The Weibull statistical fracture theory has been widely used till today, to fit the failure strengths of ceramics since its introduction in 1939 [14, 56, 57, 58], as it can predict the experimental strengths and capture the specimen size effect reliably. However, there are

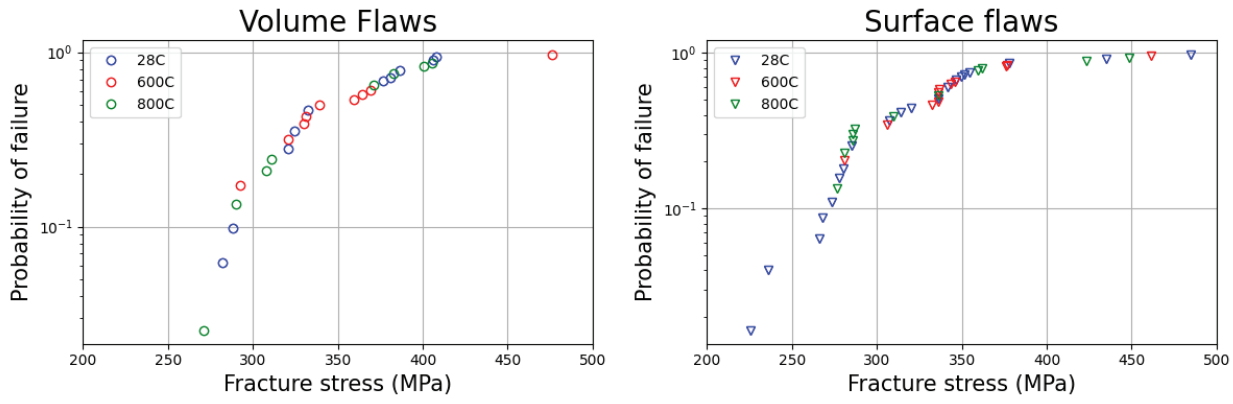

(a) (b)

Figure 5.11: Rank statistics of failure strengths generated from (a) volume flaws and (b) surface flaws

studies [59, 53, 60] that show that a Weibull distribution may not capture the statistics accurately in cases involving multi-modal flaw distribution, R-curves behavior, etc. For the present work, a Weibull distribution was chosen and modified appropriately to capture the statistics while fitting the parameters. Additionally, as demonstrated in Chapters 2 and 3, a Weibull distribution can utilize uniaxial failure statistics to capture arbitrary states of stress by leveraging the analytical equations from the fracture mechanics based models, and this justifies its use in the present Chapter. To use a Weibull distribution, firstly the failure strengths of ceramics for each population of flaw type (as shown in Fig. 5.11) are treated as a continuous random variable (as per ASTM C1239 [49]). The random variable is then implemented in the Weibull equation and the parameters are obtained by a fitting method. As mentioned in Chapter 2 the parameters are separately obtained for each flaw type and their method of estimation will be described in this section.

To demonstrate the above, the data in Fig. 5.11 were fitted to two separate Weibull distributions based on the flaw type by using a *python* script. The script implemented Eq. 5.9 and Eq. 5.10 to estimate the Weibull model parameters for failure strength distribution due to volume flaws and surface flaws, respectively.

$$P_{fV} = 1 - exp\left[-\left(\frac{\sigma}{\sigma_{0V}}\right)^{m_V} \frac{bdL_i}{2(1+m_V)}\left[\int_{d\sigma_{uV}/2\sigma}^{d/2} \frac{1}{y}\left(\frac{2y}{d} - \frac{\sigma_{uV}}{\sigma}\right)^{1+m_V} dy + \frac{L_o}{L_i}\left(1 - \frac{\sigma_{uV}}{\sigma}\right)^{1+m_V}\right]\right] \tag{5.9}$$

$$P_{fS} = 1 - exp\left[-\left(\frac{\sigma}{\sigma_{0S}}\right)^{m_S} \frac{dL_o}{2(1+m_S)}\left[\int_{d\sigma_{uS}/2\sigma}^{d/2} \frac{1}{y}\left(\frac{2y}{d} - \frac{\sigma_{uS}}{\sigma}\right)^{1+m_S} dy + \frac{1}{L_o d}(L_i d + L_o b + (1+m_s)L_i b)\left(1 - \frac{\sigma_{uS}}{\sigma}\right)^{1+m_S}\right]\right] \tag{5.10}$$

where L_i, L_o, b, and d are sample dimensions as defined in Fig. 5.3, σ the failure stress, σ_0 the scale parameter, σ_u the threshold stress, m the Weibull modulus, P_f the probability of failure, and subscripts V and S represent volume and surface, respectively.

Eq. 5.9 and Eq. 5.10 come from [55]. These equations directly correlate the probability of failure to the non-uniform stress distribution in a four-point bend test specimen, so the estimated Weibull model parameters represent the variation in the material's uniaxial failure strength. Fig. 5.12 shows the model fit to experimental data and Table 5.7 lists the fitted model parameters.

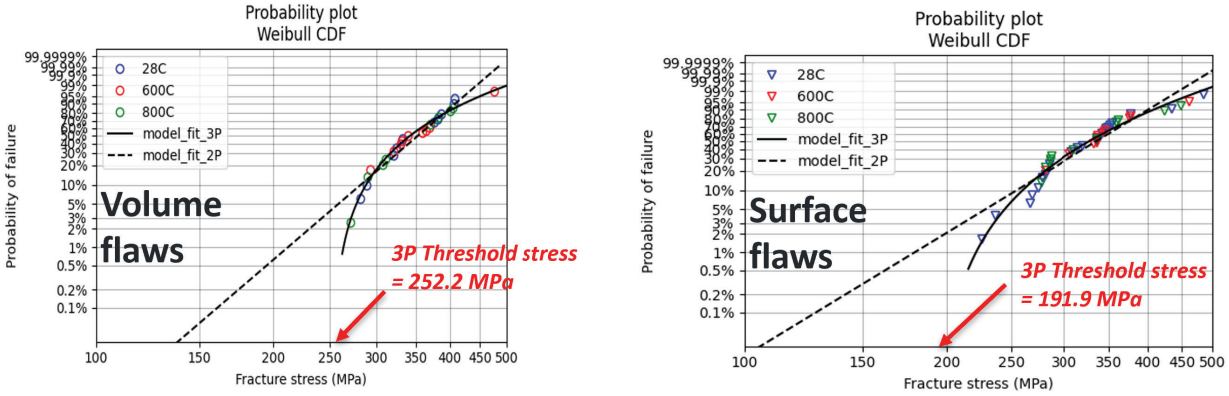

Figure 5.12: Weibull 2-parameter and 3-parameter model fits to experimental data.

Note we fit the four-point bend test data to Weibull 2-parameter and Weibull 3-parameter models. Although the Weibull 2-parameter model is frequently used to describe the variability in ceramic strength, it often results in overly conservative design estimates, especially for larger components [61], as it calculates a nonzero probability of failure across the entire stress range. In contrast, the Weibull 3-parameter model introduces a threshold stress parameter, σ_u, which allows for a zero probability of failure when the applied stress is at or below this threshold. Moreover, as discussed below, the Weibull 3-parameter model provides a better fit to our experimental data compared to the Weibull 2-parameter model. Similar findings have also been reported by other researchers [61, 57, 58]. The probability of failure of a component is defined by Eq. 5.11 and Eq. 5.11 using the Weibull 2-parameter and Weibull 3-parameter model, respectively.

$$
\begin{aligned}
P_{fV,2P} &= 1 - exp\left[-\int_V \left(\frac{\sigma}{\sigma_{0V,2P}}\right)^{m_{V,2P}} dV\right] \\
P_{fS,2P} &= 1 - exp\left[-\int_A \left(\frac{\sigma}{\sigma_{0S,2P}}\right)^{m_{S,2P}} dA\right]
\end{aligned}
\tag{5.11}
$$

$$
\begin{aligned}
P_{fV,3P} &= \begin{cases} 0 & if\ \sigma_{uV} \leq 0 \\ 1 - exp\left[-\int_V \left(\frac{\sigma - \sigma_{uV}}{\sigma_{0V,3P}}\right)^{m_{V,3P}} dV\right] & if\ \sigma_{uV} > 0 \end{cases} \\
P_{fS,3P} &= \begin{cases} 0 & if\ \sigma_{uS} \leq 0 \\ 1 - exp\left[-\int_A \left(\frac{\sigma - \sigma_{uS}}{\sigma_{0S,3P}}\right)^{m_{S,3P}} dA\right] & if\ \sigma_{uS} > 0 \end{cases}
\end{aligned}
\tag{5.12}
$$

Flaw type	Model	Weibull modulus (m)	Scale parameter (σ_0)	Threshold stress (σ_u)
Volume flaws	2P	8.29	515.3 MPa-(m)$^{3/m}$	0
	3P	1.11	1690.2 MPa-(m)$^{3/m}$	252.2 MPa
Surface flaws	2P	6.75	711.8 MPa-(m)$^{2/m}$	0
	3P	2.02	1291.6 MPa-(m)$^{2/m}$	191.9 MPa

Table 5.7: Weibull parameters obtained on fitting the strength data for volume and surface based flaws separately, using a 2-parameter and 3-parameter model.

As Eq. 5.12 indicates the probability of failure for a volume element in a finite element model of a component is zero if the σ is less than the volume threshold stress, σ_{uV}. Similarly, the probability of failure for a surface element is zero if the σ is less than the surface threshold stress, σ_{uS}. Here, σ represents either the effective equivalent stress (or principal stress for the PIA model, or normal stress for the WNTSA model), or the transformed effective equivalent stress when estimating time-independent or time-dependent reliability, respectively."

The fitting in Fig. 5.12 shows that the Weibull 3-parameter model captures the failure strengths better compared to the Weibull 2-parameter model, especially the low strength ($<$ 300 MPa) values. Additionally, the 2-parameter model provides non-zero failure probability even at low stresses as the model line when extended to low stresses intercepts the y-axis at low failure probabilities. Whereas in case of the 3-parameter model, the failure probability below the threshold stress is set to zero. This implies the Weibull 2-parameter model is more conservative than the 3-parameter model. The Weibull modulus values in the Table 5.7 indicate that the scatter in the data from volume flaws is lower compared to the data from surface flaws. From the scale parameter, it is observed that the stress at which volume flaws fail is higher compared to that of the surface flaws. Lastly, the threshold parameter for surface flaws is lower compared to the volume flaws.

5.2.4 Fracture Toughness Tests

A total of 15 bar samples with a straight notch in them were tested up to failure to determine the material's fracture toughness. The strengths obtained at each temperature are shown in Fig. 5.13 through bar plots and tabulated in Table 5.8. The data is obtained from 5 tests conducted at room temperature, 600°C, and 800°C. The average flexure strength at room temperature is 3.58 $MPa\sqrt{m}$, at 600 C is 3.09 $MPa\sqrt{m}$, and at 800 C is 3.41 $MPa\sqrt{m}$. The value of fracture toughness was not provided by the vendor Stanford Advanced Materials [44] and hence, it was compared with the values found in Kaur et. al. [62] for SiC. The literature values of fracture toughness from transgranular fracture of SiC is 3.4 $MPa\sqrt{m}$ and it falls within the bounds of data recorded in the present study as shown in the bar plot. On inspecting the fracture surfaces of the samples after failure, evidence of transgranular fracture such as cleavage steps (marks left after fracture across the grain) was found as seen in Figure 5.14. Additionally, as seen in Figure 5.13 the average value of fracture toughness at the three temperatures falls within one standard deviation.

Temperature	Number of tests ($°C$)	Fracture Toughness ($MPa\sqrt{m}$)
RT	5	3.58 ± 0.52
600^oC	5	3.09 ± 0.71
800^oC	5	3.41 ± 0.35

Table 5.8: Fracture toughness data from commercial SiC tested at room-temperature, $600°C$, and $800°C$, compared with literature data from Shetty .

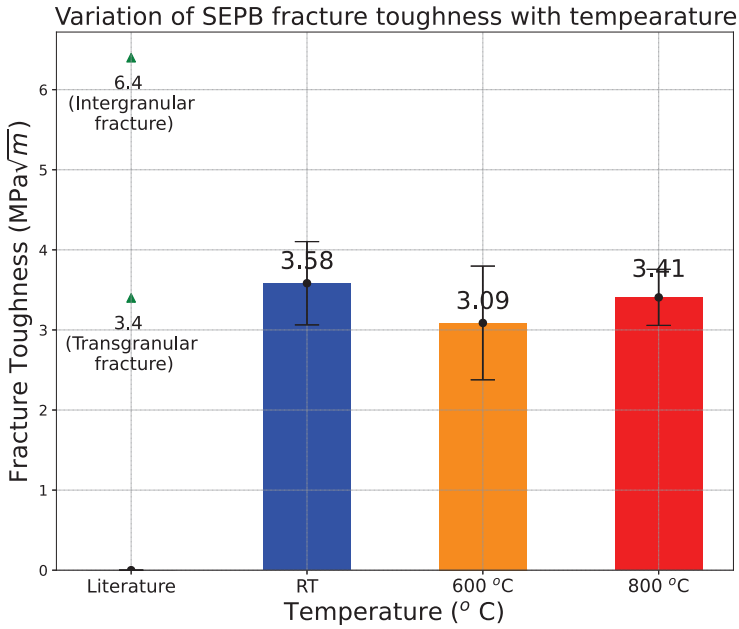

Figure 5.13: Fracture toughness results from commercial SiC tested at room-temperature, $600°C$, and $800°C$.

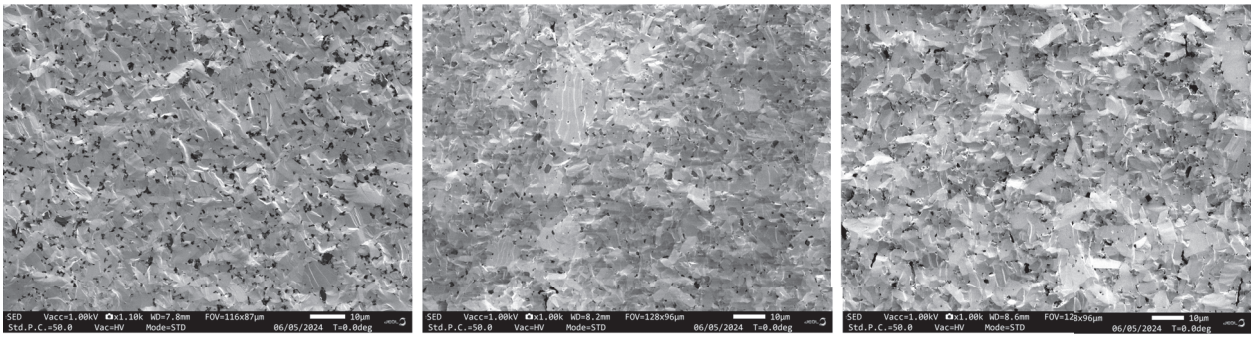

Figure 5.14: Fracture surfaces of samples tested at (a) room-tempearture, (b) $600°C$, and (c) 800 $°C$ investigated under SEM to identify fracture type.

5.2.5 Constant Stress Rate Tests

Constant stress rate tests were conducted to determine the SCG parameters. These parameters are required for time-dependent reliability estimation of the component. A total of 95 bar samples were tested up to failure at different force-rates (or stress-rates) and temperatures. The average strength values are tabulated in Table 5.9. The individual strengths from the tests are plotted with respect to their corresponding applied stress rates at each temperature as shown in Fig. 5.15. The data points from the fast-fracture tests were also included in the table as they were used in the parameter estimation technique described further. The average force rate for the fast-fracture tests was calculated to be 25 N/s and based on the specimen dimensions the average stress-rate was calculated to be 20.89 MPa/s. No fractography was conducted on the fractured sample from constant stress rate tests. We assumed the same rate for SCG for both the volume and surface flaws.

We determined the SCG parameters, $NandD$ by fitting 5.4 to the constant stress rate test data. The SCG paramter, B was then estimated using 5.7. For the value of σ_i in 5.7, the average strength of the material was used. Fig. 5.16 shows the experimental data along with the model fit following 5.4. For this fitting, we segregated the experimental data into room temperature and high temperature data. The high temperature data consists of test data collected at $600°C$and $800°C$. Since there is a very little variation in the constant stress rate tests conducted at $600°C$and $800°C$, these data were combined. Fig. 5.16(a) shows the model fit to room temperature test data conducted at four constant stress rates. The estimated values of $NandB$ are 63.65 and 10.23, respectively. The high temperature test data shown in Fig. 5.16(b) (also in Fig. 5.15(b, c)) indicate reduction in fracture stress with decreasing stress rate from 100 MPa/s to 1 MPa/s. This is expected because, according to the SCG phenomena, the fracture stress is supposed to decrease with decreasing stress rate. However, the fracture stress increases when stress rate is further decreased to 0.1 MPa/s. One possible reason for this unexpected behaviour could be closing of the surface crack due to oxidation. So, there are two competing phenomena - (i) closing of surface crack due to oxidation and (ii) SCG - that are affecting the performance of the material. To separate these two phenomena or find which one of these two controls the long term performance of the material, experiments on specimens with oxidation-resistant coating or longer term experiments, such as constant stress tests at a rate slower than 0.1 MPa/s and constant stress tests, may be required. Due to the increase in fracture stress at 0.1 MPa/s, the SCG model fit to the combined data at all four stress rates at high temperatures does not yield useful model parameters as the model finds no SCG happening. We therefore removed the 0.1 MPa/s data, i.e. ignoring the effect of oxidation which is reasonable as the receiver tubes will be coated with material that will increase solar radiation absorption and also resist oxidation, when fitting the SCG model to the high tempearture constant stress rate test data. The estimated model parameters are 63.65 and 2.84 for N and B, respectively. Note the value of N was forced to be constant for both room temperature and high temperature, so that only B is interpolated between room temperature and $600°C$when analyzing receiver tubes.

We determined the SCG parameters, N and D, by fitting Eq. 5.4 to the constant stress rate test data. The SCG parameter, B, was then estimated using Eq. 5.7. For the value of σ_i in Eq. 5.7, the average strength of the material was used. Fig. 5.16 shows the experimental

data along with the model fit based on Eq. 5.4. In this fitting, we segregated the experimental data into room temperature and high temperature data. The high temperature data consist of tests conducted at 600°C and 800°C. Since there was very little variation in the constant stress rate tests conducted at 600°C and 800°C, the data were combined.

Fig. 5.16(a) shows the model fit to the room temperature test data conducted at four constant stress rates. The estimated values of N and B are 63.65 and 10.23, respectively. The high temperature test data, shown in Fig. 5.16(b) (also in Fig. 5.15(b, c)), indicate a reduction in fracture stress with decreasing stress rate from 100 MPa/s to 1 MPa/s. This is expected since, according to SCG phenomena, fracture stress decreases with decreasing stress rate. However, the fracture stress increases when the stress rate is further reduced to 0.1 MPa/s. One possible reason for this unexpected behavior could be the closing of surface cracks due to oxidation. Therefore, two competing phenomena—(i) the closing of surface cracks due to oxidation and (ii) SCG—are influencing the material's performance at high temperature.

To distinguish these phenomena and determine which one controls the long-term performance, experiments on specimens with oxidation-resistant coatings or longer-term experiments, such as constant stress tests at rates slower than 0.1 MPa/s, may be necessary. Due to the increase in fracture stress at 0.1 MPa/s, the SCG model fit to the combined high temperature data at all four stress rates did not yield useful parameters, as the model suggests no SCG is occurring. Therefore, we excluded the 0.1 MPa/s data—ignoring the oxidation effect, which is reasonable since the receiver tubes will be coated with materials that enhance solar radiation absorption and may also resist oxidation—when fitting the SCG model to the high temperature constant stress rate data. Moreover, ASTM C1456 allows exclusion of slower stress rate data if there is an increase in strength. The estimated model parameters for N and B are 63.65 and 2.84, respectively. Note that N was forced to remain constant for both room and high temperatures, so only B is interpolated between room temperature and 600°C when analyzing receiver tubes.

Temperature ($°C$)	Number of tests	Force rate (N/s)	Stress rate (MPa/s)	Flexural strength (MPa)
RT	12	0.1	0.085 ± 0.005	303.59 ± 47.32
	10	1	0.841 ± 0.012	347.41 ± 53.04
	30	25	20.89	331.25 ± 58.29
	10	100	84.52 ± 1.05	364.31 ± 53.91
600	10	0.1	0.087 ± 0.003	342.41 ± 53.41
	10	1	0.856 ± 0.038	331.85 ± 76.38
	30	25	20.89	354.05 ± 49.63
	11	100	84.96 ± 4.95	348.54 ± 64.38
800	10	0.1	0.085 ± 0.001	370.22 ± 57.28
	10	1	0.841 ± 0.023	302.91 ± 74.73
	30	25	20.89	323.21 ± 62.26
	10	100	84.54 ± 3.61	343.43 ± 46.67

Table 5.9: Average failure strength data from the constant stress rate tests conducted at 0.1, 1, and 100 N/s, at room temperature, 600$°C$, and 800$°C$.

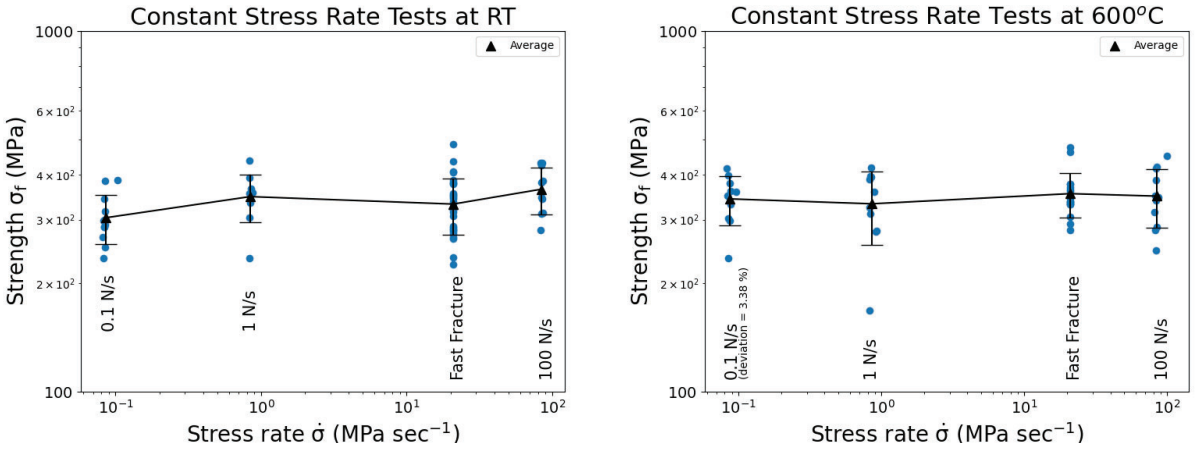

(a)

(b)

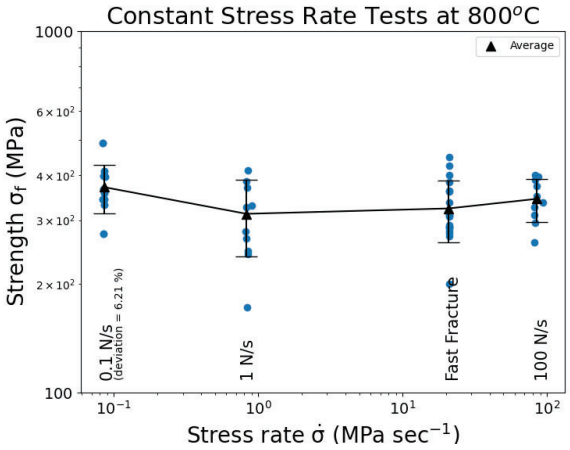

(c)

Figure 5.15: Constant stress-rate results from commercial SiC tested at (a) room temperature, (b) 600°C, and (c) 800°C. Blue dots indicate data points and the solid black line indicates the average line.

Temperature ($°C$)	N	D ($MPa.sec$)	B ($MPa^2.hr$)
RT	63.65	317.57	10.23
600 $°C$	63.65	317.54	2.85
800 $°C$	63.65	317.54	2.85

Table 5.10: Subcritical crack growth parameters obtained on fitting the strength data from constant stress rate tests.

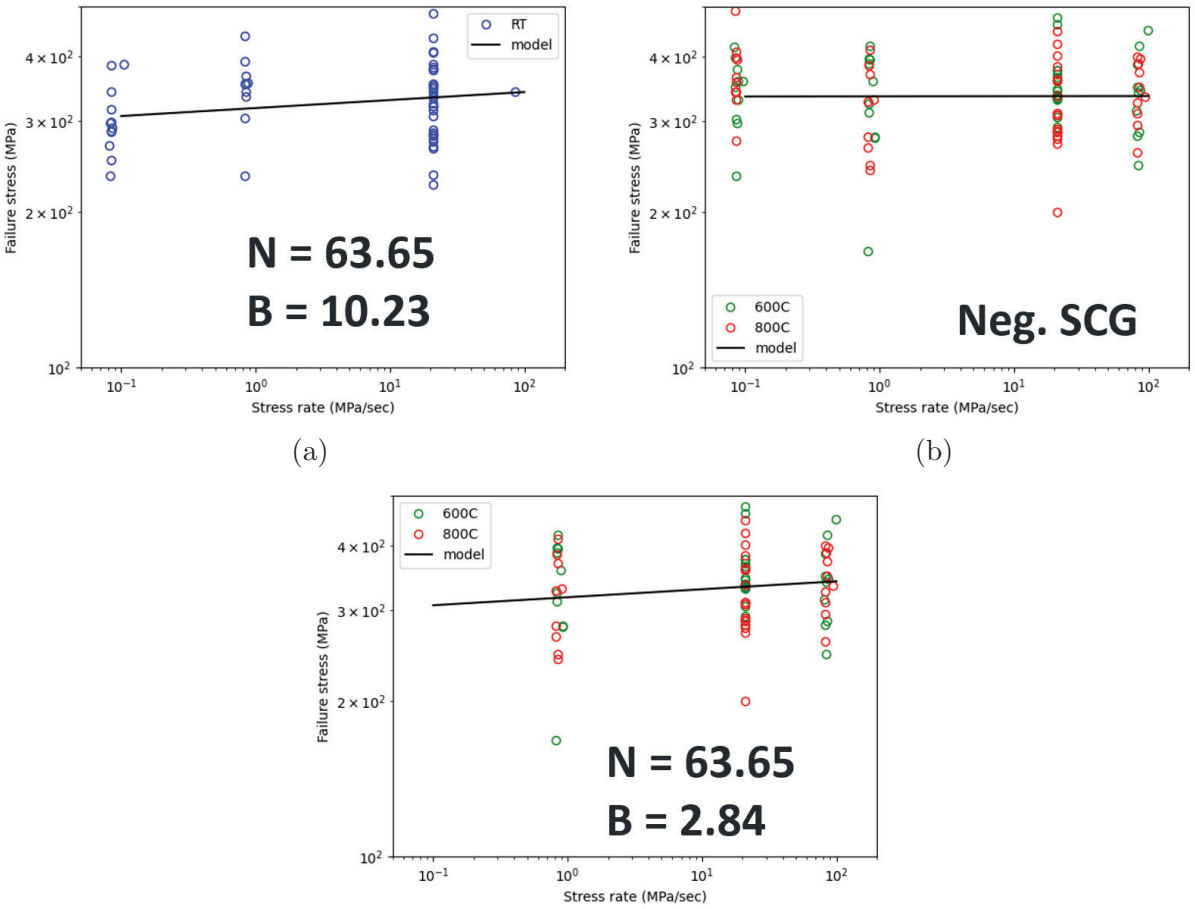

(a) (b)

(c)

Figure 5.16: Subcritical crack growth parameters obtained by applying regression on data points at (a) room temperature, (b) 600$°C$ and 800$°C$ pooled together, (c) 600$°C$ and 800$°C$ pooled together excluding 0.1 N/s data.

5.2.6 Constant Stress Tests

A total of 15 bar samples, were tested at 800 $°C$ to estimate their time to failure under a static (creep) loading condition. In 14 out of the 15 tests, the samples failed during loading

and 5 of the samples did not fail even after a long test duration. Only one test was successful as the sample failed after 37 mins when loaded at 400 MPa, as shown in Table 5.11.

Temperature ($°C$)	Number of tests	Applied force (N)	Applied Stress (MPa)	Test Result	Reason
$800°C$	15	471	400.35	Unsuccessful	Sampled did not fail after 26 h
		479	400.72	Unsuccessful	Sampled did not fail after 24 h
		524	450.41	Unsuccessful	Sampled did not fail after 37 h
		486	400.11	Successful	Sample failed after 37 min
		404	400.61	Unsuccessful	Failed while loading at 351 MPa
		465	400.49	Unsuccessful	Failed while loading at 359 MPa
		423	350.07	Unsuccessful	Failed while loading at 259 Mpa
		359	300.17	Unsuccessful	Failed while loading at 233 MPa
		489	400.90	Unsuccessful	Failed while loading at 398 MPa
		450	375.21	Unsuccessful	Failed while loading at 312 MPa
		429	350.46	Unsuccessful	Failed while loading at 331 MPa
		394	330.35	Unsuccessful	Failed while heating at 333 MPa
		368	300.24	Unsuccessful	Failed while loading at 217 MPa
		329	275.54	Unsuccessful	Sample did not fail after 110 h
		365	300.24	Unsuccessful	Sample did not fail after 215 h

Table 5.11: Results from constant-stress (creep) tests conducted at $800°C$.

5.3 Discussion and Summary

In the present chapter, a series of time-independent and time-dependent tests were conducted on samples of monolithic commercial SiC. The tests were conducted at various temperatures and the data was plotted for each temperature to check for a trend. The data was also used to estimate a set of Weibull failure and subcritical crack growth parameters for the ceramic, using statistical methods. Observations were made from the trends shown and are discussed as follows:

- The ceramic revealed no degradation in strength with temperatures, up to $800°C$. This conclusion was based on the average strength falling within one standard deviation for all temperatures and the KS test concluding the strength data belong to the same distribution.
- On identifying the sources of failure origin, surface-based flaws were found to contribute majorly to failure, and these included agglomerates, compositional inhomogeneities, and machining defects. The remaining flaws were either located in the volume, or at the edge, and some were unidentified. The agglomerates and compositional inhomogeneities might have existed due to incomplete sintering of the ceramic. The machining defects must have been generated from polishing or grinding the samples. On loading the sample, the above defects form areas of stress concentrations and act as critical flaws responsible for the failure, and the stress distribution across the sample's surface and volume controls which critical flaw results in failure.
- Based on the Weibull scale and threshold parameter it can be concluded that failure from volume flaws likely occurs at higher stresses in comparison to failure from surface flaws, in the ceramic. At high temperatures ($600°C$, $800°C$) surface defects or cracks

get blunted (or become less severe) by the formation of a protective layer of silica via oxidation of SiC, which can result in failure only from the volume flaws at higher stresses. The fractography of samples tested at high temperatures did indeed reveal a layer of oxidation formed on the surface.

- Based on Fig. 5.16(b), it can be concluded that the SiC shows negligible SCG up to $800°C$. This can be witnessed from the constant stress tests wherein 5 out of 14 samples did not fail upon subjecting the ceramic to constant loads at $800°C$.

Part IV

Metallic/Ceramic receiver comparison

6 Evaluating Reliability of a Ceramic Receiver

Fig. 6.1 illustrates the overall process of evaluating a ceramic solar receiver using the *srlife* tool. The evaluation begins with the user inputting key geometric and operational parameters. These include the tube dimensions such as height, outer diameter, and wall thickness, as well as the number of tubes in each panel and the arrangement of panels in each flow path. Additionally, the user provides the mass flow rates of the heat transfer fluid (HTF) for each flow path, along with the net incident heat flux and internal pressure as functions of time for each tube considered in the analysis. Moreover, *srlife* provides options for setting up tube mechanical boundary conditions to approximate the effects of tube restraint caused by the panel manifold and/or interpanel structural connections. For individual tubes these options range from completely decoupled, generalized plane strain to having each tube in a panel rigidly connected. Similarly, the mechanical constraints between panels in the receiver can range from disconnected to rigidly connected. To optimize computational efficiency, the user may analyze a representative subset of tubes from each panel rather than evaluating all tubes.

srlife incorporates a basic thermohydraulic analysis module to calculate the heat balance within each flow path of the receiver. Note the thermohydraulic module is a new addition to *srlife* as part of this project. In the original version of the tool, the user was required to provide the fluid temperature as a function of position along the flow path and time. Integration of the thermohydraulic analysis into *srlife* greatly simplifies the analysis required to make a fair comparison between comparable receivers made from widely different material categories. Details of the development of thermohydraulic module and its validation can be found in the year-1 progress report of this project [63].

The mass flow rate of the HTF can either be set as constant—resulting in variable fluid outlet temperatures—or adjusted over time to maintain a uniform fluid outlet temperature throughout the day. For the latter, *srlife* can be utilized to iteratively determine the mass flow rates required at different times using its thermohydraulic solver.

Once the thermohydraulic analysis is complete, *srlife* uses its structural analysis modules to calculate the stress and strain distributions in each tube, based on the internal pressure and temperature profiles. At this point, the software has generated detailed stress, strain, and temperature data for every tube in the receiver.

The final step involves converting these results into either creep-fatigue damage accumulation for metallic tubes or reliability predictions for ceramic tubes. For metallic receivers, life is determined by the worst-case creep-fatigue damage accumulation. Details of the creep-fatigue life estimation for metallic receivers in *srlife* can be found in [11]. In contrast, life estimation for ceramic receivers follows a probabilistic approach due to the inherent variability in material failure, making deterministic predictions impractical. *srlife* calculates the reliability of ceramic tubes as a function of service life, enabling users to estimate tube life for a specified target reliability.

srlife utilizes the equations provided in Chapters 2 and 3 to calculate the reliability of each tube, based on the stress field and temperature-dependent material properties. First, an effective equivalent stress is calculated from the 3D stress tensor for each element in the finite element model of individual tubes. The effective equivalent stress maps the multiaxial stress components to unaxial stress. The formulation of the effective equivalent stress depends on the model, crack shape, and fracture criteria considered. The effective equivalent stress is

then used, along with the Weibull model parameters (which are temperature-dependent for each element), to determine the probability of failure for that element.

The probability of failure for each element in the finite element model of the tube is then combined to determine the overall probability of failure for the entire tube, which is subsequently converted into the tube's reliability. This calculation is performed for failures due to both volume flaws and surface flaws. The tube's reliability is based on the combined probability of failure from both types of flaws. This process allows for a time-independent reliability assessment of individual tubes in the receiver.

The time-dependent reliability assessment follows the same process, with one additional step - here, the effective equivalent stress is transformed into a modified equivalent stress before calculating the probability of failure for each element. This modification depends on the service life of the receiver.

The reliability of individual tubes in a panel can then be combined to estimate the reliability of the panel. Finally, the reliability of the panels can be combined to estimate the overall reliability of the receiver.

For reliability estimation, *srlife* provides many options to the user for choosing the failure model, crack type, and fracture criteria. As discussed in Chapter 2, the ceramic failure models implemented in *srlife* are based on different failure criteria including – (i)PIA method, (2) WNTSA method, (3) MTS criterion, (4) CSE criterion, and (5) SMM criterion. The PIA and WNSTA models are inherently crack shape independent and shear insensitive, while other models are crack shape dependent. *srlife* provides options for modelling two types of cracks – GF and PSF – for volume flaw reliability analysis and another two types – GN and SCC – for surface flaw analysis. For the four crack shape dependent models, *srlife* provides two analysis options – one using shear insensitive fracture criteria and one using shear sensitive fracture criteria. Table 6.1 lists all the models implemented in srlife and specifies their relevance for various types of analysis options.

For reliability estimation, *srlife* offers a variety of options for selecting failure models, crack types, and fracture criteria. As discussed in Chapters 2 and 3, the ceramic failure models implemented in *srlife* are based on several failure criteria, including: (1) the PIA method, (2) the WNTSA method, (3) the MTS criterion, (4) the CSE criterion, and (5) the SMM criterion. The PIA and WNTSA models are crack-shape independent and insensitive to shear, while the other models depend on crack shape. *srlife* allows users to model two types of cracks—GF and PSF—for volume flaw reliability analysis, and GN and SCC for surface flaw analysis. For the four crack-shape-dependent models, *srlife* provides two analysis options: one using shear-insensitive fracture criteria and the other using shear-sensitive criteria. Table 6.1 outlines all the models available in *srlife* and their applicability for various analysis types.

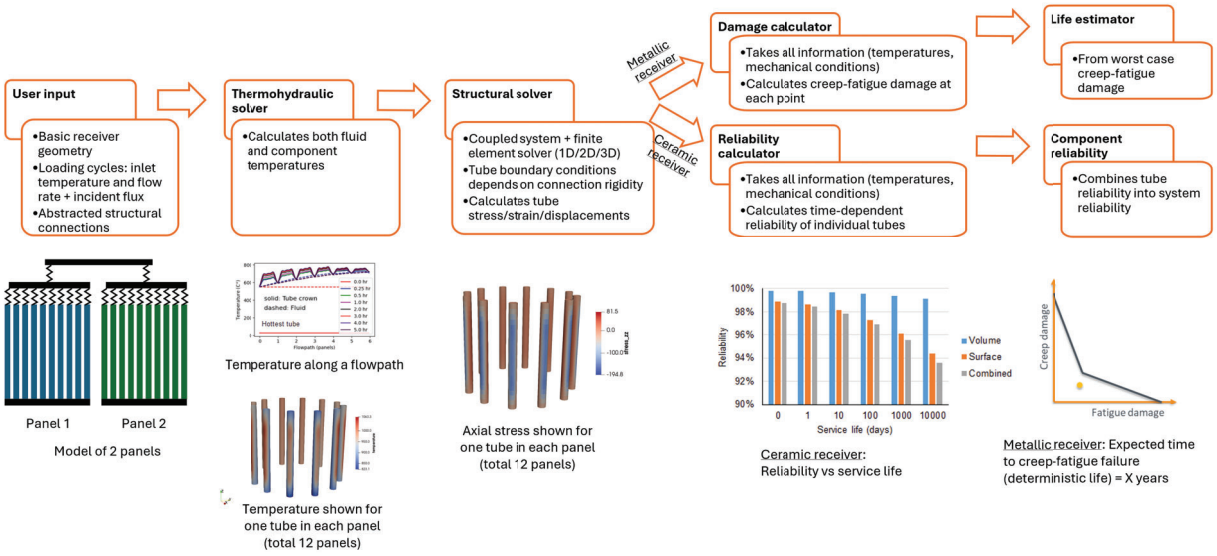

Figure 6.1: Flowchart showing analysis steps in receiver evaluation in *srlife*.

Model		Crack type	Shear insensitive fracture criteria		Shear sensitive fracture criteria	
			Volume flaw	Surface flaw	Volume flaw	Surface flaw
Crack shape independent	PIA	-	yes	yes	no	no
	WNTSA	-	yes	yes	no	no
Crack shape dependent	MTS	GF	yes	yes	yes	yes
		PSF	yes	no	yes	no
	SMM	GF	yes	yes	yes	yes
		PSF	yes	no	yes	no
		GN	no	yes	no	yes
		SCC	no	yes	no	yes
	CSE	GF	yes	yes	yes	yes
		PSF	yes	no	yes	no
		GN	no	yes	no	yes

Table 6.1: Reliability models and receiver analysis options in *srlife*.

7 Metallic vs Ceramic Receiver Designs

7.1 Reference receiver systems

One of the primary project objectives is to perform a comparative analysis between ceramic and metallic receiver designs. We compare the performance of ceramic and metallic materials through system optimization for the maximum achievable life of the receiver. For this design study, we consider a cylindrical receiver located at Dagget, CA, with a thermal design power of 180 MWt. The system optimization is performed in two steps – (i) determining an optimum receiver overall size and heliostat configuration for a given maximum allowable heat flux, (ii) based on the heat flux map on the receiver, optimizing the tube size and the panel configuration in the system. For the allowable heat flux, we consider three cases – (i) 1000 kW/m^2, (ii) 700 kW/m^2, (iii) 450kW/m^2. With three levels of allowable heat flux, we basically optimize the tube size and panel configuration for three receiver systems with the same design power. It's worth noting that while one material may be more expensive than another, it might perform better under high heat flux conditions, resulting in a more compact design with fewer tubes. Therefore, adjusting the allowable heat flux allows for a cost comparison of receiver designs optimized for each material.

We utilized SolarPILOT to determine the optimum heliostat configuration and receiver overall dimensions. Table 7.1 lists the values of key parameters considered in this optimization. Annual simulations were conducted based on 9 representative days, with time points recorded every hour. For the heliostat selection criteria, we considered maximizing the annual thermal input to the receiver. Table 7.2 lists the optimal receiver dimensions for different allowable heat fluxes. For an allowable heat flux of 1000 kW/m^2a, the optimal receiver diameter was found to be 10 m for a height of 12 m. These optimal receiver dimensions are similar to those reported in [64] for an cylindrical receiver with similar thermal design power, tower height, and heliostat parameters. We then fixed the receiver height to 12 m and determined the receiver diameter for the other two allowable heat fluxes – 700 kW/m^2a and 450 kW/m^2a. The height of the receiver was kept fixed so that the length of the tubes is the same for all the cases. The aspect ratio of the receiver with 450 kW/m^2a allowable flux is similar to the optimal design reported in [65] for a receiver with similar allowable heat flux. Fig. 7.1 shows the heliostat field and heat flux maps at different times of the day of summer solstice for three receivers.

The next step in design optimization involves determining the optimal tube size and the optimal panel and flowpath configuration in the receiver to maximize the life of the receiver. Table 7.3 lists the constraints, parameter ranges, as well as the heat transfer fluid (HTF) and different tube materials considered. For metallic tubes, the thickness is set to the minimum thickness specified in the ASME B36.10M pipe schedule. For ceramic tubes, the thickness is set to 3 mm, reflecting the minimum manufacturable thickness achievable with current ceramic technology, as advised by ceramic experts. The tube outer diameters, as listed in Table 7.3, are also from ASME metallic pipe manual B36.10M. While the diameter of ceramic tubes can be of any value, we opt to adhere to that for metallic tube to avoid large design space. Considering the heat flux map being symmetric about the north-south axis at noon, we set the total flow paths to two and therefore the total number of panels is varied in the design optimization along with the tube diameter. We simulate the thermal and structural performance of the tubes under the heat flux on the day of summer solstice as it is found to

be the most critical design point from a structural integrity perspective.

Parameters	Values
Climate	USA, CA, Dagget (TMY3)
Max/min heliostat field capacity	2000 m / 50 m
Tower optical height	100 m
Annual simulation	9 representative days with 1 hr frequency
Solar field design power	180 MW_t
Design point DNI	950 W/m^2
Sun location at design point	Summer solstice
Heliostat size; reflectance; slope error	7.07 m x 7.07 m; 90%; $1.5e^{-3}$ rad
Receiver thermal absorptance	98%

Table 7.1: SolarPILOT simulation parameters.

Receiver #	Allowable flux	Receiver height	Receiver diameter	Aspect ratio
1	1000 kW/m^2	12 m	10 m	1.2
2	700 kW/m^2	12 m	16 m	0.75
3	450 kW/m^2	12 m	24 m	0.5

Table 7.2: Receiver optimal dimensions vs allowable heat flux.

Parameters	Values
Allowable heat flux	1000 kW/m^2, 700 kW/m^2, 450 kW/m^2
Tube outer diameter	42.2 mm, 33.4 mm, 21.2 mm
Tube thickness	1.24 mm (metal), 3 mm (ceramic)
Tube spacing	1 mm
Total flowpaths	2
Total panels	12, 18, 24
Number of bends per panels	4
Tube material	Metal: A740H, A282; Ceramic: SiC
HTF	$NaCl - KCl - MgCl_2$ eutectic molten salt [66]
HTF inlet temperature	500°C
HTF outlet temperature	720°C
HTF outlet pressure	0.5 MPa
HTF pressure drop	less than 3 MPa
Additional criteria for metallic tubes	Must pass the primary design check

Table 7.3: Parameter constraint and ranges for system optimization.

7.2 Metallic Receivers

For metallic receivers, we consider two high temperature nickel based superalloys, A740H and A282. The properties of these two materials can be found in [11] and also available in

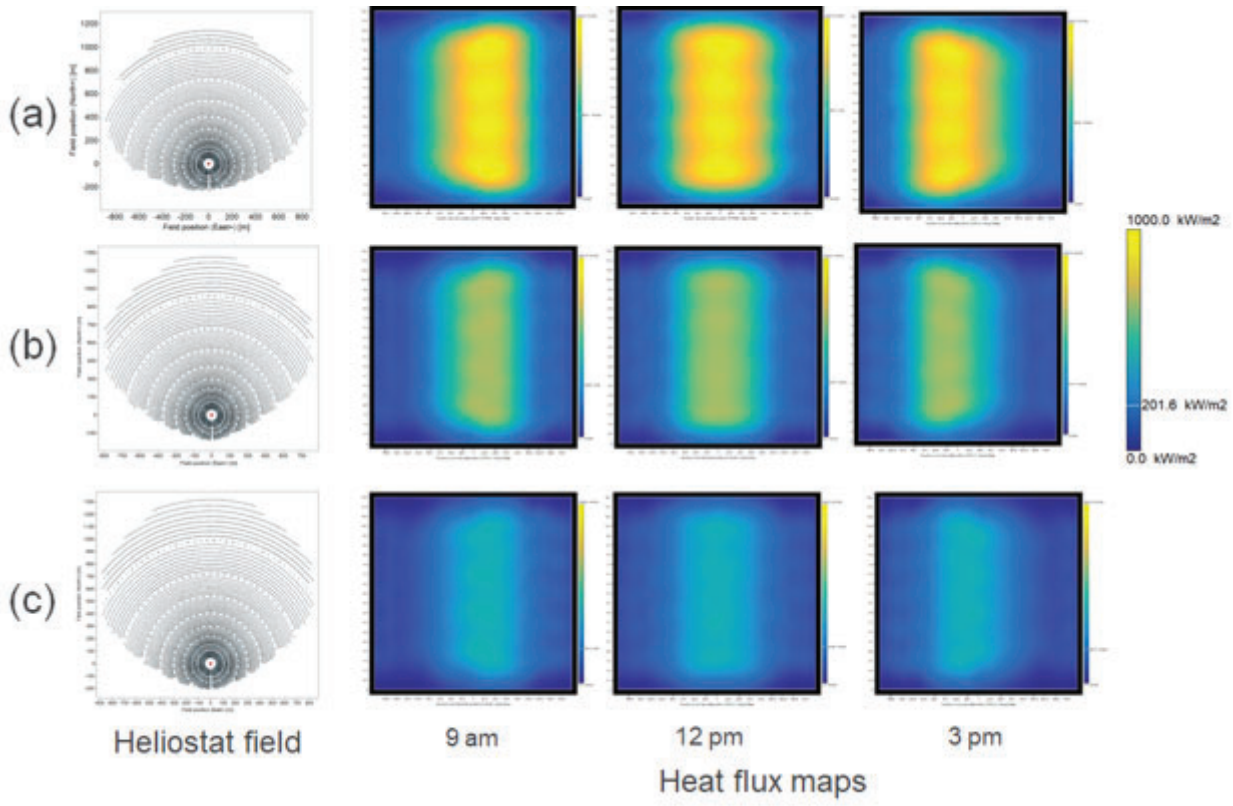

Figure 7.1: Heliostat field and heat flux maps at different times of the day of summer solstice for different allowable heat fluxes. (a) 1000 kW/m^2 (b) 700 kW/m^2 (c) 450 kW/m^2.

the material database of *srlife*.

We utilized *srlife* to estimate the life of receiver. First, the thermohydraulic module of *srlife* is used to determine the temperature history in the tube. This analysis is set to run iteratively to determine the optimal flow rate for the HTF for a target outlet temperature of 720°C. Fig. 7.2 shows some example results from thermohydraulic analysis. The results from the thermohydraulic analysis are then utilized to determine the pressure loss between the inlet and outlet, and this information is used to impose the pressure load in the structural analysis. For both the structural and thermohydraulic analyses, only two tubes are considered in the simulation to reduce computational time. During the structural analysis *srlife* also simultaneously performs a system analysis, considering the user-specified rigidity of the connections between the tubes and the tube manifold in a panel as well as the connections between different panels. For the system analysis, we assumed that the panels are disconnected from each other, but the tubes are rigidly connected to the tube manifold within each panel.

Using the stress and strain history from structural analysis, *srlife* performs the creep-fatigue damage analysis to estimate the life of the metallic receiver. Table 7.4 summarizes the results from design optimization of receiver#3 (see Table 7.2), considering A740H as the tube material. As the table indicates, the tube thickness was kept constant at 1.24 mm while tube diameter and the total number of panels in the receiver were varied. For larger

diameter tubes the maximum tube temperature is found to be higher compared to smaller diameter tubes. This can be explained considering the flow velocity of the HTF. For the same power, the HTF needs to flow at a higher velocity through smaller diameter tubes and thus higher Reynolds number which results in higher heat transfer coefficient and lower tube temperature. The higher flow velocity also explains the higher pressure drop between receiver inlet and outlet for the smaller diameter tubes.

Table 7.4 also indicates decreasing maximum tube temperature and increasing pressure drop for increasing number of panels when the tube size is the same. Since the total number of tubes in a receiver is about the same for the same tube size, more panels in a flowpath means the same amount of HTF is passed through less number of tubes. This increases the flow velocity and thus reduced tube temperature and higher pressure loss.

Taking into account the constraints specified in Table 7.3, configuration#7 in Table 7.4 is found to be the optimal configuration with a receiver life of 11482 days (30 years).

We performed similar analysis for other receiver dimensions (receiver# 2 and 3 in Table 7.2) as well as for A282. The optimum design configurations for all three allowable heat fluxes are listed in Table 7.5 for A740H and A282. For both materials, a receiver life of over 30 years can be achieved when the heat flux is limited to 450 kW/m^2. However, at higher allowable heat flux levels of 700 kW/m^2 and 1000 kW/m^2, the receiver life is drastically reduced to around 2 years for A740H and 3 to 4 years for A282. This sharp reduction in life is primarily due to the increased tube temperatures at higher heat fluxes, leading to faster creep damage accumulation.

Config.	Tube t (mm)	Tube OD (mm)	Total panels	Total tubes	Max. tube T ($°C$)	P loss (MPa)	Avg. cf life (days)
1	1.24	42.2	12	1740	883	0.12	0
2	1.24	42.2	24	1728	759	0.65	774
3	1.24	42.2	30	1740	749	1.17	2159
4	1.24	33.4	12	2184	821	0.21	503
5	1.24	33.4	18	2178	764	0.60	699
6	1.24	33.4	24	2184	750	1.34	2570
7[@]	1.24	33.4	30	2190	744	2.48	11482
8	1.24	21.3	12	3366	762	0.92	789
9	1.24	21.3	18	3366	744	2.96	8807
10	1.24	21.3	24	3366	741	6.66	37524

Table 7.4: Summary of thermal, structural, and damage analysis of receiver#3 (H: 12 m, D: 24 m, allowable flux: 450 kW/m2) for different tube outer diameter and total number of panels. Tube material is A740H. Creep-fatigue life calculated based on elastic-creep analysis of 30 simulated cycles. '@' indicates the optimum design configuration.

Material	Allowable flux (kW/m2)	Receiver dia. (m)	Tube t (mm)	Tube OD (mm)	Total panels	Total tubes	Max. tube T ($°C$)	P loss (MPa)	Avg. cf life (days)
A740H	450	24	1.24	33.4	30	2190	744	2.49	11482
	700	16	1.24	33.4	24	1440	764	2.62	732
	1000	10	1.24	33.4	18	900	807	2.60	634
A282	450	24	1.24	33.4	30	2190	744	2.49	15445
	700	16	1.24	33.4	24	1440	764	2.62	1544
	1000	10	1.24	33.4	18	900	809	2.60	1106

Table 7.5: Optimum metallic receiver designs.

7.3 Ceramic Receivers

For ceramic receiver, we consider a monolithic ceramic material, commercial SiC. The parameters required for reliability estimation, based on stress and temperature, include the Weibull modulus, scale parameter, threshold stress, and the SCG parameters B and N. These parameters for SiC were determined from fast fracture and constant stress rate tests conducted at ANL. Details of these experiments, along with the parameter estimation process, are discussed in Chapter 5. The estimated parameters are listed in Tables 5.7 and 5.10, and are also available in the material database of *srlife*.

For structural and thermal analysis, other required properties of SiC, such as thermal conductivity, thermal diffusivity, elastic modulus, and Poisson's ratio, were sourced from literature, with the exception of the coefficient of thermal expansion, which was measured at ANL. These parameters are also available in the *srlife* material database.

The analysis of SiC receivers was conducted in two steps. First, a design optimization was carried out based on the results from time-independent reliability analysis. Once the optimal design was identified, a time-dependent reliability analysis was performed to evaluate how the receiver's reliability changes over its service life. As discussed in Chapter 6, srlife offers various options for reliability analysis, including different failure models, crack shapes, and fracture criteria. In this study, all SiC receivers were analyzed using the PIA model. A comprehensive analysis of a receiver using multiple failure models and fracture criteria, along with a discussion on the conservatism and applicability of these models for ceramic receiver evaluation, can be found in [63].

Table 7.6 presents the results of the optimization process for the SiC receiver under an allowable flux of 450 kW/m^2. Configuration-1 in the table corresponds to the optimal design for the metallic material A740H, included here to highlight how SiC tubes would perform if a tube thickness of 1.24 mm could be achieved. However, in this study, the minimum tube thickness for SiC was set at 3 mm, as shown in Table 7.3. Increasing the tube thickness from 1.24 mm to 3 mm, while keeping the inner diameter constant, leads to an increase in maximum equivalent stress, which in turn reduces the predicted reliability, as determined by the Weibull 2-parameter model (see configuration-2 versus configuration-1 in Table 7.6). Additionally, the pressure drop for configuration-2 reaches 3.09 MPa, which exceeds the design constraint of 3 MPa. To reduce the pressure drop, the outer tube diameter was increased from 36.92 mm in configuration-2 to 38 mm in configuration-3. Although this adjustment reduced the pressure drop to 2.76 MPa—within the design constraints—it also resulted in a further increase in maximum equivalent stress, again reducing reliability

according to the Weibull 2-parameter model. Despite this increase in stress, configuration-3 was identified as the optimal design due to its acceptable pressure drop. Further increasing the outer diameter beyond 38 mm reduces the pressure drop even more, but it does not enhance the structural performance.

It can be seen from Table 7.6 that for all configurations the reliability is predicted to be 100% when using the Weibull 3-parameter model. This is because the stresses in all receiver tubes remain below the threshold stress of the Weibull 3-parameter model. The probability of failure equations for both the Weibull 2-parameter and Weibull 3-parameter models are provided in 5.11 and 5.12, respectively. Fig. 7.3 compares the fit of the Weibull 2-parameter and Weibull 3-parameter models to experimental data, along with the range of maximum equivalent stress values from Table 7.6 and the threshold stress of the Weibull 3-parameter model. As shown in the figure, the maximum equivalent stress in all configurations is below the threshold stress, whether for volume or surface flaws. As a result, the Weibull 3-parameter model consistently predicts 100% reliability. In contrast, the Weibull 2-parameter model predicts a non-zero probability of failure even when the equivalent stress is close to zero. The difference in reliability estimation between Weibull 2-parameter and Weibull 3-parameter model becomes significant for large components like the 12-meter-long receiver tubes analyzed in this study. When considering each element in the finite element model of the tube, the cumulative probability of failure can quickly add up, leading to a considerably lower reliability estimation when using the Weibull 2-parameter model.

As Fig. 7.3 illustrates, the maximum equivalent stress remains well below the minimum experimental strength of the SiC material, indicating that the tubes are not expected to fail under these stress levels. However, the Weibull 2-parameter model still predicts lower reliability. This comparison between the Weibull 2-parameter and Weibull 3-parameter models underscores two important considerations for designing ceramic receiver tubes - (1) ceramic materials should not be rejected solely based on Weibull 2-parameter model results, and (2) larger specimens and full-scale tubes should be tested to improve confidence in the estimation of threshold stress. The latter is critical because, for large components like receiver tubes, the reliability prediction in the Weibull 3-parameter model is predominantly influenced by the threshold stress parameter.

Table 7.7 presents the time-dependent reliability of the optimal SiC receiver design (configuration-3 from Table 7.6) as a function of service life, under an allowable flux of 450 kW/m^2. This time-dependent reliability analysis takes into account the SCG, which occurs due to the high operating temperatures and the diurnal cyclic loads experienced by the receiver. As indicated in Table 7.7, the transformed equivalent stress—a modification of the equivalent stress that includes the effects of SCG—rises with increasing service life. Consequently, reliability predictions based on the Weibull 2-parameter model decrease over time as service life increases. However, the Weibull 3-parameter model consistently predicts 100% reliability, even for a service life of up to 30 years, since the maximum transformed effective stress remains below the threshold stress throughout the receiver's lifetime.

We performed similar design optimization analyses for other receiver dimensions (receiver# 2 and 3 in Table 7.2). Table 7.8 lists the optimum receiver configurations for different allowable heat fluxes, along with their time-independent reliability. As the table indicates, the reliability of the receiver, estimated using the Weibull 2-parameter model, decreases as the allowable heat flux increases. However, the Weibull 3-parameter model estimates 100%

reliability for all three flux limits. This is because the equivalent stresses in the receiver tubes are below the threshold stress.

Table 7.9 lists the service life of the three optimum SiC receiver designs based on different target minimum tube reliability. Since the time-dependent reliability analysis is a probabilistic method, it estimates the reliability of a component for a given service time, meaning the life of a ceramic receiver can only be estimated for a defined target reliability. For instance, a life of y at x% target reliability indicates that the minimum probability of survival for individual tubes in the receiver is x% over a service life of y. Table 7.9 lists the estimated life of the SiC receivers for three target reliabilities set at 50%, 90% and 99% for the tubes in the receiver. As the table indicates, the estimated life (using the Weibull 2-parameter model) decreases as the target reliability increases. For an allowable flux of 450 kW/m^2, the Weibull 2-parameter model estimates a minimum life of 100 days at 50% target reliability. However, when the target reliability is increased to 90%, the estimated life drops 0 days. For higher allowable fluxes, the estimated life is 0 days even at 50% target reliability.

On the other hand, the Weibull 3-parameter model estimates a service life exceeding 30 years for all three levels of allowable flux, even at a target reliability of 99%. Again, this is because the maximum transformed effective stress remains below the threshold stress.

Config.	Tube ID (mm)	Tube t t (mm)	Tube OD (mm)	Total panels	Total tubes	Max. tube T (°C)	P loss (MPa)	Max. eq. stress (MPa)	Min. tube reliability (time-independent)			
									Weibull 2P model			Weibull 3P model (combined)
									Vol. flaw	Surf. flaw	Combined	
1*	30.92	1.24	33.40	30	2190	740	2.47	72	98%	93%	91%	100%
2	30.92	3	36.92	30	1980	744	3.09	76	95%	92%	88%	100%
3@	32	3	38	30	1920	745	2.76	79	94%	89%	84%	100%
4	33	3	39	30	1860	745	2.49	81	92%	87%	80%	100%
5	34	3	40	30	1830	746	2.26	83	89%	84%	74%	100%

Table 7.6: Optimization of SiC receiver design for an allowable flux of 450 kW/m^2. '@' indicates the optimum design configuration. '*' indicates the configuration found for optimum design of A740H receiver.

Life time (days)	Max. transformed eq. stress (MPa)	Min. tube reliability (time-dependent)			
		Weibull 2P model			Weibull 3P model
		Vol. flaw	Surf. flaw	Combined	(combined)
0	79	94%	89%	84%	100%
1	89	84%	79%	67%	100%
10	92	79%	74%	58%	100%
100	96	73%	68%	49%	100%
1000	99	65%	60%	39%	100%
10000 (30 years)	103	56%	52%	29%	100%

Table 7.7: Time-dependent reliability of the optimum SiC receiver design for 450 kW/m^2 flux limit as a function of service life.

Allowable flux (kW/m^2)	Receiver diameter (m)	Tube t (mm)	Tube OD (mm)	Total panels	Total tubes	Max. tube T ($°C$)	P loss (MPa)	Minimum tube reliability (Time-independent)	
								Weibull-2P	Weibull-3P
450	24	3.00	38	30	1920	745	2.49	84%	100%
700	16	3.00	38	24	1272	768	2.62	25%	100%
1000	10	3.00	38	18	792	820	2.60	0%	100%

Table 7.8: Optimum ceramic (SiC) receiver designs.

Allowable flux (kW/m2)	Receiver diameter (m)	Tube t (mm)	Tube OD (mm)	Total tubes	Life (days) at x% target minimum tube reliability reliability					
					x=50%		x=90%		x=99%	
					Weibull 2P	Weibull 3P	Weibull 2P	Weibull 3P	Weibull 2P	Weibull 3P
450	24	3.00	38	1920	100	>10000	0	>10000	0	>10000
700	16	3.00	38	1272	0	>10000	0	>10000	0	>10000
1000	10	3.00	38	792	0	>10000	0	>10000	0	>10000

Table 7.9: Life of ceramic (SiC) receiver for different target reliabilities.

7.4 Receiver life comparison

Fig. 7.4 provides a detailed comparison of the estimated service lives of metallic receivers, constructed from A740H and A282, and ceramic receivers, made from SiC, as a function of varying allowable flux limits. The life estimations for SiC are based on both the Weibull 2-parameter and Weibull 3-parameter models. Since the life estimates of metallic receivers are based on the average material properties, a target reliability of 50% was used for the Weibull 2-parameter model in SiC analysis. However, this target reliability is not applied to the Weibull 3-parameter model, as it predicts a life of more than 30 years with 100% reliability for all three SiC receiver designs.

As illustrated in Fig. 7.4, the Weibull 2-parameter model predicts an almost negligible service life for SiC receivers across all flux levels. This occurs because the Weibull 2-parameter model tends to underestimate the reliability of large components, such as the 12-meter-long tubes in the receivers considered in this study. The high probability of failure in large volumes significantly reduces the life estimates in this model.

In contrast, the Weibull 3-parameter model predicts a service life of more than 30 years for SiC receivers at all flux levels with 100% reliability. This stark difference between the two models underscores the critical importance of accounting for a material's threshold stress, which is only considered in the Weibull 3-parameter model. The threshold stress effectively eliminates failure predictions for stress values below a certain limit, allowing for more realistic reliability estimates. However, due to the large size of the receiver tubes, the life estimation using the Weibull 3-parameter model largely depends on the accuracy of the threshold stress parameter. Therefore, precise experimental estimation of the threshold stress is crucial. Confidence in this estimation can be improved by testing more standard-size specimens, some large specimens, and a limited number of full-size tubes.

Both A740H and A282 receivers show a different trend. At higher allowable flux levels, the estimated service life of these metallic receivers is significantly reduced, with a projected

life of only a few years. This reduction is due to the materials' susceptibility to creep at elevated temperatures, which is exacerbated by high incident heat flux, accelerating damage accumulation. However, when the allowable flux is reduced to 450 kW/m^2, the metallic receivers are estimated to last up to 30 years.

Although reducing the allowable flux extends the service life of the receiver, there is a trade-off: as the allowable flux decreases, the number of receiver tubes required increases to maintain the system's overall thermal power output. Fig. 7.4 also illustrates this trade-off, showing how reducing the flux necessitates a larger-diameter receiver with additional tubes, which can increase both material and construction costs.

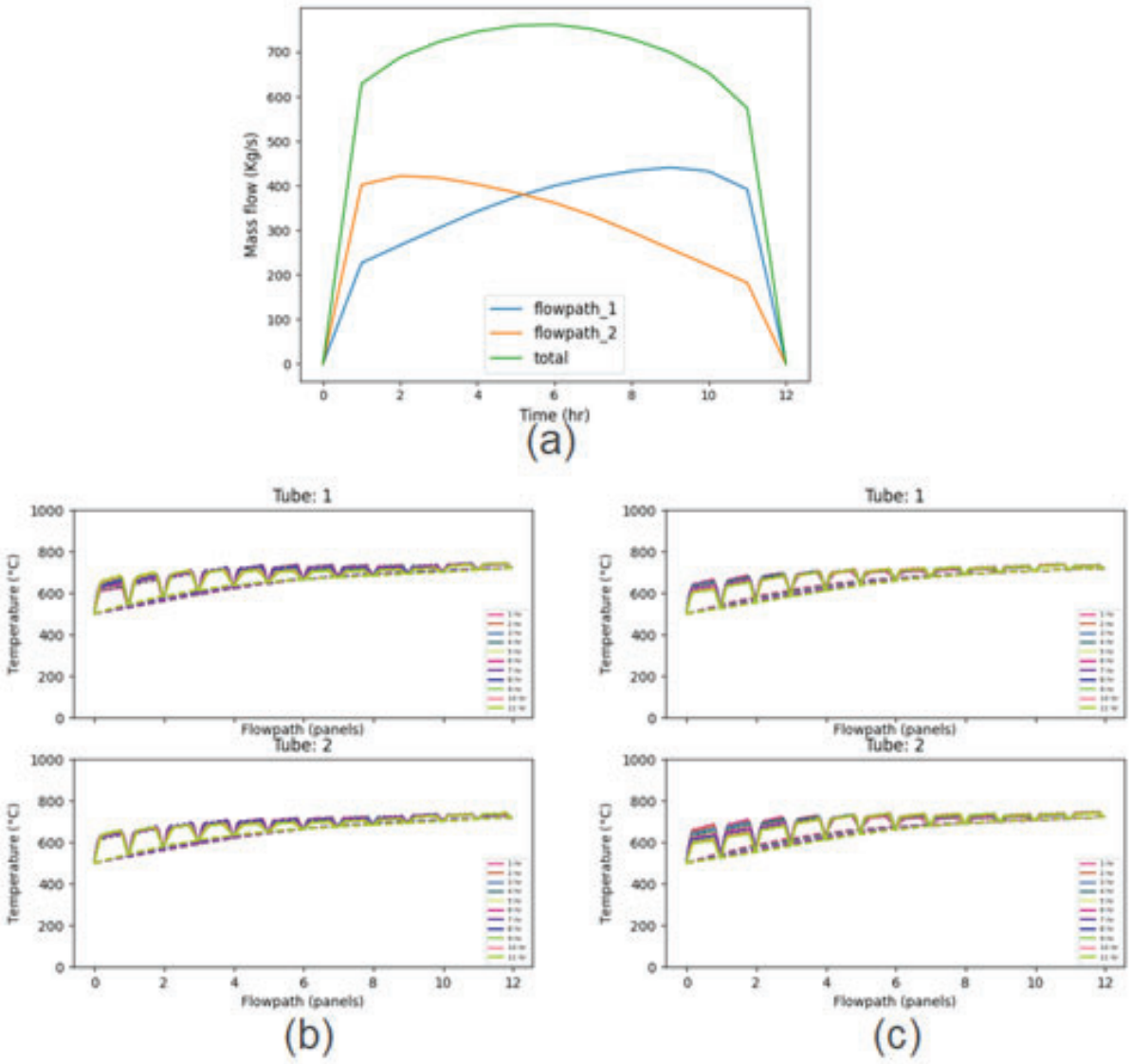

Figure 7.2: Example thermohydraulic results showing (a) variation in HTF mass flow rate during the day for a constant outlet temperature of 720°C; and (b, c) changes in HTF (dashed lines) and tube crown (solid lines) temperatures (shown for the coldest and hottest tubes in the panel) along two flowpaths at different times of the day.

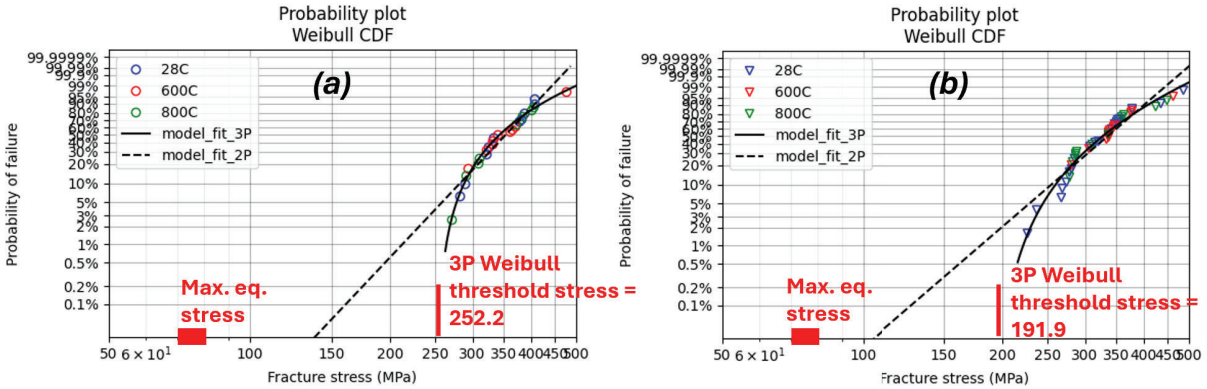

Figure 7.3: Maximum equivalent stress in the SiC receiver with optimum configuration for 450 kW/m^2 allowable flux is compared to the Weibull 2-parameter and Weibull 3-parameter model fit to experimental strength data of SiC for failure due to (a) volume flaws and (b) surface flaws.

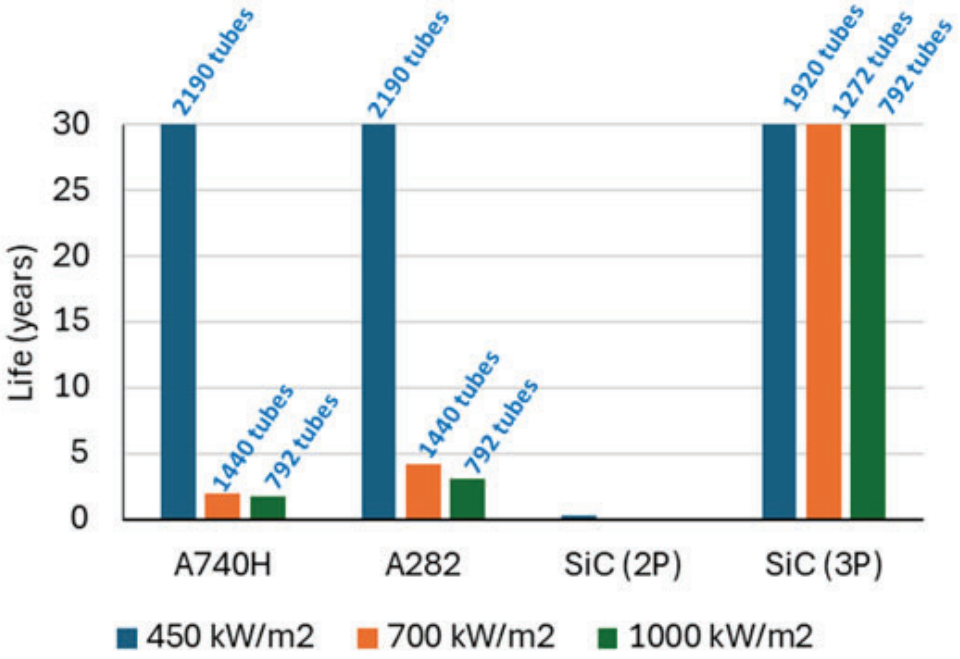

Figure 7.4: Receiver life comparison between metals (A740H and A282) and ceramic (SiC) and the number of required tubes for each optimal design as a function of allowable flux limit.

8 Conclusions

This report documents the development of a comprehensive framework for evaluating the long-term reliability of ceramic receivers in high temperature CSP systems. The *srlife* tool, originally developed for evaluating high temperature metallic receivers, was extended to include both time-independent and time-dependent reliability analyses for ceramic receivers. While *srlife* is a complete analysis module for tubular receiver analysis, its reliability module can also be applied to other ceramic components using stress and temperature results from any finite element analysis software.

The ceramic failure models implemented in *srlife* are based on various failure criteria, including (i) the PIA method, (ii) the WNSTA method, (iii) the MTS criterion, (iv) the total CSE release rate criterion, and (v) the SMM criterion. The PIA and WNSTA models are inherently crack shape-independent and shear-insensitive, while the other models are crack shape-dependent. *srlife* provides options for modeling two types of cracks —Griffith flaw and penny-shaped flaw — for volume flaw reliability analysis, and two types — Griffith notch and semi-circular crack — for surface flaw analysis. For the crack shape-dependent models, *srlife* offers two analysis options — one using shear-insensitive fracture criteria and one using shear-sensitive fracture criteria. These models, adopted from NASA's CARES program manuals [9][10], were validated through the simulation results provided in these references. They account for ceramic strength variations using Weibull model parameters estimated from fast fracture test data. The effect of long-term service loads on reliability is incorporated using SCG parameters which can be estimated from various time-dependent tests, such as constant stress rate tests, constant stress tests, and cyclic fatigue tests.

SiC, a commercially available advanced ceramic, was investigated as a potential replacement for high temperature metallic components due to its superior properties, such as high temperature strength and low thermal expansion. Fast fracture and constant stress rate tests of SiC were conducted at room temperature, $600°C$, and $800°C$to determine the necessary material parameters for the failure models, including Weibull parameters and SCG constants. Experimental results indicate that SiC retains excellent strength up to $800°C$and shows negligible SCG under typical CSP operating conditions.

A comparative design analysis between metallic receivers (A740H and A282) and SiC ceramic receivers revealed that while metallic receivers can perform adequately (30 years of service life) at lower flux levels (450 kW/m^2), their service life significantly diminishes (to a few years) under high heat flux (700 kW/m^2 and above) due to accelerated creep damage. In contrast, SiC ceramic receivers maintain structural integrity even at elevated flux levels (over 30 years of service life at 1000 kW/m^2), making them a more suitable option for future high-efficiency CSP systems.

Another critical aspect of this report is the comparison between the Weibull 2-parameter and 3-parameter models for predicting the reliability of ceramic receivers. The Weibull 2-parameter model, although widely used, was found to be overly conservative for large components, such as the 12-meter-long receiver tubes analyzed in this study. This model predicts a nonzero probability of failure at very low stress levels, potentially leading to an unrealistically short estimated service life for large components. In contrast, the Weibull 3-parameter model introduces a threshold stress below which the probability of failure is zero. This comparison highlights the importance of using the Weibull 3-parameter model for more realistic reliability assessments, especially for large ceramic components like CSP receiver

tubes. Accurate estimation of the threshold stress is crucial for the Weibull 3-parameter model to provide reliable predictions, and confidence in this estimation can be improved by testing a range of specimens, including standard-size, large, and a limited number of full-size tubes.

Overall, the extended *srlife* tool provides essential capabilities for CSP developers to assess the feasibility of ceramic receivers and other components, offering detailed comparisons with traditional metallic designs. This work advances design methodologies for CSP components and provides a reliable path forward for integrating ceramics into next-generation solar energy systems.

Acknowledgements

This work was sponsored by the U.S. Department of Energy under Contract No. DE-AC02-06CH11357 with Argonne National Laboratory, managed and operated by UChicago Argonne LLC. The authors gratefully acknowledge support from the U.S. Department of Energy through the Office of Energy Efficiency and Renewable Energy, Solar Energy Technologies Office, CSP Program (project 38482). Special thanks are extended to Joseph Coventry of Australian National University for providing expertise in creating the reference receiver systems used for comparative design analysis between metallic and ceramic receivers. The authors also appreciate the valuable discussions with DOE project manager Kamala Raghavan.

Bibliography

[1] B. Barua and M. C. Messner, "Structural design challenges and implications for high temperature concentrating solar power receivers," Solar Energy, vol. 251, no. June 2022, pp. 119–133, 2023.

[2] B. Barua, M. McMurtrey, R. E. Rupp, and M. C. Messner, "Design guidance for high temperature concentrating solar power components," Tech. Rep. ANL-20/03, Argonne National Lab.(ANL), Argonne, IL (United States), 2020.

[3] J. Kim, B. K. Sovacool, M. Bazilian, S. Griffiths, J. Lee, M. Yang, and J. Lee, "Decarbonizing the iron and steel industry: A systematic review of sociotechnical systems, technological innovations, and policy options," Energy Research & Social Science, vol. 89, p. 102565, 2022.

[4] S. Ghavam, M. Vahdati, I. G. Wilson, and P. Styring, "Sustainable ammonia production processes," Frontiers in Energy Research, vol. 9, p. 580808, 2021.

[5] B. Barua, M. C. Messner, and D. Singh, "Assessment of Ti3SiC2MAX phase as a structural material for high temperature receivers," AIP Conference Proceedings, vol. 2445, no. May, 2022.

[6] M. C. Messner, B. Barua, and D. Singh, "Towards a Design Framework for Non-metallic Concentrating Solar Power Components,"

[7] C. Carter, "Ceramic materials: Science and engineering," 2007.

[8] T. Lube and R. G. Baierl, "Sub-critical crack growth in alumina–a comparison of different measurement and evaluation methods," BHM Berg-und Hüttenmännische Monatshefte, vol. 156, no. 11, pp. 450–456, 2011.

[9] N. N. Nemeth, J. M. Manderscheid, and J. P. Gyekenyesi, "Ceramics Analysis and Reliability Evaluation (CARES) Users and Programmers Manual," tech. rep., NASA, 1990.

[10] N. N. Nemeth, L. M. Powers, L. a. Janosik, and J. P. Gyekenyesi, "CARES/LIFE Ceramics Analysis and Reliability Evaluation of Structures Life Prediction Program," Tech. Rep. February, NASA, 2003.

[11] M. C. Messner, B. Barua, and M. McMurtrey, "srlife: A fast tool for high temperature receiver design and analysis," Tech. Rep. ANL-22/29, Argonne National Lab.(ANL), Argonne, IL (United States), 2022.

[12] R. L. Barnett, P. C. Hermann, J. R. Wingfield, and C. L. Connors, "Fracture of Brittle Materials Under Transient Mechanical and Thermal Loading," 1967.

[13] FREUDENTHAL and A. M., "Statistical approach to brittle fracture," Fracture, An Advanced Treatise, II, pp. 591–619, 1968.

[14] WEIBULL and W., "A statistical theory of strength of materials," IVB-Handl., 1939.

[15] B. Gross and J. P. Gyekenyesi, "Weibull Crack Density Coefficient for Polydimensional Stress States," Journal of the American Ceramic Society, vol. 72, no. 3, pp. 506–507, 1989.

[16] D. K. Shetty, "Mixed-Mode Fracture Criteria for Reliability Analysis and Design With Structural Ceramics," ASME International Mechanical Engineering Congress and Exposition, Proceedings, vol. 109, no. July, 1987.

[17] K. Palaniswamy and W. G. Knauss, "on the Problem of Crack Extension in Brittle Solids Under General Loading.," Mech Today, vol. 4, pp. 87–148, 1978.

[18] S. B. BATDORF and H. L. HEINISCH, "Weakest Link Theory Reformulated for Arbitrary Fracture Criterion," Journal of the American Ceramic Society, vol. 61, no. 7-8, pp. 355–358, 1978.

[19] S. B. Batdorf and J. G. Crose, "Statistical Theory for the Fracture of Brittle Structures Subjected To Nonuniform Polyaxial Stresses.," American Society of Mechanical Engineers (Paper), no. 74 -APM-D, 1974.

[20] S. B. Batdorf, "Some approximate treatments of fracture statistics for polyaxial tension," International Journal of Fracture, vol. 26, no. 4, pp. 394–400, 1984.

[21] J. P. Gyekenyesi and N. N. Nemeth, "Surface flaw reliability analysis of ceramic components with the SCARE finite element postprocessor program," Journal of Engineering for Gas Turbines and Power, vol. 109, no. 3, pp. 274–281, 1987.

[22] I. Hotz, L. Feng, B. Hamann, and K. Joy, "Tensor-fields visualization using a fabric-like texture applied to arbitrary two-dimensional surfaces," Mathematics and Visualization, vol. 0, no. December, pp. 139–155, 2009.

[23] G. C. Sih, L. U. I. of Fracture, and S. Mechanics, Handbook of Stress-intensity Factors: Stress-intensity Factor Solutions and Formulas for Reference. No. v. 2 in Handbook of Stress-intensity Factors, Lehigh University, Institute of Fracture and Solid Mechanics, 1973.

[24] K. Palaniswamy and W. G. Knauss, "On the problem of crack extension in brittle solids under general loading," tech. rep., 1978.

[25] F. W. Smith, A. F. Emery, and A. S. Kobayashi, "Stress intensity factors for semicircular cracks: Part 2-semi-infinite solid," Journal of Applied Mechanics, Transactions ASME, vol. 34, no. 4, pp. 953–959, 1964.

[26] F. W. S. Sorensen and D. R., "Mixed mode stress intensity factors for semi elliptical surface cracks," tech. rep., Colorado State University, 1974.

[27] S. M. Wiederhorn, Subcritical Crack Growth in Ceramics. Springer, 1974.

[28] G. D. Quinn and J. B. Quinn, "Slow Crack Growth in Hot-Pressed Silicon Nitride," Fracture Mechanics of Ceramics, vol. 6, pp. 603–686, 1983.

[29] S. R. Choi and J. P. Gyekenyesi, "Slow crack growth analysis of advanced structural ceramics under combined loading conditions: Damage assessment in life prediction testing," Journal of Engineering for Gas Turbines and Power, vol. 123, no. 2, pp. 277–287, 2001.

[30] G. D. Quinn and R. N. Katz, "Time Dependence of the High Temperature Strength of Sintered Alpha Silicon TIME DEPENDENCE OF THE HIGH TEMPERATURE \ STRENGTH OF SINTEREO ALPHA SILICON CARBIDE," Tech. Rep. February 2018, Army Materials and Mechanics Research Center, 1979.

[31] S. R. Choi, J. A. Salem, and N. N. Nemeth, "High-temperature slow crack growth of silicon carbide determined by constant-stress-rate and constant-stress testing," Journal of Materials Science, vol. 33, no. 5, pp. 1325–1332, 1998.

[32] S. R. Choi, N. N. Nemeth, and J. P. Gyekenyesi, "Slow crack growth of brittle materials with exponential crack velocity under cyclic fatigue loading," International Journal of Fatigue, vol. 28, no. 2, pp. 164–172, 2006.

[33] T. Lube and R. G. A. Baierl, "Sub-Critical Crack Growth in Alumina – a Comparison of Different Measurement and Evaluation Methods," BHM Berg- und Hüttenmännische Monatshefte, vol. 156, no. 11, pp. 450–456, 2011.

[34] C. J. Gilbert, D. R. Bloyer, M. W. Barsoum, T. El-Raghy, A. P. Tomsia, and R. O. Ritchie, "Fatigue-crack growth and fracture properties of coarse and fine-grained Ti3SiC2," Scripta Materialia, vol. 42, no. 8, pp. 761–767, 2000.

[35] G. Sturmer, A. Schulz, and S. Wittig, "Life time prediction for ceramic gas turbine components," American Society of Mechanical Engineers (Paper), pp. 1–2, 1991.

[36] F. Test, "ASTM C1368 Standard Test Method for Determination of Slow Crack Growth Parameters of Advanced Ceramics by Constant Stress Rate Strength Testing at Ambient Temperature," Tech. Rep. Reapproved, ASTM, 2010.

[37] R. H. Dauskardt, M. James, J. Porter, and R. Ritchie, "Cyclic fatigue-crack growth in a SiC-whisker-reinforced alumina ceramic composite: long-and small-crack behavior," Journal of the American Ceramic Society, vol. 75, no. 4, pp. 759–771, 1992.

[38] W. K., "Effects of Environment and Complex Load History on Fatigue Life," p. 1, ASTM International, 1970.

[39] L. R. Swank and R. M. Williams, "Correlation of Static Strengths and Speeds of Rotational Failure of Structural Ceramics.," American Ceramic Society Bulletin, vol. 60, no. 8, pp. 830–834, 1981.

[40] ASTM International, "ASTM Standard Test Method for Flexural Strength of Advanced Ceramics at Ambient Temperautre C1161 - 18," tech. rep., ASTM, 2003.

[41] ASTM International, "ASTM Standard Test Method for Flexural Strength of Advanced Ceramics at Elevated Tempeartures C1211 - 18," tech. rep., ASTM, 2003.

[42] F. Test, "ASTM C1456 Standard Test Method for Determination of Slow Crack Growth Parameters of Advanced Ceramics by Constant Stress-Rate Flexural Testing at Elevated Temperatures," Tech. Rep. Reapproved, 2010.

[43] F. Test, "ASTM C1834 Standard Test Method for Determination of Slow Crack Growth Parameters of Advanced Ceramics by Constant Stress Flexural Testing (Stress Rupture) at Elevated Temperatures," Tech. Rep. Reapproved, ASTM, 2010.

[44] "Stanford Advanced Materials."

[45] "Test Resources."

[46] "Applied Test Systems."

[47] "Bomas."

[48] ASTM International, "ASTM C1421 Standard Test Methods for Determination of Fracture Toughness of Advanced Ceramics at Ambient Temperature," Tech. Rep. Reapproved 2007, 2001.

[49] Astm C1239, "Standard Practice for Reporting Uniaxial Strength Data and Estimating Weibull Distribution Parameters for Advanced Ceramics," Astm, vol. i, no. January, pp. 1–17, 2000.

[50] ASTM C1322-15 (Reapproved 2019), "Standard Practice for Fractography and Characterization of Fracture Origins in Advanced Ceramics," Tech. Rep. Reapproved, 2019.

[51] G. D. Slavin, Michael J. Quinn, "Mechanical Property Evaluation at Elevated Temperatures of Sintered Beta Silicon Carbide.," tech. rep., ARMY LAB COMMAND WATERTOWN MA MATERIAL TECHNOLOGY LAB, 1986.

[52] L. Chao and D. K. Shetty, "Reliability analysis of structural ceramics subjected to biaxial flexure," Journal of the American Ceramic Society, vol. 74, no. 2, pp. 333–344, 1991.

[53] R. Danzer, "Some notes on the correlation between fracture and defect statistics: Are Weibull statistics valid for very small specimens?," Journal of the European Ceramic Society, vol. 26, no. 15, pp. 3043–3049, 2006.

[54] J. B. Quinn and G. D. Quinn, "A practical and systematic review of Weibull statistics for reporting strengths of dental materials," Dental Materials, vol. 26, no. 2, pp. 135–147, 2010.

[55] B. Gross, "Least Squares Best Fit Method for the Three Parameter Weibull Distribution: Analysis of Tensile and Bend Specimens with Volume or Surface Flaw Failure," NASA Technical Memorandum, vol. 4721, no. July 1996, pp. 1–26, 1996.

[56] J. J. Petrovic, "Weibull statistical fracture theory for the fracture of ceramics," Metallurgical Transactions A, vol. 18, no. 11, pp. 1829–1834, 1987.

[57] S. Nohut, "Three-parameter (3P) weibull distribution for characterization of strength of ceramics showing R-Curve behavior," Ceramics International, vol. 47, no. 2, pp. 2270–2279, 2021.

[58] H. Zhang, Z. Gao, C. Du, S. Bi, Y. Fang, F. Yun, S. Fang, Z. Yu, Y. Cui, and X. Shen, "Parameter estimation of three-parameter Weibull probability model based on outlier detection," RSC Advances, vol. 12, no. 53, pp. 34154–34164, 2022.

[59] B. Basu, D. Tiwari, D. Kundu, and R. Prasad, "Is Weibull distribution the most appropriate statistical strength distribution for brittle materials ?," vol. 35, pp. 237–246, 2009.

[60] R. Danzer, P. Supancic, J. Pascual, and T. Lube, "Fracture statistics of ceramics - Weibull statistics and deviations from Weibull statistics," Engineering Fracture Mechanics, vol. 74, no. 18, pp. 2919–2932, 2007.

[61] S. F. Duffy, L. M. Powers, and A. Starlinger, "Reliability analysis of structural ceramic components using a three-parameter weibull distribution," ASME 1992 International Gas Turbine and Aeroengine Congress and Exposition, GT 1992, vol. 2, 1992.

[62] K. Sarbjit, A. C. Raymond, and D. K. Shetty, "Short-Crack Fracture Toughness of Silicon Carbide," Journal of American Ceramic Society, pp. 179–185, 2009.

[63] P. S. Chaugule, D. Singh, B. Barua, and M. Messner, "Design Methods , Tools , and Data for Ceramic Solar Receivers Year 1 Continuation Report," Tech. Rep. ANL-22/48, Argonne National Laboratory, Lemont, 2022.

[64] C.-A. Asselineau, A. Fontalvo, S. Wang, F. Venn, J. Pye, and J. Coventry, "Techno-economic assessment of a numbering-up approach for a 100 mwe third generation sodium-salt csp system," Solar Energy, vol. 263, p. 111935, 2023.

[65] J. Martinek, S. Jape, and C. S. Turchi, "Evaluation of external tubular configurations for a high-temperature chloride molten salt solar receiver operating above 700° c," Solar Energy, vol. 222, pp. 115–128, 2021.

[66] X. Wang, J. D. Rincon, P. Li, Y. Zhao, and J. Vidal, "Thermophysical properties experimentally tested for nacl-kcl-mgcl2 eutectic molten salt as a next-generation high-temperature heat transfer fluids in concentrated solar power systems," Journal of Solar Energy Engineering, vol. 143, no. 4, p. 041005, 2021.

Applied Materials Division
Argonne National Laboratory
9700 South Cass Avenue, Bldg. 212
Argonne, IL 60439

www.anl.gov